Okinawa Institute of Science and Technology
Graduate University

Thesis submitted for the degree

Doctor of Philosophy

Wave Propagation and Light-Matter Interactions in Optical Nanofibers and Discrete Media

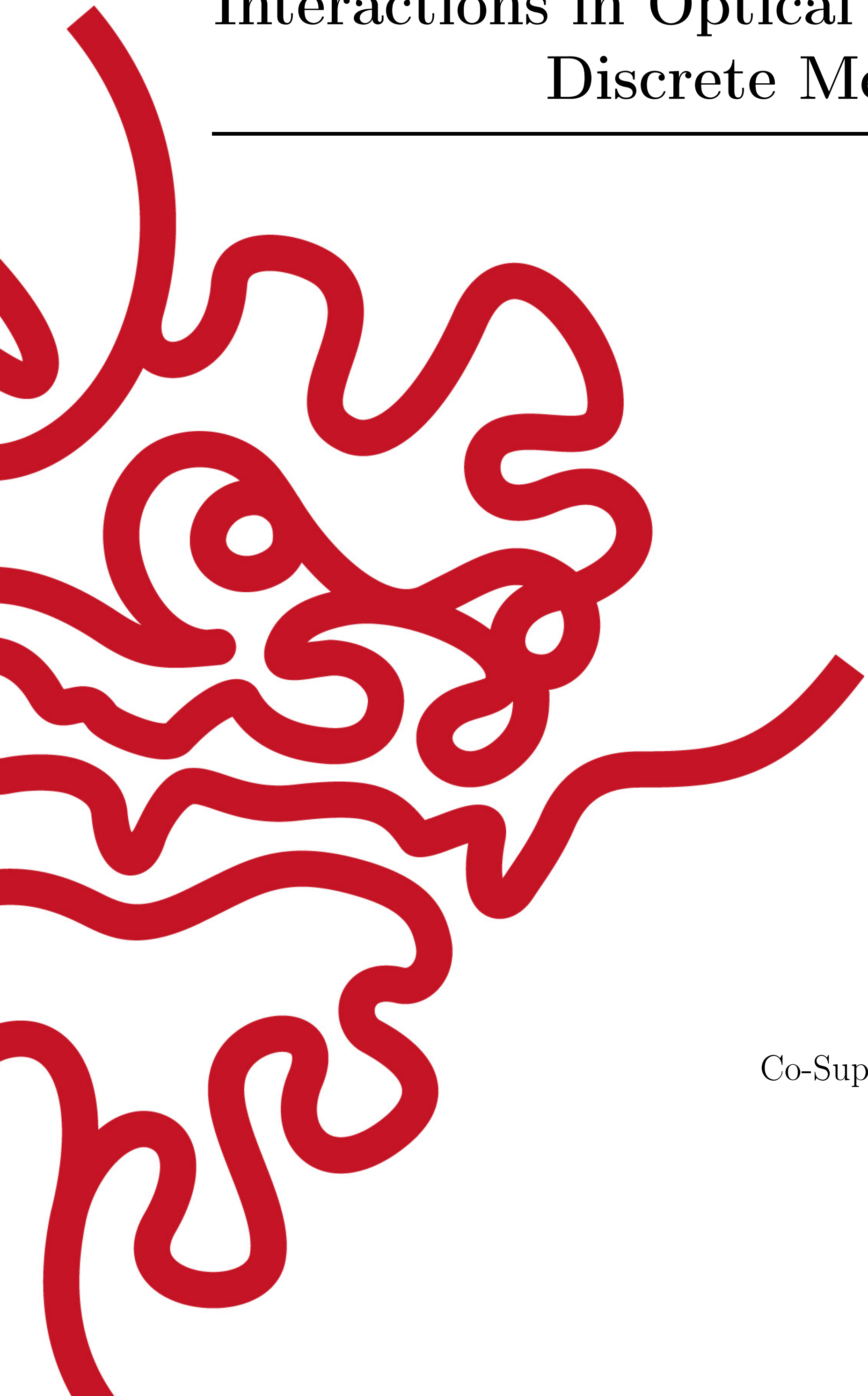

by

Lewis Ruks

Supervisor: **Thomas Busch**
Co-Supervisor: **Síle Nic Chormaic**

November 2022

Declaration of Original and Sole Authorship

I, Lewis Ruks, declare that this thesis entitled *Wave Propagation and Light-Matter Interactions in Optical Nanofibers and Discrete Media* and the data presented in it are original and my own work.

I confirm that:

- No part of this work has previously been submitted for a degree at this or any other university.
- References to the work of others have been clearly acknowledged. Quotations from the work of others have been clearly indicated, and attributed to them.
- In cases where others have contributed to part of this work, such contribution has been clearly acknowledged and distinguished from my own work.
- None of this work has been previously published elsewhere, with the exception of the following:
  The results of chapter 2 are published in
    - Le Kien, Fam, Lewis Ruks, Sile Nic Chormaic, and Thomas Busch. "Coupling between guided modes of two parallel nanofibers." New Journal of Physics **22**, no. 12 (2020): 123007.
      This project was conceived of by my collaborator, Dr Fam Le Kien. I did part of the analytical calculations and all of the numerical simulations. All authors contributed to the interpretation of results and to writing the later versions of the manuscript.
    - Le Kien, Fam, Lewis Ruks, Síle Nic Chormaic, and Thomas Busch. "Spatial distributions of the fields in guided normal modes of two coupled parallel optical nanofibers." New Journal of Physics **23**, no. 4 (2021): 043006.
      This project was conceived of by my collaborator, Dr Fam Le Kien. I did part of the analytical calculations and all of the numerical simulations. All authors contributed to the interpretation of results and to writing the later versions of the manuscript.
    - Kien, Fam Le, Lewis Ruks, and Thomas Busch. "Waveguide-induced dispersion interaction between two two-level atoms with orthogonal in-transverse-plane dipoles." Applied Physics B **125**, no. 11 (2019): 1-7.
      This project was conceived of by my collaborator, Dr Fam Le Kien. I did part

of the analytical calculations and all of the numerical simulations. All authors contributed to the interpretation of results and to writing the later versions of the manuscript.
The results of chapter 3 are published in

- Gietka, Karol, Lewis Ruks, and Thomas Busch. "Understanding and Improving Critical Metrology. Quenching Superradiant Light-Matter Systems Beyond the Critical Point." Quantum **6** (2022): 700.

The project was conceived of by my collaborator Dr Karol Gietka. I carried out analytical calculations concerning the dynamical evolution of the Dicke model, and the calculations concerning Fisher information obtained using the homodyne measurement. All authors contributed to the interpretation of results and the editing of the later versions of the manuscript.
The results of chapter 4 are published in

- Ruks, Lewis, and Thomas Busch. "Green's functions of and emission into discrete anisotropic and hyperbolic baths." Physical Review Research **4**, no. 2 (2022): 023044.

I conceived of and initiated the project, carried out all analytical calculations and numerical simulations, and wrote the manuscript. All authors contributed to the final interpretation of results and writing of the final version.

Date: 15 November 2022
Signature:

L Ruks

Abstract

Wave Propagation and Light-Matter Interactions in Optical Nanofibers and Discrete Media

Building on more than 50 years of sustained progress, artificial systems of atoms and photons are now routinely controllable down to the nanoscale, which paves the way for simulators and processors powered by the light-matter interaction. In particular the rapid experimental progress made in platforms of nanoscale photonics and neutral atoms demands fresh computational studies along with more powerful theoretical tools in order to simulate these increasingly complex (quantum) optical systems. In this thesis I contribute to (1) the understanding of current state-of-the-art in experimental optical nanofiber systems on one hand, and to (2) the general theory of emission into photonic lattices together with (3) quantum metrology in light-matter platforms. In the former I (1) systematically investigate light propagation in coupled optical nanofibers fibers and dispersion potential mediated through these nanofibers for experimentally relevant parameters, shedding light on effects that may be observed in near-future setups. In the latter I (2) study hyperbolic lattices exhibiting strongly anisotropic emission, with results that may have applications in transporting and storing photons in nanoscale platforms. Additionally, in a collaborative work (3) a proposal is made for a metrological protocol consisting of quenching through a quantum phase transition to obtain quantum-limited precision in system measurements.

Acknowledgment

I would first and foremost like to thank Thomas Busch for his generous and unwavering support over the past five years. His dedication to promoting long-term growth and independence in his students have undoubtedly made the doctoral pursuit all the more a rewarding experience. Thanks are further in order for my co-supervisors Síle Nic Chormaic and mentor Fam Le Kien. Síle has taught me valuable lessons about the practical side of research that have carried far into other aspects of life. On the other hand, I remain in awe at Fam's steadfast research ability, and his incredible breadth and depth of knowledge in my newfound field of quantum optics. Thanks/apologies are especially due for his patience in teaching me; I am grateful to have had the good fortune of working alongside Fam. I'd also like to thank our unit administrator Sawako Koki, who spared me from much of the administrative logistics of academia. In the lab, working with the easygoing and many members of the Busch Unit has been an enjoyable part of the experience – I very much appreciate the daily tea and/or sweets in the lunch rooms, which kept things lively even on the slower days. Away from OIST, I'd like to thank Dr Andreas Ruschhaupt, Dr Aidan Arnold, Prof. Helmut Ritsch, Prof. Janne Ruostekoski, and Dr. Bill Munro for the opportunity to present at their groups (in person or otherwise), and for their valuable insight during such short visits. I am especially indebted to Dr. Munro for additionally hosting me as an intern at NTT BRL. In two months I found my horizons greatly expanded, and I was particularly moved by the attention and assistance he offered to each individual in his group. Coming to a close, I'd like to thank my family and the friends made in the years before and during the Ph.D., particularly for their continuous support and the many life lessons shared that have undoubtedly brought me to where I am today.
Finally, an extra special thanks for the past five years, to Sachie.

Abbreviations

EM	electromagnetic
QED	quantum electrodynamics
BZ	Brillouin zone
TLS	two-level system
vdW	van der Waals
ONF	optical nanofiber
RDDI	resonant-dipole-dipole interaction
CMT	coupled mode theory
SQL	standard quantum limit
CR	Cramer-Rao
FI	Fisher information
QFI	quantum Fisher information
CFI	classical Fisher information

Nomenclature

c	Speed of light ($2.997\ 924\ 58 \times 10^{8}$ ms^{-1})
$\hbar$	Reduced Planck constant ($1.054\ 572\ 66 \times 10^{-34}$ Js)
μ_0	Permeability of free-space ($4\pi \times 10^{-7}$ Hm^{-1})
ϵ_0	Permittivity of free-space ($8.854\ 187\ 812\ 8 \times 10^{-12}$ Fm^{-1})

Contents

List of Figures

Introduction

In the past century hybrid systems of light and matter have seen an explosion in theoretical development and experimental realisations, bringing about technologies ubiquitous in everyday life, with the laser and LED as well-known examples. At the heart of such technologies is the basic light-matter interaction, which allows for the manipulation of both constituents and enables a wealth of applications realised in metrology [14, 15], manipulation of light [16, 17] and particles [18], and quantum simulation [19]. Whilst much of the theoretical groundwork for (quantum) optics was laid around half a century ago [20, 21], it remains a very much active topic of study to this day. In particular, advances on all fronts – experimental, analytical, and computational – have driven a push to the nanoscale in optical systems composed of macroscopic dielectric media, point-like emitters, and light [22, 23, 24]. In this setting, the effect of the sub-wavelength medium scales on light [22], of the energy dispersion [17, 25], and of the interplay of optics with quantum mechanics [26] are current key focal points in the theoretical community. Recent advances are abound, with quantum-limited atomic clocks [27] realised, simulators of quantum magnetism proposed [28], and optical metamaterials featuring single-photon nonlinearities fabricated [29]. As the accompanying experiments advance, models previously far from reality come within reach, demanding fresh theoretical studies with the potential to further expand our optical toolbox. In line with the following thesis summary, I will present investigations on the propagation of light and the interaction with emitters in nanoscale optical media representing current or near-future state-of-the-art.

0.1 Thesis summary

In this thesis, I investigate the propagation of light in continuum and discrete media, and supplement with studies investigating the consequences of light-matter interaction in such media. In the introduction I set the stage for the subsequent studies, exploring light propagation in macroscopic linear dielectric media together with the light-matter interaction between field and emitter, both in the classical and quantum formalisms. This discussion touches on existing results in the field.

In the second chapter I focus on setups based around the optical nanofiber, including a coupled two-fiber system and that of two atoms coupled through an optical nanofiber via the dispersion potential. Optical fibers are well established as the workhorse for transporting light over long distances with low loss and their derivative, the optical nanofiber, additionally offers a flexible platform for interfacing light and matter, offering powerful methods of manipulation and interfacing beyond free space. A particular system of two coupled fibers naturally allows for the creation of interferometers [30], sensors [31], and resonators [32], along with light-emitter platforms featuring enhanced coupling [33] and trapping [34]. While analogue two-waveguide-type structures on the nanoscale have been experimentally realised [35, 36, 37], a detailed theoretical analysis of the qualitative features of propagating light in coupled fibers with both radius and separation on the nanoscale is so far lacking. In the first half of the second chapter I systematically analyze the travelling modes of the two-fiber system using the approximate coupled-mode theory and using an exact eigenmode expansion for parameters of current experimental state-of-the-art. The results yield improved predictions on fiber-fiber mode coupling beyond existing and recent works [32] and shed light on the electric field profiles in the two-fiber system, which has since seen proposals in atom trapping [34] and interfacing [33].

In the second half of the second chapter I include a coupling to matter, investigating the dispersion potential between two ground-state atoms in the vicinity of nanoscale cylinders of differing material. Long-range dispersion forces at the micro- and nanoscale have an influence on the properties of matter on the macro-scale, and must also be taken into account in quantum optical experiments featuring similar length scales [38]. In the additional presence of optical media, anistropy in the resulting dispersion potential can be induced. This allows for tailoring of the potential [39, 40, 41], which in turn provides additional tools for investigating QED at a fundamental level. Despite this being the case, anisotropy in the dipole matrix elements of quantum emitters has not yet been taken into account yet, to my knowledge, except in the case of free space [42, 43, 44]. I thus investigate the dispersion potential between two atoms with distinct matrix elements when mediated through a cylinder of differing materials. I find that the cylinder-induced anisotropy of the field, together with anisotropic dipole elements, can result in a dispersion potential enhanced or diminished by orders of magnitude compared to free space. The findings both offer insight into dispersion forces in general strongly anisotropic environments and realistic predictions specifically in the case of existing optical nanofiber platforms.

In the third chapter I move from the open waveguide to the cavity, and investigate the quantum metrological applications of the collective light-matter coupling between atoms and a cavity – the archetypal Dicke model [45, 46]. One of the simplest quantum models – a collective spin coupled to a bosonic mode – the Dicke model features a quantum phase transition and symmetry breaking of the ground state. In the context of quantum metrology, a phase transition is beneficial due to system susceptibility diverging in the region, which is accompanied by a diverging sensitivity. Whilst this 'critical quantum metrology' [47, 48, 49] has been a recent subject of intense focus, a feature left unaddressed is that a quench through the critical point causes an instability of the vacuum state and results in a rapid generation of photons, that is, probes. I present my analytical calculations contributing to an investigation showing that this quench protocol offers an alternative route to increasing sensitivity in critical quantum systems. The results offer an alternative viewpoint on critical quantum metrology, and expand the toolbox of measurement techniques available to optical cavity-style setups.

In the fourth chapter, I consider linear wave propagation in a discrete but open lattice of bosonic modes via an investigation of the system Green's function, and study a range of effective emitter-emitter interactions that can be engineered through emission

into the structured bath. Extended and periodic optical media offer novel emitter-field and emitter-emitter interactions determined by the dispersion relation of the underlying bath [13, 28, 50, 51, 52, 53]. A particular class of bath is that with hyperbolic dispersion [9], featuring highly focused emission, sub-wavelength transport to the far field, and greatly enhanced spectral density of states, with applications in the tailoring of emission and emitter-emitter interactions [54, 55]. Despite their popularity in the quantum optics community, the discrete nature of realistic hyperbolic materials is rarely taken into account in theoretical investigations [11, 56], whilst despite the full power of artifical gauge fields available in photonic [57] and neutral atom [58] systems, they have yet to be exploited in conjunction with hyperbolic dispersion in quantum optics. In this work, I investigate the Green's function associated with a bosonic lattice featuring hyperbolic-like dispersion along with the induced emitter-emitter interactions in the Born-Markov approximation. I find unconventional exponentially decaying, yet disspative emitter-emitter interactions. Upon effecting an artifical gauge field on the lattice, I also find that quasi-one-dimensional transport of photons can be realised in higher dimensional baths. The latter finding allows one to construct effective cavities within structured baths with emitters as the effective mirrors [7, 59]. My work expands the toolbox of bath effected emitter-emitter interactions and paves the way for studies combining hyperbolic dispersion with other exotic features of structured baths.
In the fifth and final chapter I conclude the thesis with a summary and outlook. A summary of the chapters and the corresponding publications is given as follows:

- **Chapter 1: Background.** This chapter introduces the equations of motion for (quantum) light in macroscopic dielectric linear media, together with the equations describing the interacting of light and emitters. Notable consequences relevant to the thesis are discussed.

- **Chapter 2: Optical Nanofibers for Light-Matter Platforms.** As an analytically treatable geometry of an open optical waveguide, the optical nanofiber is given an extended discussion in the introduction of this chapter, which focuses theoretically on the guided modes and practically on optical nanofibers as a light-matter platform. In the first half of the chapter, the coupled mode theory and the exact eigenmode expansion of the two-fiber system is presented. The notable findings are presented from the publications [1] and [2] respectively:

  Coupling between guided modes of two parallel nanofibers
  F Le Kien, L Ruks, SN Chormaic, T Busch
  New Journal of Physics **22** (12), 123007 (2020)

  Spatial distributions of the fields in guided normal modes of two coupled parallel optical nanofibers
  F Le Kien, L Ruks, SN Chormaic, T Busch
  New Journal of Physics **23** (4), 043006 (2021)

  In the former the coupled mode theory is used to investigate the coupling between two optical nanofibers for experimentally realisable parameters and improve upon recent works [32]. In the latter the field profiles are comprehensively studied using the exact eigenmode expansion, and I observe that placing atoms at the center of the two fibers simultaneously allows for efficient interfacing and trapping. The field eigenvalues are also compared with the coupled mode theory, and I find that the discrepancy is large for close fibers and small fiber radii. The two projects were conceived of by my collaborator, Dr Fam Le Kien. I did part of the analytical calculations and all of the numerical simulations. All authors contributed to the interpretation of results and to writing the later versions of the manuscript. In the latter half of the chapter I explore the dispersion potential between two ground-state atoms with non-equal dipole transition matrix elements in the presence of a dielectric cylinder, contained in the work [3].

Waveguide-induced dispersion interaction between two two-level atoms with orthogonal in-transverse-plane dipoles
FL Kien, L Ruks, T Busch
Applied Physics B **125** (11), 1-7 (2019)

I find that the anisotropic and non-equal matrix elements in conjunction with different material responses allow for enhancement or diminishing of the dispersion potential with respect to free space. This project was conceived of by my collaborator, Dr Fam Le Kien. I did part of the analytical calculations and all of the numerical simulations. All authors contributed to the interpretation of results and to writing the later versions of the manuscript.

- **Chapter 3: Quenches Across The Superradiant Phase Transition For Quantum Metrology**

  I here introduce (critical) quantum metrology in the context of the Dicke model of cavity QED. I present my calculations describing the evolution of the field vacuum state in the superradiant phase along with the measurement statistics for a quadrature measurement. The calculations are given in the context of a proposed quantum metrological protocol given by a quench into the superradiant phase of the Dicke model and followed by a quadrature measurement, which is discussed in full in the publication [4]

Understanding and Improving Critical Metrology. Quenching Superradiant Light-Matter Systems Beyond the Critical Point
K Gietka, L Ruks, T Busch
Quantum **6**, 700 (2022)

The project was conceived of by my collaborator Dr Karol Gietka. I carried out analytical calculations concerning the dynamical evolution of the Dicke model, and the calculations concerning Fisher information obtained using the quadrature measurement. All authors contributed to the interpretation of results and the editing of the later versions of the manuscript.

- **Chapter 4: Wave Propagation And Emission In Discrete Baths Exhibiting Hyperbolic Dispersion** In this final chapter I consider wave propagation in and emission into baths described by a tight-binding lattice and exhibiting a dispersion analogous to that of hyperbolic media, as in the publication [5]

  Green's functions of and emission into discrete anisotropic and hyperbolic baths
  L Ruks, T Busch
  Physical Review Research **4** (2), 023044 (2022)

  In particular, I find that these discrete bosonic baths can mediate tunable dissipative and exponentially decaying interactions between emitters, whilst inclusion of an artificial magnetic field acting on the baths bosons results in robust quasi-one-dimensional emission into the 2D bath, that allows two emitters to act as near-perfect mirrors and form approximate cavity modes. Possibilities for experimental realisation are also discussed. I conceived of and initiated the project, carried out all analytical calculations and numerical simulations, and wrote the manuscript. All authors contributed to the final interpretation of results and writing of the final version.

- **Chapter 5: Conclusions.** I here provide a summary, in hindsight, of the individual chapters and of the thesis as a whole.

Chapter 1

Background: Electromagnetism and the light-matter interaction

1.1 Maxwell's Equations: Shaping the Electromagnetic Field

Light is a fundamental part of both our everyday lives and experiments at the cutting-edge of science. The ability to shape and guide light is intertwined with the advancement of technologies on many fronts, and a common way to control light is by using linear electric materials. To investigate electromagnetic (EM) waves and light-matter interactions in an electric linear medium, I start from the macroscopic and classical formulation of the source-free Maxwell's equations, described in the frequency domain for electric field $\mathbf{E}(\mathbf{r}, \omega)$ and magnetic field $\mathbf{H}(\mathbf{r}, \omega)$

$$\nabla \cdot \mathbf{H}(\mathbf{r}, \omega) = 0, \tag{1.1}$$

$$\nabla \cdot (\epsilon(\mathbf{r}, \omega)\mathbf{E}(\mathbf{r}, \omega)) = 0, \tag{1.2}$$

$$\nabla \times \mathbf{E}(\mathbf{r}, \omega) = i\omega\mu_0\mathbf{H}(\mathbf{r}, \omega), \tag{1.3}$$

$$\nabla \times \mathbf{H}(\mathbf{r}, \omega) = -i\omega\epsilon_0\epsilon(\mathbf{r}, \omega)\mathbf{E}(\mathbf{r}, \omega), \tag{1.4}$$

The linear electric response of the material, characterised through $\epsilon(\mathbf{r}, \omega)$, creates a 'potential' for light, allowing us to shape light beyond the transverse plane waves of free space. A central goal in (quantum) optics is to reduce the effective mode 'area', either to isolate the light or focus it (upon matter) in a region of interest. Two candidates for mode area given in [8] and [60, 61], for example, are

$$A^{(0)}_{\text{eff}} = \frac{\left(\int d\mathbf{r}\epsilon(\mathbf{r},\omega)|\mathbf{E}(\mathbf{r},\omega)|^2\right)}{\text{Max}_{\mathbf{r}}[\epsilon(\mathbf{r},\omega)|\mathbf{E}(\mathbf{r},\omega)|^2]}, \tag{1.5}$$

$$A^{(2)}_{\text{eff}} = \frac{\left(\int d\mathbf{r}|\mathbf{E}|^2\right)^2}{\int d\mathbf{r}|\mathbf{E}|^4}. \tag{1.6}$$

Note in the above dimension is left ambiguous, as one may try to minimize the full 3D mode volume or a transverse area. In free space, the diffraction limit $A_{\text{eff}} \gtrsim \lambda^2$ sets a lower limit on the field confinement in the transverse plane, and one then resorts to

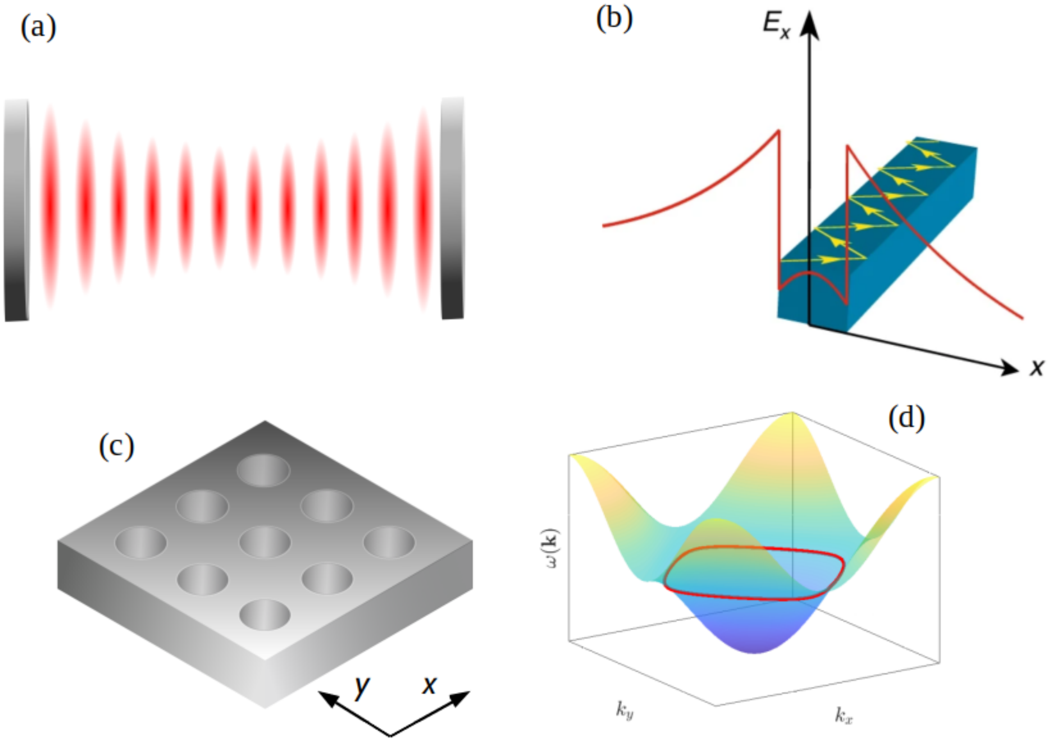

Figure 1.1: (a) Schematic of the optical cavity, with a standing wave confined between two highly reflective mirrors (b) Total internal reflection (yellow arrows) due to an increased dielectric refractive index (blue region) results in an evanescent field profile (red line) for, say, the x-polarization of an electric field guided by the structure. Taken from [6] (c) Periodic milling of holes in a dielectric, whose (periodic) refractive index modulation results in a (d) non-linear dispersion relation (with $\omega(\mathbf{k}) = \omega(k_x, k_y)$) for travelling waves of a given band in the transverse x-y plane.

imposing boundary conditions on the system in order to shape the field. To this end, one goal is to employ high-reflectivity conducting mirrors, effecting $\mathbf{E} \approx 0$ outside of a localized region featuring standing waves – the cavity (see Fig. 1.1(a)).

A complementary paradigm for exploring wave propagation, and the focus of the majority of this thesis, are extended optical environments. In particular, the conventional waveguide employed guides fields through regions of larger ϵ via the principal of total internal reflection. Assuming negligible loss and combining equations (1.3) and (1.4) to yield the Hermitian eigenvalue problem for $\mathbf{H}$ [17],

$$\hat{\Theta}\mathbf{H}(\mathbf{r},\omega) := \nabla \times \frac{1}{\epsilon(\mathbf{r},\omega)} \nabla \times \mathbf{H}(\mathbf{r},\omega) = \left(\frac{\omega}{c}\right)^2 \mathbf{H}(\mathbf{r},\omega) = k^2 \mathbf{H}(\mathbf{r},\omega), \tag{1.7}$$

we minimize the energy of the associated functional

$$\frac{\langle \mathbf{H}, \hat{\Theta}\mathbf{H}\rangle}{\langle \mathbf{H}, \mathbf{H}\rangle} = \frac{\int d^3\mathbf{r} |\nabla \times \mathbf{E}(\mathbf{r},\omega)|^2}{\int d^3\mathbf{r}\epsilon(\mathbf{r},\omega)|\mathbf{E}(\mathbf{r},\omega)|^2}, \tag{1.8}$$

to obtain the frequency eigenvalues. One sees indeed that the electric field should be concentrated in regions of larger ϵ, whilst minimizing spatial oscillations. An extreme case of this effect, and the central feature of optical waveguides, is the *guided mode*. These modes feature a wave-number beyond the light-line of free space, which demands that a wave-number perpendicular must be complex and results in an evanescent wave exponentially decaying away from the waveguide, as can be seen in Fig. 1.1(b). To ensure orthogonality with other modes, there then must be a discrete number of guided modes for each frequency ω. For the common step-index material, one finds the boundary conditions for the field components normal and tangential to the surface across which the permitivity is discontinuous

$$(\mathbf{E}(\mathbf{r}^+,\omega) - \mathbf{E}(\mathbf{r}^-,\omega)) \times \hat{\mathbf{n}} = 0, \tag{1.9}$$

$$\epsilon(\mathbf{r}^+,\omega)\mathbf{E}(\mathbf{r}^+,\omega) = \epsilon(\mathbf{r}^-,\omega)\mathbf{E}(\mathbf{r}^-,\omega), \tag{1.10}$$

where $\mathbf{r}^\pm$ denotes the limit of position on either side of the interface, and $\hat{\mathbf{n}}$ is the unit normal. We see that for guided waves, not only is there an electric field outside of the waveguide for finite ϵ, but at the interface the region of *smaller* relative permitivity will have a *larger* field component, resulting in a larger overall intensity. This means that a significant portion of the field mode may be comprised of the *evanescent field* outside the waveguide, which can be strongly localized in the vicinity of the interface. This in particular allows the guided field to be efficiently interfaced with nearby media [62], as I explore in Chapter 2. It is common to guide light over large distances in addition to confining it, and in these cases dielectrics featuring low loss are the material of choice. The current limits in low-loss dielectrics are pushed by the likes of silicon and germanium [63], with refractive indices $n = \sqrt{\epsilon} \approx 4$ at optical wavelengths. For typical purposes, however, silica ($n \approx 1.45$ at optical wavelengths) is commonly used due to its cheapness and the well-established wealth of fabrication techniques available. Circular waveguides can be reliably fabricated with lengths of mm, and with radii on the order of 10s of nm, far below the free-space wavelength of optical light [63, 64]. In particular, an index $n > 1$ can allow guided light to be confined in the transverse plane beyond the diffraction limit (see Chapter 2)[8].

As will be elaborated on in Chapter 4, accompanying spatial confining of system modes is dispersion engineering of the energy landscape, often employed for light in photonic crystals [17]. Here, a discrete translational symmetry is imposed onto the refractive index profile of the system (see Fig. 1.1(c), for an example in lattices of waveguides). Bloch's theorem then applies, and the eigenvalue equation for Bloch waves $\mathbf{u}_\mathbf{k}(\mathbf{r}) = e^{-i\mathbf{k}\cdot\mathbf{r}}\mathbf{H}_\mathbf{k}(\mathbf{r})$ may be obtained

$$\hat{\Theta}_k(\mathbf{r})\mathbf{u}_\mathbf{k}(\mathbf{r}) = (i\mathbf{k} + \nabla) \times \frac{1}{\epsilon(\mathbf{r})}(i\mathbf{k} + \nabla) \times \mathbf{u}_\mathbf{k}(\mathbf{r}) = \left(\frac{\omega(\mathbf{k})}{c}\right)^2 \mathbf{u}_\mathbf{k}(\mathbf{r}), \tag{1.11}$$

with $\mathbf{u}_\mathbf{k}(\mathbf{r}+\mathbf{R}) = \mathbf{u}_\mathbf{k}(\mathbf{r})$, for any lattice vector $\mathbf{R}$ in real space and the quasimomentum vector $\mathbf{k}$ in the Brillouin zone (BZ). The dispersion is revealed by the dependence of ω on $\mathbf{k}$, which is in general different to the dispersion $\omega(\mathbf{k}) = c|\mathbf{k}|$ of free space, as can be seen for the example in Fig. 1.1(c,d). The modified dispersion can have stark consequences on the resulting travelling waves, manifest as phenomena analogous to those in crystalline condensed matter systems:

- Waves travelling in certain directions (i.e., with a certain group velocity $\mathbf{v}(\mathbf{k}) = \nabla\omega(\mathbf{k})$) or even in all directions may be forbidden at a given frequency. As a consequence, incident waves with frequency lying in this *band gap* are then reflected, resulting in a dielectric mirror
- Light may be slowed down due to the correspondingly low group velocity $\mathbf{v} \to \mathbf{0}$ near a band edge. The density of states $D(\Delta) = \frac{1}{(2\pi)^d}\int_{\mathrm{BZ}} d^d\mathbf{k}\delta(\Delta - \omega(\mathbf{k}))$ (in d-D) may also be non-smooth in general – a *Van Hove singularity*
- Berry curvature corresponding to adiabatic changes in $\mathbf{k}$ can give rise to artificial magnetic fields for light, mimicking single-particle topological phenomena under focus in condensed matter systems, and allowing the platform to act as a natural analogue simulator.

Photonic crystal (waveguides) are also routinely fabricated with sub-wavelength transverse length scales in the optical regime, typically featuring refractive indices of $2 \leq n \leq 4$ [65, 66, 67].

The family of dielectric waveguides form foundational platforms in which guided light may be shaped in the spatial and temporal domain. On the purely optical front, interest lies in using low-loss dielectric waveguides (such as the silica optical fiber, see Chapter 3) to transport information for computational applications [68, 69] and, in the case of periodic media, exploiting the dielectric mirror effect to produce all-dielectric optical cavities [70, 71]. The real power of these optical platforms, however, lies in their ability interface with, and mediate interactions in, neighbouring matter.

1.2 Classical light-matter interaction: the Green's function

Light-matter interactions are realised in a host of systems, including cold atoms [72], quantum dots [73], defects in solid state [74], superconducting qubits [59], and excitons in (say) semiconductor cavities [75]. The influence of light on the emitter allows one to tailor the resonance and decay rate of emitters by structuring of the EM bath, whilst the spatially-dependent potential further results in forces on the emitters, unlocking control over spatial degrees of freedom. Turning the situation on its head with reciprocity, the point-like emitters may also be used to shape the light further, acting as nanoscale antennae that can interface far- and near-field radiation. Emission engineering is particularly relevant in probing matter at the nanoscale, whilst judiciously placed emitters can be used to construct metasurfaces with exotic and tunable optical responses [11, 29, 76]. This is so far to say nothing of the additional tools available when quantum degrees of freedom are considered.

In most of this thesis only a single quanta will be considered present in the system, so that any quantum nonlinearity is not probed and the system can be considered classically. An exception to this will be the dispersion potential explored in Chapter 2. I thus first discuss the interaction between a classical induced oscillating dipole and an EM field, from which the quantization scheme and quantum light-matter interaction analysis naturally follows. The equation of motion for the classical electric field is obtained after eliminating the magnetic field, now in the presence of a polarization source

$$\nabla \times \nabla \times \mathbf{E}(\mathbf{r},\omega) - k^2\epsilon(\mathbf{r},\omega)\mathbf{E}(\mathbf{r},\omega) = \mu_0\omega^2\mathbf{P}(\mathbf{r},\omega) = \mu_0\omega^2\mathbf{P}_0(\omega)\delta(\mathbf{r}-\mathbf{r}_0). \quad (1.12)$$

The (point-like) polarization density is given by $\mathbf{P}(\mathbf{r},\omega) = \mathbf{P}_0(\omega)\delta(\mathbf{r}-\mathbf{r}_0)$ for the delta function $\delta(\cdot)$ with corresponding polarization $\mathbf{P}_0$. By linearity, one can obtain the field for any distribution of current, via decomposing into point-like dipolar sources; the associated Green's function containing all information on dipole radiation is given as the solution to the equation [77]

$$\nabla \times \nabla \times \mathbf{G}(\mathbf{r},\mathbf{r}',\omega) - k^2\epsilon(\mathbf{r},\omega)\mathbf{G}(\mathbf{r},\mathbf{r}',\omega) = \mathbf{I}\delta(\mathbf{r}-\mathbf{r}'), \quad (1.13)$$

with inverse units of length, and for the identity matrix $\mathbf{I}$. One recovers the electric field from the general polarization density as follows including a homogeneous component $\mathbf{E}_0$ corresponding to no sources

$$\mathbf{E}(\mathbf{r},\omega) = \mathbf{E}_0(\mathbf{r},\omega) + \mu_0\omega^2 \int d^3\mathbf{r}'\mathbf{G}(\mathbf{r},\mathbf{r}',\omega)\cdot\mathbf{P}(\mathbf{r},\omega), \quad (1.14)$$

with the particularly simple expression for the point-like source with no homogeneous field component

$$\mathbf{E}(\mathbf{r},\omega) = \mu_0\omega^2\mathbf{G}(\mathbf{r},\mathbf{r}',\omega)\cdot\mathbf{P}_0(\omega). \quad (1.15)$$

The Green's function thus contains all the information on the propagation of dipole radiation *given a background medium* $\epsilon(\mathbf{r},\omega)$. The Green's function takes an intuitive form in the case of negligible loss (real ϵ) and for non-dispersive material $\epsilon(\mathbf{r},\omega) = \epsilon(\mathbf{r})$: with the resulting Hermitian problem of Eq. (1.15), one can readily verify the expansion into normalized field modes $\tilde{\mathbf{E}}_\mu$ [60]

$$\mathbf{G}(\mathbf{r},\mathbf{r}',\omega) = \frac{1}{k^2}\sum_\mu \left(\frac{\omega_\mu^2}{\omega_\mu^2-\omega^2}\right)\tilde{\mathbf{E}}_\mu(\mathbf{r})\otimes\tilde{\mathbf{E}}_\mu(\mathbf{r}') - \frac{1}{k^2}\frac{\delta(\mathbf{r}-\mathbf{r}')}{\epsilon(\mathbf{r})}\mathbf{I}, \quad (1.16)$$

for the normalization

$$\int d^3\mathbf{r}\epsilon(\mathbf{r})\tilde{\mathbf{E}}_\mu^*(\mathbf{r})\cdot\tilde{\mathbf{E}}_{\mu'}(\mathbf{r}) = \delta_{\mu\mu'}. \quad (1.17)$$

I note here that the *transverse* part of the Green's tensor has the form

$$\mathbf{G}^{(T)}(\mathbf{r},\mathbf{r}',\omega) = \sum_\mu \left(\frac{c^2}{\omega_\mu^2-\omega^2}\right)\tilde{\mathbf{E}}_\mu(\mathbf{r})\otimes\tilde{\mathbf{E}}_\mu(\mathbf{r}'), \quad (1.18)$$

where the sums in Eqs. (1.16) and (1.18) are only over transverse (physical) modes with $\nabla\cdot\left(\epsilon\mathbf{E}_\mu\right) = 0$, and satisfying the usual equation

$$\nabla \times \nabla \times \mathbf{E}_\mu(\mathbf{r}) - k^2\epsilon(\mathbf{r})\mathbf{E}_\mu(\mathbf{r}) = 0. \quad (1.19)$$

In the present discussion with ϵ real and frequency-independent, $\Im[\mathbf{G}] = \Im[\mathbf{G}^{(T)}]$ [78], so that consideration of the transverse Green's tensor $\mathbf{G}^{(T)}$ is sufficient for the imaginary part [79, 80]. In general, the full Green's function $\mathbf{G}$, with the implicit inclusion of non-physical (longitudinal) modes $\nabla \cdot \left(\epsilon \mathbf{E}_\mu\right) \neq 0$, should be used for $\mathbf{r} \neq \mathbf{r}'$ [81, 82], which results in a different value for the real part. In any case, the above expressions then show that the Green's function simply couples all valid fields to the dipole, which are then propagated away with a mode dependent weight. I finally note the often-used decomposition of the Green's function [77, 83, 84, 85]

$$\mathbf{G}(\mathbf{r}, \mathbf{r}', \omega) = \mathbf{G}^{(0)}(\mathbf{r}, \mathbf{r}', \omega) + \mathbf{G}^{(R)}(\mathbf{r}, \mathbf{r}', \omega), \tag{1.20}$$

where $\mathbf{G}^{(0)}$ is the vacuum Green's function

$$\begin{aligned}\mathbf{G}^{(0)}(\mathbf{r}, \mathbf{r}', \omega) = -\tfrac{1}{3k^2}\delta(\mathbf{r} - \mathbf{r}')\mathbf{I} \\ + \tfrac{\exp(ikR)}{4\pi R}\left[\tfrac{k^2R^2 + ikR - 1}{k^2R^2}\mathbf{I} + \tfrac{3 - 3ikR - k^2R^2}{k^2R^2}\hat{\mathbf{R}} \otimes \hat{\mathbf{R}}\right],\end{aligned} \tag{1.21}$$

and $\mathbf{G}^{(R)}$ is the reflected (or scattered) part that depends on the medium. For a homogeneous bulk electric, one makes the replacement $k \to kn(\omega) = k\sqrt{\epsilon(\omega)}$ with the complex square root chosen such that the material is absorbing, i.e., $\Im[k] > 0$. The vacuum self Green's function exhibits a divergence in the real part $\Re[\mathbf{G}^{(0)}(\mathbf{r}, \mathbf{r}, \omega)] \to \infty$, due to assumption of a point-like dipole resolving arbitrarily high wavenumbers, and when evaluating both arguments at the same point, one makes the replacement

$$\Re[\mathbf{G}(\mathbf{r}, \mathbf{r}, \omega)] \to \Re[\mathbf{G}^{(R)}(\mathbf{r}, \mathbf{r}, \omega)], \tag{1.22}$$

as the self-Green's function is finite for the reflected part (except in the case where the atom lies at an interface), whilst the full imaginary part remains finite with (for real k) $\Im[\mathbf{G}_0(\mathbf{r}, \mathbf{r}, \omega)] = \frac{k}{6\pi}\mathbf{I}$. Indeed, the renormalization of the real part arising from the vacuum is typically much smaller than that of the scattered part in practice [86]. In the rest of this thesis I use the notation $\mathbf{G}(\mathbf{r}, \mathbf{r}, \omega)$ with the replacement of Eq. (1.22) implicitly assumed.

As mentioned, the Green's function contains all information on wave propagation in the medium, and salient system features can typically be immediately inferred from the form of the Green's function. I briefly highlight a few key examples of the Green's function in qualitatively different media to show how the medium characteristics are manifest in the resulting wave propagation.

The Green's function in the case of an optical cavity resonant at ω_0, with decay rate κ, and with a single resonant cavity mode $\mathbf{E}(\mathbf{r})$ takes the approximate form [60]

$$\mathbf{G}_{\text{cavity}}(\mathbf{r}, \mathbf{r}', \omega) \approx \left(\frac{c^2}{2\omega_0(\omega - \omega_0 - i\kappa/4)}\right)\mathbf{E}(\mathbf{r}) \otimes \mathbf{E}^*(\mathbf{r}'), \tag{1.23}$$

which immediately shows that a Lorentzian peak around resonance and the coherent single-mode nature of propagation can be observed. The cavity modes typically feature a sinusoidal dependence along the cavity axis coordinate, so that propagation within the cavity is in principle without attenuation. For a single-mode 1D waveguide with periodicity length a along the waveguide axis with coordinate z, the Green's function [60, 82]

$$\mathbf{G}_{\mathrm{1D}}(\mathbf{r},\mathbf{r}',\omega) = \frac{iac^2}{2\omega v}\Big[\mathbf{E}_k(\mathbf{r}) \otimes \mathbf{E}^*_k(\mathbf{r}')\Theta(z-z') + \mathbf{E}^*_k(\mathbf{r}) \otimes \mathbf{E}_k(\mathbf{r}')\Theta(z'-z)\Big], \tag{1.24}$$

is obtained for the mode $\tilde{\mathbf{E}}_k(\mathbf{r})$ with a quasi-momentum (or effective wave-vector in the case of continuous translational symmetry) k, group velocity $v = v(k)$, and where $\Theta(\cdot)$ is the Heaviside function. Eq. (1.24) captures the essential features of waves in 1D – notably the infinite range propagation, inverse scaling with mode area (noting that $\tilde{\mathbf{E}}$ has inverse dimensions of square-root-volume), and potential for chiral light-matter interactions – when $\tilde{\mathbf{E}}_k(\mathbf{r})$ exhibits a slowly varying field envelope along the z-axis, the field longitudinal component is $\pi/2$ out of phase with the transverse component [87]. This feature allows one to select a dipole with (say) $\mathbf{P}_0(\omega)\cdot\tilde{\mathbf{E}}_k(\mathbf{r}) = 0$, and $\mathbf{P}_0(\omega)\cdot\tilde{\mathbf{E}}^*_k(\mathbf{r}) \neq 0$. The result according to Eqs. (1.24) and (1.15) is chiral emission with the field only non-zero for $z' > z$. This remarkable result is the cornerstone of *chiral quantum optics*, which employs symmetry breaking in the flow of light for applications in information processing [88] on one hand and fundamental studies of cascaded quantum systems [87, 89, 90] on the other. A final example noted for reference in Chapter 4 is the Green's function for ω just (say) above the band edge of a one-dimensional band-gap material. One approximates the dispersion in the vicinity of the band edge at k_0 by [28, 91]

$$\omega(k) = \omega_b[1 - \alpha(k-k_0)^2/k_0^2], \tag{1.25}$$

where α characterises the band curvature [91], and ω_b is the band edge frequency. Assuming small detuning $\Delta = \omega - \omega_b > 0$ above the edge, that the Green's function is dominated by contribution exclusively due to this band, and that the polarization of Bloch waves varies little around k_0, an approximation

$$\mathbf{G}_{\mathrm{BG}}(\mathbf{r},\mathbf{r}',\omega) \approx \frac{La}{2}\Re[\mathbf{E}_{k_0}(\mathbf{r}) \otimes \mathbf{E}^*_{k_0}(\mathbf{r}')]e^{-|z-z'|/L}, \tag{1.26}$$

can be obtained in a similar manner to that presented in [28] by approximating the integral corresponding to Eq. (1.16). The localization length is given by $L = \sqrt{\frac{\alpha\omega_b}{\Delta k_0^2}}$, for the detuning $\Delta = \omega - \omega_b > 0$. Notably, the Green's function is purely real, and exponentially decaying due to the inability of photons with frequency ω to travel – any radiation from the emitter will form a localized 'cloud', and power is forbidden from being radiated away from the dipole. Nonetheless, the evanescent field still allows the emitter to probe and interact with its surrounding. That $\mathbf{G}_{\mathrm{BG}}$ is real indicates the absence of travelling waves at ω, and is further suggestive of reversible dynamics. Indeed, this scenario is central to band-gap quantum optics [28, 92, 93] that seeks to engineer long-range and coherent interactions between quantum emitters.

Moving beyond emission of a constant dipole, the interplay between light and matter becomes apparent when, in addition to the dipolar emission Equation (1.15), one considers an induced linear dipole at position $\mathbf{r}_0$ such that

$$\mathbf{P}_0(\omega) = \alpha(\omega)\mathbf{E}(\mathbf{r}_0, \omega), \tag{1.27}$$

with (scalar) polarizability $\alpha(\omega)$. Including a driving field $\mathbf{E}_0$, one obtains a non-trivial and self-consistent system of equations for both the polarization $\mathbf{P}_0$ and the resulting electric field, specifically

$$\mathbf{P}_0(\omega) = \alpha(\omega)\left[\mathbf{I} - \alpha(\omega)\frac{k^2}{\epsilon_0}\mathbf{G}(\mathbf{r}_0, \mathbf{r}_0, \omega)\right]^{-1}\mathbf{E}_0(\mathbf{r}_0, \omega) = \alpha_{\text{eff}}(\omega)\mathbf{E}_0(\mathbf{r}_0, \omega), \tag{1.28}$$

that is, the polarizability is renormalized to α_{eff} by the presence of the medium, with a corresponding total electric field at frequency ω of

$$\mathbf{E}(\mathbf{r}, \omega) = \mathbf{E}_0(\mathbf{r}, \omega) + \mu_0\omega^2\alpha_{\text{eff}}(\omega)\mathbf{G}(\mathbf{r}, \mathbf{r}_0, \omega) \cdot \mathbf{E}_0(\mathbf{r}_0, \omega). \tag{1.29}$$

When multiple emitters are present, collective modes of the linear system are formed and, employed en masse, optical elements such as mirrors with sharply peaked responses may be formed [11, 29]. On the other hand, the average optical force acting on a polarizable particle is given for a total field $\mathbf{E}$ by

$$\mathbf{F} = \frac{1}{2}\Re\Big[\mathbf{P}_0 \cdot \nabla\mathbf{E}(\mathbf{r}_0)\Big], \tag{1.30}$$

so that through Eq. (1.29), the optical force may be shaped on an emitter via its environment – a common theme in optical nanofiber (ONF) optics (see Chapter 2) and in plasmonics, where atoms can be trapped by the strongly confined near-field of nanotips to precisions of nanometers [94]. Of course, multiple scattering also results in forces on each of the emitters that are dependent on the total configuration, creating a rich playground for investigating collective optomechanics of levitated nanoparticles [95, 96]. In these latter scenarios the background medium is often used to engineer strong and long range interactions between the emitters (see Eq. (1.24)).

1.3 Field quantization in arbitrary electric linear media

Theoretical machinery has grown more sophisticated since the early quantization schemes in a box [97], leading to the subsequent quantization in lossless continuum media [98], and eventually arbitrary linear electric media [99, 100, 101] which employ the classical EM Green's tensor (1.13). These general quantization schemes lay the foundation for studies of light-matter interactions in the presence of electric linear media, and the applicability of these Green's-function based methods becomes evident through the wealth of literature that employ them to this day in engineering emission and interactions in spin systems [28, 52, 53, 102, 103, 104, 105, 106], in determining transport/transfer of spin excitations [107, 108, 109], in determining optical properties of emitter-based metasurfaces [29, 76], and more. The equation for the quantum electric field $\hat{\mathbf{E}}(\mathbf{r},\omega)$ for a given frequency component at frequency ω and position $\mathbf{r}$ reads as that of the classical field in the presence of quantum noise currents $\hat{\mathbf{j}}(\mathbf{r},\omega)$

$$\nabla \times \nabla \times \hat{\mathbf{E}}(\mathbf{r},\omega) - \frac{\omega^2}{c^2}\epsilon(\mathbf{r},\omega)\hat{\mathbf{E}}(\mathbf{r},\omega) = i\omega\mu_0\hat{\mathbf{j}}(\mathbf{r},\omega). \tag{1.31}$$

In general the frequency-dependent permitivity $\epsilon(\mathbf{r},\omega)$ is complex, precluding the immediate quantization of the classical Maxwell's equations due to non-Hermiticity of the eigenvalue problem. One addresses the damping that would then arise in $\hat{\mathbf{E}}$ (and consequently, the bosonic operators) via the introduction of accompanying noise induced by local current fluctuations in $\hat{\mathbf{j}}$, consistent with the fluctuation-dissipation theorem. The electric field is found as the propagated current

$$\hat{\mathbf{E}}(\mathbf{r},\omega) = i\omega\mu_0 \int d^3\mathbf{r}' \mathbf{G}(\mathbf{r},\mathbf{r}',\omega)\cdot\hat{\mathbf{j}}(\mathbf{r}',\omega). \tag{1.32}$$

In the following I address only the electric field, as the magnetic component follows similarly and I will only consider the electric dipole interaction when investigating the light-matter Hamiltonian in any case. The noise is then decomposed into bosonic fields

$$\hat{\mathbf{j}}(\mathbf{r},\omega) = \omega\sqrt{\frac{\hbar\epsilon_0}{\pi}\mathrm{Im}\epsilon(\mathbf{r},\omega)}\hat{\mathbf{f}}(\mathbf{r},\omega), \tag{1.33}$$

satisfying the bosonic commutation relations

$$[\hat{\mathbf{f}}(\mathbf{r},\omega), \hat{\mathbf{f}}^{+}(\mathbf{r}',\omega')] = \mathbf{I}\delta(\mathbf{r}-\mathbf{r})\delta(\omega-\omega'). \tag{1.34}$$

Consideration of the EM field energy gives the Hamiltonian as the sum of harmonic oscillators

$$\hat{H} = \int d^3\mathbf{r} \int_0^\infty d\omega\hbar\omega\hat{\mathbf{f}}^{+}(\mathbf{r},\omega)\hat{\mathbf{f}}(\mathbf{r},\omega). \tag{1.35}$$

The quantization of the field is particularly relevant in periodic media as an analogy to the *tight-binding* model can be drawn, establishing a connection between the solid-state and optics. I present this connection in the following for reference in Chapter 4. In periodic, lossless, and dispersionless media, one can obtain the Hamiltonian in second quantization expansion similar to (1.35) but in terms of the Bloch waves of the system

$$\hat{H} = \hbar\sum_{\mu\mathbf{k}} \omega_\mu(\mathbf{k})\hat{a}^{+}_{\mu\mathbf{k}}\hat{a}_{\mu\mathbf{k}}, \tag{1.36}$$

for the photon annihilation operator $\hat{a}_{\mu\mathbf{k}}$ acting on the photon of the μ-th band of the system with quasimomentum $\mathbf{k}$. Note that I neglect the continuum of modes that are not guided. In this case, the Wannier basis can be constructed

$$\hat{a}_{\mu j} = \frac{1}{\sqrt{N}}\sum_{\mathbf{k}} e^{i\mathbf{k}\cdot\mathbf{R}_j}\hat{a}_{\mu\mathbf{k}}, \tag{1.37}$$

where the set $\{\mathbf{R}_j\}_j$ is a set of lattice sites of size $N \to \infty$ for the system. One then obtains the tight-binding form of the Hamiltonian

$$\hat{H} = \hbar \sum_{\mu} \sum_{jk} J_{\mu jk} \hat{a}^{+}_{\mu j} \hat{a}_{\mu k}, \tag{1.38}$$

for

$$J_{\mu jk} = \hbar \sum_{\mathbf{k}} \omega_{\mu}(\mathbf{k}) e^{i\mathbf{k}\cdot(\mathbf{R}_j - \mathbf{R}_k)}, \tag{1.39}$$

which can also be written as an overlap integral between the corresponding Wannier functions for the EM field [110]. That is, a photon hops between orbitals corresponding to localized Wannier functions localized at each lattice cell. As Wannier functions are typically exponentially decaying [111], one often neglects site interactions beyond nearest neighbor, and in addition assumes low energies so that higher bands can be neglected.

Given the great degree of controlability of state-of-the-art in photonics, one has a great freedom in engineering bosonic Hamiltonians in both the continuum and discrete settings. When the quantum degree of freedom is considered for both field and emitter, the interplay between a bosonic bath and the emitters can be explored similarly to the classical case including induced polarizability, as we see in the following.

1.4 Atom-field equations of motion

I begin with the paradigmatic light-matter dipolar coupling Hamiltonian that can be derived from the microscopic system of charges [77], in the case of many distinct two-level systems (TLS), which are here concretely taken to be atoms. The system reads

$$\hat{H} = \hat{H}_{\text{field}} + \hat{H}_{\text{atom}} + \hat{H}_{\text{int}}, \tag{1.40}$$

with the constituents

$$\hat{H}_{\text{field}} = \int d^3\mathbf{r} \int_0^{\infty} d\omega \hbar\omega \hat{\mathbf{f}}^{+}(\mathbf{r},\omega)\hat{\mathbf{f}}(\mathbf{r},\omega), \tag{1.41}$$

$$\hat{H}_{\text{atom}} = \tfrac{1}{2} \sum_j \hbar\omega_0 \sigma^z_j, \tag{1.42}$$

$$\hat{H}_{\text{int}} = -\sum_j \hat{\mathbf{D}}_j \cdot \hat{\mathbf{E}}(\mathbf{r}_j), \tag{1.43}$$

for the dipole operator $\hat{\mathbf{D}}_j$, and the Pauli spin-1/2 operator (matrix) $\hat{\sigma}^{\alpha}_j$ acting on atom j for two level atoms characterised by ground ($|g\rangle$) and excited ($|e\rangle$) states with resonant frequency ω_0. With no permanent dipole moment, the dipole operator must necessarily take the form

$$\hat{\mathbf{D}}_j = \mathbf{d}^* \sigma^{+}_j + \mathbf{d}\sigma_j = \hat{\mathbf{D}}^{+}_j + \hat{\mathbf{D}}^{-}_j, \tag{1.44}$$

with the associated dipole matrix element $\mathbf{d} = \langle g|_j \hat{\mathbf{D}}_j |e\rangle_j$ and lowering operator $\sigma_j = |g\rangle_j \langle e|_j$. In the Heisenberg picture, the equation of motion for the positive-frequency component $\hat{\mathbf{E}}^+$ of the electric field is obtained as

$$\dot{\hat{\mathbf{E}}}^+(\mathbf{r},\omega,t) = i\omega\hat{\mathbf{E}}^+(\mathbf{r},\omega,t) + \frac{i\mu_0\omega^2}{\pi}\sum_{j=1}^{N}\Im[\mathbf{G}(\mathbf{r},\mathbf{r}_j,\omega)]\cdot\hat{\mathbf{D}}_j^+(t). \tag{1.45}$$

In the limit of weakly saturated atoms $\sigma_j^z \approx -1$, one integrates and obtains the quantum analogue of Eq. (1.15) [86]

$$\hat{\mathbf{E}}^+(\mathbf{r},\omega) = \hat{\mathbf{E}}_0^+(\mathbf{r},\omega) + \mu_0\omega^2\sum_j \mathbf{G}(\mathbf{r},\mathbf{r}_j,\omega)\cdot\hat{\mathbf{D}}_j^+(\omega), \tag{1.46}$$

with the feedback onto the atomic dipole (ignoring the initial atomic contribution) entering through [53, 60, 86]

$$\hat{\mathbf{D}}_j^+(\omega) = \boldsymbol{\alpha}(\omega)\cdot\hat{\mathbf{E}}^+(\mathbf{r}_j,\omega), \tag{1.47}$$

for the tensor polarizability associated with the transition [77]

$$\boldsymbol{\alpha}(\omega) = \frac{1}{\hbar}\Big[\frac{\mathbf{d}^*\otimes\mathbf{d}}{\omega+\omega_0+i0} - \frac{\mathbf{d}\otimes\mathbf{d}^*}{\omega-\omega_0+i0}\Big], \tag{1.48}$$

in agreement with classical intuition, and where $(\Delta+i0)^{-1} = \lim_{\epsilon\to0^+}(\Delta+i\epsilon)^{-1} = \mathcal{P}\big(\frac{1}{\Delta}\big) - i\pi\delta(\Delta)$, with $\mathcal{P}$ denoting the Cauchy principal value. In general, nonlinear coupling to higher-order cumulants in the Heisenberg equations precludes this correspondence. Eqs. (1.46) and (1.47) similarly give a self-consistent system of equations for the dipole operators and electric field, which results in a renormalization of the polarization for each emitter. In the Markov approximation, the atomic dipolar response is assumed to be sharply peaked around resonance, and the variation of the Green's function over this frequency range is assumed negligible. In addition, the travel time of photons between two emitters is considered negligible in comparison to the atomic timescales. Then, $\mathbf{G}$ becomes local in time, and one may make the replacement $\mathbf{G}(\mathbf{r},\mathbf{r}',\omega) \to \mathbf{G}(\mathbf{r},\mathbf{r}',\omega_0)$ to find in the time domain (upon taking the rotating-wave approximation)

$$\hat{\mathbf{E}}^+(\mathbf{r},t) = \hat{\mathbf{E}}_0^+(\mathbf{r},t) + \mu_0\omega_0^2\sum_j \mathbf{G}(\mathbf{r},\mathbf{r}_j,\omega_0)\cdot\hat{\mathbf{D}}_j^+(t). \tag{1.49}$$

Alternatively, one may take a more dynamical approach in order to derive the equations of motion for the atomic population, without assuming weak-saturation of the atoms. Formally beginning instead from the original Hamiltonian (1.40) and applying the Born and Markov approximations of bath-spin factorization and a memoryless photonic environment gives an equation of motion coarse-grained over the fast bath time-scale for the reduced density matrix $\hat{\rho}$ of spins only [83, 102] in the interaction picture rotating as $\hat{U} = e^{i(\hat{H}_{\text{atom}}+\hat{H}_{\text{field}})t}$

$$\dot{\hat{\rho}} = \frac{-1}{\hbar^2}\int_0^\infty d\tau\big[\hat{H}_{\text{int}}(t),\big[\hat{H}_{\text{int}}(t-\tau),\hat{\rho}\otimes|0\rangle\langle0|\big]\big], \tag{1.50}$$

for the field vacuum state $|0\rangle$. One evaluates the exponentials appearing in the integral by

$$\int_0^\infty d\tau e^{-i\omega t} = \pi\delta(\omega) - i\mathcal{P}\frac{1}{\omega}, \tag{1.51}$$

to obtain the master equation

$$\dot{\rho} = -\frac{i}{\hbar}[\hat{H}_{\text{eff}}, \rho] + \mathcal{L}[\rho], \tag{1.52}$$

for the effective Hamiltonian and Linbladian

$$\hat{H}_{\text{eff}} = -\hbar \textstyle\sum_{j,k=1} \Omega_{jk}\hat{\sigma}_j^+\hat{\sigma}_k, \tag{1.53}$$

$$\mathcal{L}[\rho] = \tfrac{1}{2}\textstyle\sum_{j,k=1} \Gamma_{jk}\Big[\big[\hat{\sigma}_k, \rho\hat{\sigma}_j^+\big] + \big[\hat{\sigma}_k\rho, \hat{\sigma}_j^+\big]\Big]. \tag{1.54}$$

The coefficients determining coherent and incoherent spin exchanges respectively are given by

$$\Omega_{jk} = \tfrac{\mu_0\omega_0^2}{\hbar}\mathbf{d}^* \cdot \Re\mathbf{G}(\mathbf{r}_j, \mathbf{r}_k, \omega_0) \cdot \mathbf{d}, \tag{1.55}$$

$$\Gamma_{jk} = \tfrac{2\mu_0\omega_0^2}{\hbar}\mathbf{d}^* \cdot \Im\mathbf{G}(\mathbf{r}_j, \mathbf{r}_k, \omega_0) \cdot \mathbf{d}, \tag{1.56}$$

and are also known as the *resonant dipole-dipole interaction* (RDDI) elements. Note that if a driving field is present, one works in the rotating frame that produces an extra Hamiltonian term corresponding to detuning in Eqs. (1.53), whilst in the interaction elements Ω_{jk}, Γ_{jk}, one makes the replacement $\omega_0 \to \omega_L$ [83]. For typical detunings $\omega_0 - \omega_L \sim \Gamma_{jj}$, the variation of the Green's function is negligible and either can be taken. It is worth mentioning here the applicability of this setup for quantum simulations. Although TLSs have been considered to arrive at the flip-flop interactions – tunable through the photonic environment – in Eqs. (1.53), a wealth of interacting spin models with dynamical tunability can be created by employing a more complex atomic level structure and external driving fields for atoms situated in particular next to photonic crystals [26, 28, 112]. In platforms of one- and two-dimensional crystals coupled two cold atoms, the basic functionalities (atom trapping, interfacing, measurement) have been demonstrated [113, 114], suggesting steady progress towards the realization of engineered many-body quantum models in the near-future.

Beyond the interactions of Eq. (1.53) obtained in the rotating wave approximation, I note for reference in Chapter 3 that at second order in the atom-field coupling strength, one in general finds also a single-emitter ground state energy shift due to the presence of the medium [77, 83]

$$\begin{aligned}\Omega_{jj} \to \Omega_{jj} &+ \tfrac{\mu_0}{\hbar\pi}\textstyle\int_0^\infty du \tfrac{u^2\omega_0}{\omega_0^2+u^2}\mathbf{d}^* \cdot \mathbf{G}(\mathbf{r}_j, \mathbf{r}_j, iu) \cdot \mathbf{d} \\ &= \Omega_{jj} + \tfrac{\mu_0}{2\pi}\textstyle\int_0^\infty du u^2 \text{Tr}\big[\boldsymbol{\alpha}(iu)\mathbf{G}(\mathbf{r}_j, \mathbf{r}_j, iu)\big],\end{aligned} \tag{1.57}$$

which requires that the rotating-wave approximation *not* be taken. This shift is typically small compared to other quantities, but generically becomes significant as the atom-surface distance is reduced – as an example, Caesium atoms next to an infinite silica half-space in the non-retarded limit feel the potential [77, 115]

$$U(z) \sim \frac{C_3}{z^3}, \tag{1.58}$$

for the van der Waals coefficient $C_3 = 5.6 \times 10^{-49}$ Jm^3, and where z denotes distance of the atom to the half-space boundary. This already corresponds to a ground-state energy shift of 1 MHz= $O(\Gamma_0/2\pi)$ when $z \approx 174$ nm, sub-wavelength with respect to the dominant optical transitions $\lambda_0 \sim 1\mu$ m. In the context of trapping this corresponds to a temperature of approximately 7.64 μK, but when $z \approx 34$ nm the shift corresponds to a temperature of approximately 1 mK and the strong atom-surface attraction then typically overcomes laser-induced trapping potentials [22, 115], resulting in trapping limited by dispersion to atom-surface distances on the order of 100nm for Caesium atoms [114] next to dielectrics with a moderate refractive index. Whilst the dispersion potential here is found at second order in atom-field coupling and acts only on a single atom, I will explore in Chapter 2 the two-atom dispersion potential that can be found at fourth order.

1.4.1 Collective modes: superradiance and subradiance

A recurring theme in this thesis will be the collective modes of coupled systems, be it the joint modes of a two-fiber coupler (Chapter 2), or the collective excitations of atoms mediated through the EM field (Chapters 3 and 4). Concretely, in the previous example of atoms coupled through the field, the collective modes are can be readily analyzed in the single excitation subspace. Recalling the Heisenberg equation of motion for operators corresponding to Eq. (1.53), one obtains the linear set of equations [53]

$$\dot{\boldsymbol{\sigma}} = i\left(\boldsymbol{\Omega} + \frac{i}{2}\boldsymbol{\Gamma}\right)\boldsymbol{\sigma} = i\mathbf{g}\boldsymbol{\sigma}, \tag{1.59}$$

where we have the vector of atomic coherence expectations $\boldsymbol{\sigma} = (\langle\sigma_1(t)\rangle, \ldots, \langle\sigma_n(t)\rangle)$ and matrices $\boldsymbol{\Omega} = [\Omega_{jk}]_{jk}, \boldsymbol{\Gamma} = [\Gamma_{jk}]_{jk}$. The real and imaginary part of the eigenvalues of the matrix $\boldsymbol{g}$ will then determine the collective resonances and decay rates respectively, with the eigenvector giving the profile $\boldsymbol{\sigma}$ of spin coherences. In particular, any collective decay rate Γ is restricted by $0 \leq \Gamma \leq \sum_j \Gamma_{jj}$, with saturation of the left inequality yielding *subradiant* collective states and the saturation of the right inequality yielding *superradiant* states. These two situations showcase the extremes of collective radiation of emitters with, in the case of identical emitters, either an N-fold (for N atoms) enhancement of decay rate, or a perfectly non-radiating state that does not decay. (Note that the dynamical superradiant decay is not to be confused with the phenomenon of steady-state superradiance in the Dicke model of cavity QED, to be touched upon in Chapter 3.) A transparent example of this behaviour can be observed in cavity QED. Assuming the standard longitudinal $\cos(kz)$ dependence of the cavity mode field, one can obtain the RDDI interaction elements from (1.23) in a driven cavity (with the fast cavity eliminated [53]) as

$$\begin{aligned} \Omega_{jk} &= -\tfrac{g^2\Delta_c}{\Delta_c^2+\kappa^2/4}\cos(kz_j)\cos(kz_k), & (1.60)\\ \Gamma_{jk} &= \tfrac{g^2\kappa}{\Delta_c^2+\kappa^2/4}\cos(kz_j)\cos(kz_k), & (1.61) \end{aligned}$$

where g is the atom-cavity coupling, κ is the cavity decay rate and $\Delta_c = \omega_p - \omega_c$ is the detuning between the cavity frequency ω_c and the probe field frequency ω_p. Regardless of emitter position, there is then always a single superradiant mode that couples to the cavity field

$$\sigma_j \propto \cos(kz_j), \qquad \Omega + i\Gamma/2 = \frac{g^2(-\Delta_c + i\kappa/2)}{\Delta_c^2 + \kappa^2/4}\sum_{j=1}^{n}\cos^2(kz_j), \tag{1.62}$$

and $n-1$ subradiant modes that are decoupled. For emitters placed at antinodes, and assuming resonance $\Delta_c = 0$, one constructs the collective spin operator

$$\hat{S} = \frac{1}{\sqrt{N}}\sum_{j=1}^{n}\hat{\sigma}_j, \tag{1.63}$$

to obtain the Linbladian

$$\mathcal{L}[\rho] = \frac{\Gamma}{2}\Big(\big[\hat{S}\rho, \hat{S}^{+}\big] + \big[\hat{S}, \rho\hat{S}^{+}\big]\Big), \tag{1.64}$$

which again reveals an enhancement of N in the decay rate of the superradiant mode over single-body emission. In addition to the immediate enhancement of emission into the cavity [116], superradiant emission has applications in quantum memories [117], lasing [118], and enhanced cooling schemes [119]. Superradiant decay has further been experimentally verified in a range of settings [37, 74, 120, 121]. Due to their inherent decoupling from the EM field, subradiant modes are more difficult to excite [122], but promise long-lived decoherence free subspaces [123] for information processing and 'tailored' subradiance may be used for information transport, e.g., to selectively excite desired modes of a neighboring optical nanofiber, whilst remaining decoupled from the undesired free-space modes [107].

Chapter 2

Optical Nanofibers for Light-Matter Interfaces

2.1 Background

The ONF is a simple extension of the optical fiber – a component ubiquitous in today's society – that can be obtained by heating and stretching [124, 125] a standard (typically silica) optical fiber to create a tapered region with a diameter of the order of 100s of nanometers. A schematic of the resulting structure is given in Fig. 2.1. After decades of progress in optical fiber technologies and their branching into ONFs, the current state-of-the-art standard allows silica ONFs with lengths of millimeters and a realised attenuation of $2.6{\times}10^{-5}$ dB/mm for wavelengths of 780 nm [126] to be routinely fabricated with radii at the waist of 200 nm [127], well below free-space optical wavelengths. ONFs support discrete electromagnetic modes guided by total internal reflection that feature evanescent fields (see Fig. 2.1), which exponentially decay outside of the fiber, and allow for external interfacing with matter. With the realisation of low-loss ONFs with a deeply-sub-wavelength diameter of 50 nm in 2003 [64], interest rekindled in extending the numerous applications of standard optical microfibers to nanoscale platforms. Similarly to optical micro-fibers, the ONF has found uses in light guiding as part of miniaturized optical circuits [128, 129], along with efficient couplers [130], resonators [32, 131], and optical sensors [30, 132, 133]. On the other hand, the interface provided by the evanescent field makes the ONF a powerful platform in the quantum optical realm when interfacing with emitters. Here the ONF boasts strong optical near fields for particle trapping [34, 115], guiding [134, 135, 136], and detection [133]. The significant coupling into the fiber also allows for efficient photon collection and generation [33, 62, 93] through the guided mode, whilst the infinite-range and strong interactions through the ONF realise the basic building block for a quantum information network [68, 69], and enable the simulation of a host of long-range and open many-body quantum systems in a 1D bath [7, 90, 137, 138]. Indeed, the broadband and open 1D nature of the ONF is a key distinguishing feature in comparison to, say, optical cavities. When considered alongside their low-cost and relative ease of integration with existing platforms, ONFs, (or 1D waveguides in general) have been cemented as an indispensable tool in realising flexible and powerful light-matter interfaces.

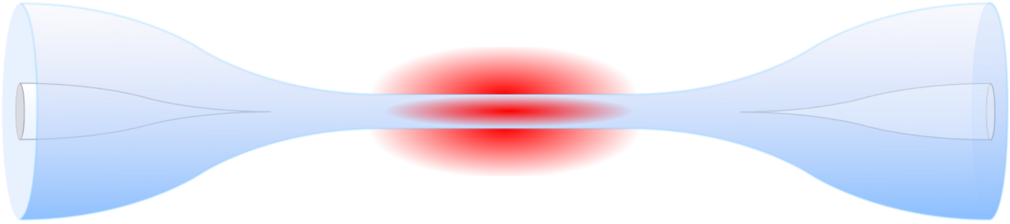

Figure 2.1: Schematic of a tapered optical fiber. The ONF (central region) is obtained by heating and stretching a standard optical fiber. The cladding (blue) of the original optical fiber becomes the core of the ONF, which is surrounded by a ‘cladding’ of vacuum. Red denotes a guided pulse of light, which extends outside as an evanescent field.

2.1.1 ONFs for sensing, measurements and interferometers

Aside from applications in quantum optics, ONFs excel in metrological applications and transporting and transforming information. A common role of ONFs is that of a coupler, allowing one to interface two spatially separated working components. A classic example is the coupling of Fabry-Perot optical cavities [139, 140, 141, 142], allowing high efficiency large bandwidth coupling, in addition to whispering gallery resonators [143, 144], where the guided modes of the ONF overcome phase-mismatching that occurs when attempting to excite cavity modes by free space beams. In fact, optical cavities can be formed from ONFs themselves [145, 146, 147, 148], which allows for long on-axis cavity lengths on the order of metres, as there are (ideally) no off-axis modes to carry away energy. Aside from their roles as passive optical elements, the ONF also plays a more central role when it comes to sensing and manipulation of matter present in the evanescent field. The base functionality of the light-matter interaction is that of a refractive index sensor, which is employed directly to measure the refractive index of gases [149], and indirectly in order to determine the positions and sizes of micro- and nano-particles [133, 150, 151] via scattering into fiber modes. Conversely, injecting light into the fiber further allows one to manipulate nearby particles [134, 135, 136, 152] due to the large component of electric field in the vicinity of the fiber. Recent all-optical applications of the ONF include twisted-fiber interferometers [32], measurement of the vdW potential [153], and measurement of the spin angular momentum of light [154]. More recently, ONFs have received a great deal of attention as a platform for interfacing light and (quantum) emitters.

2.2 ONFs coupled to neutral atoms

2.2.1 Trapping and interfacing of particles

To create an interface between light and matter, reliable trapping schemes that can localize single particles are an indispensable part of the quantum optical toolbox. Common laser trapping schemes make use of the induced dipole potential [83], where we assume a polarizable particle with a single resonance and a laser field detuned from resonance by Δ (cf. the optical force in Eq. (1.30))

$$U(\mathbf{r},\Delta) = -\frac{1}{2}\alpha(\Delta)|\mathbf{E}(\mathbf{r})|^2. \tag{2.1}$$

In the regime of large Δ, the polarizability (for projected dipole matrix element d) may be approximated as

$$\alpha(\Delta) = -\frac{d^2}{\hbar\Delta}, \tag{2.2}$$

due to the imaginary part scaling as $O(\Delta^{-2})$ [83, 115] – this feature ensures that high laser powers can be used to create deep trapping potentials without compromising incoherent scattering, provided detuning is large enough. Then, in evanescent-field trapping schemes, one may launch far red-detuned light through the ONF in order to attract atoms towards regions of high intensity near the surface where centrifugal forces provide a balancing force [155], or one may launch blue-detuned light to guide particles towards regions of low intensity, applied in ‘slot’-style (ONF) waveguides featuring a central intensity minimum [34, 61, 65]. In general geometries, one may launch both red- and blue-detuned light with distinct evanescent decay lengths to create a combination of attractive and repulsive forces, balancing near the surface of the dielectric: proposed for 1D waveguides in 2000 [156], the so-called *two-color* trap was theoretically treated for ONFs in 2004 [115], and has seen almost universal adoption in atom-ONF platforms [22, 120, 127, 157, 158], and also in 2D dielectric platforms [159, 160]. Here trapping depths on the order of mK can be achieved [22, 115]. Current state of the art allows Cesium atoms to be trapped for 1s and near the motional ground state (with ground-state occupation more than 50% in all three directions) 300nm from hot ONFs, using a combination of two-color traps and degenerate Raman cooling [158] to satisfy the sub-mK requirements demanded by the trap depth.

2.2.2 Collective response of quantum emitters to guided modes

ONF losses are negligible within typical fiber lengths of interest (1mm-1m), which means that emitters coupled to the ONF can interact over arbitrarily large distances – this feature lies at the heart of many quantum optical applications. Demonstrated theoretically in 2004 [161] for two emitters and in 2007 for many [162], the ONF guided modes allow for coherent interference between the emission of coupled emitters placed along the ONF. Neglecting for clarity the effective single-body emission into radiation modes, one can then describe the purely dissipative interactions in terms of a collective spin as in Eq. (1.64), resulting in super- (sub-)radiance when (anti)-symmetric states of the emitters are excited. Remarkably, despite the fact that the single-atom coupling Γ_{1D} into the ONF is typically small compared to the decay rate Γ' into non-guided vacuum modes, placing N atoms along the ONF allows the optical depth $\frac{N\Gamma_{1D}}{2\Gamma'}$ to be arbitrarily increased. For increasing N, the spin-wave corresponding to the superradiant mode has an overlap with the ONF guided mode closer and closer

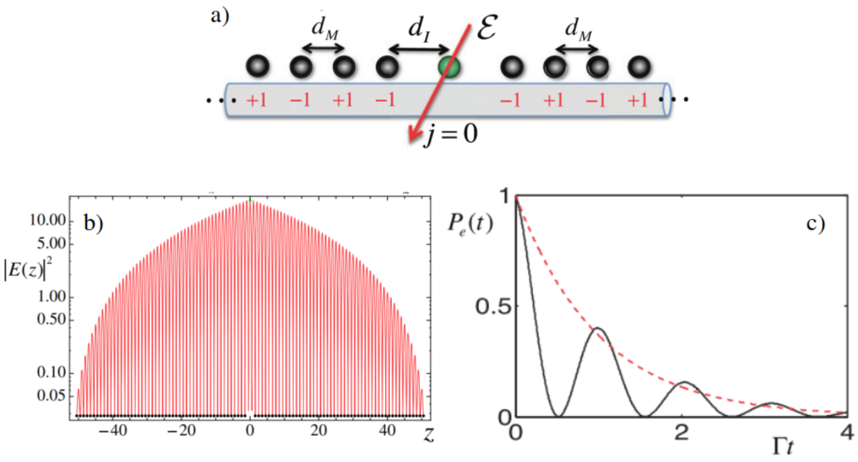

Figure 2.2: (a) Schematic for realising an effective cavity using two atomic mirrors of equally spaced atoms; the atoms with labelling ±1 form two superradiant collective modes that are π out of phase, producing an overall subradiant cavity mode, which the atom at $j = 0$ couples to. (b) Intensity profile of the effective cavity mode. (c) Rabi oscillations of an initially excited impurity atom placed in the effective cavity (black line) vs single-atom decay rate without the cavity atoms (dashed red line). Taken from [7].

to unity, with a channel efficiency

$$f = \frac{N\Gamma_{1D}}{\Gamma' + N\Gamma_{1D}}, \tag{2.3}$$

and $f = 0.96$ has been achieved for a chain of $N = 100$ Cesium atoms trapped at a distance of 100 nm from a ONF of radius $a = 200$ nm [162]. Note here that the decay Γ' into radiation modes in principle sets a bound on the collective spin lifetime, in contrast to the losses κ from the cavity mode. Whilst the single-body emission into radiation modes (typically on the order of ∼80-99%) cannot be neglected in practice, the ratio between coupling to radiation modes and collective coupling to the guided mode can be arbitrarily increased with increasing atom number, so that on relevant timescales the coupling to the guided mode is the dominant mechanism. Formation of superradiant atomic chains is at the core of collective-atom-fiber interfaces, and was experimentally observed in 2017 [121] for a cloud of atoms, whilst the associated large Bragg reflection of the array was observed in 2016 [157]. An early theoretical proposal for applications of this effect was to demonstrate an encompassing of cavity QED within waveguide QED, by realising atomic 'mirrors' using arrays of atoms trapped along the ONF ([7], see Fig. 2.2), and has been experimentally realised in the equivalent circuit QED of superconducting qubits in 2019 [59]. Coupling of the cavity mode to an impurity atom then scales as $\frac{\Gamma_{1D}\sqrt{N}}{2}$. Using a modest $N = 900$ and 20% coupling into the fiber $\Gamma_{1D} = \Gamma'/4$, the hallmark Rabi oscillations [163] of cavity QED are observed in the oscillation of the impurity population.

When employed in conjunction with 3-level Λ-type atoms, the large collective coupling allows a single and long-lived collective excitation to be stored within a superposition of two ground states of the atomic chain upon illumination through the fiber, and read out at will. This concept was explored in [7], and realised experimentally in [120]. This ability to control photons and interface with atoms at the single quantum level realises a foundation for quantum-information processing in atom-ONF systems, spurring on experimental progress aimed at bringing practical systems closer to realisation, in addition to fundamental physical investigations aiming to explore the functionalities available to the ideal atom-fiber system. To select a few, recent notable findings include the experimental generation of strongly bunched and anti-bunched light, using the non-linear photon-photon interactions mediated by atomic arrays [164]; realisation of mechanical analogues of the celebrated Dicke model (see Ch. 3) by using strong artificial magnetic field arising due to strong polarization gradients [165] that couple the motional atomic states to the spin states [166]; chiral amplifiers of ONF-guided-light [167] exploiting the spin-orbit coupling [87] of tightly confined fields.

2.3 Theory and principles of the ONF

One of the attractive qualities of the ONF is its amenity to theoretical treatment, which under mild modelling assumptions allows one to completely specify the system eigenmodes analytically. In the following we model an ONF as an infinite cylinder with a step-refractive index profile $n(\mathbf{r})$ surrounded by a vacuum and given in cylindrical coordinates $\mathbf{r} = (r, \varphi, z)$

$$n(\mathbf{r}) = \begin{cases} n_1 & r < a, \\ 1 & r > a, \end{cases} \tag{2.4}$$

for the fiber radius a and constant refractive index $n_1 > 1$, which for now we take to be real, given the low losses of silica in the optical wavelengths [126, 127]. The resulting eigenvalue problem (1.7) is Hermitian, and admits an orthonormal set $\{\mathbf{E}_\mu\}_\mu$ of field modes characterised by the super-parameter μ that we specify later. The ONF features translational invariance along the z-axis, along with rotational symmetry about the ONF axis, so solutions take the form

$$\mathbf{E}_\mu(\mathbf{r}) = \boldsymbol{\mathcal{E}}_\mu(x, y) e^{if\beta z} = \mathbf{e}_\mu(r) e^{i(f\beta z + l\varphi)}, \tag{2.5}$$

where $f = \pm 1$ indicates the direction of propagation, $l = \ldots, -2, 1, 0, 1, 2, \ldots$ is the azimuthal mode number, and $\beta = \beta(\mu)$ is the (conserved) propagation constant. Generally for 1D waveguides, the field components along the fiber axis (the *longitudinal* field components) decouple [16, 168]

$$\left(\nabla_\perp^2 + [k^2 n(x, y)^2 - \beta^2]\right) \begin{bmatrix} \mathcal{E}_{\mu z} \\ \mathcal{B}_{\mu z} \end{bmatrix} = 0, \tag{2.6}$$

for the transverse Laplacian $\nabla_\perp^2 = \nabla_x^2 + \nabla_y^2$, and the transverse components are readily obtainable as

$$\begin{bmatrix} \boldsymbol{\mathcal{E}}_{\mu\perp} \\ \boldsymbol{\mathcal{B}}_{\mu\perp} \end{bmatrix} = \frac{i}{n^2k^2 - \beta^2}\left(\beta + k \begin{bmatrix} 0 & -\left(\frac{\epsilon_0}{\mu_0}\right)^{1/2} \\ n^2\left(\frac{\mu_0}{\epsilon_0}\right)^{1/2} & 0 \end{bmatrix} \cdot \hat{\mathbf{z}} \times \right)\nabla_\perp \begin{bmatrix} \mathcal{E}_{\mu z} \\ \mathcal{B}_{\mu z} \end{bmatrix}. \tag{2.7}$$

The boundary conditions are the standard interface conditions for step-discontinuities in Maxwell's equations (Eqs. (1.9)) along with $\boldsymbol{\mathcal{E}}_\mu(x,y), \boldsymbol{\mathcal{H}}_\mu(x,y) \to 0$ at infinity in the transverse plane, completing the eigenvalue problem and allowing the nature of eigenmodes to be deduced as follows. As the ONF refractive index is $n_1 > 1$, and n_1 is the largest index in the system, it follows that the propagation constant is restricted to

$$|\beta| < kn_1. \tag{2.8}$$

If $|\beta| < k$, the wavevector is possible in free space (lies within the light line), and the wave is physically not guided by the ONF; in Eq. (2.6) we see that outside the fiber the longitudinal components may be expanded as outgoing and incoming Hankel waves, which decay weakly as $(x^2+y^2)^{-1/2}$ in the far-field. In this case we may specify each eigenmode by

$$\mu = (\beta, l, p, f), \tag{2.9}$$

where $\beta < |k|$ and $p = \pm 1$ describes the two polarizations. This continuum of eigenmodes with propagation constant within the light line are known as the *radiation modes*. On the other hand, one argues that a wave confined to the fiber core – the *guided modes* – allow

$$k < |\beta| < kn_1. \tag{2.10}$$

In this case, examination of (2.6) with Eq. (2.10) satisfied reveals the field outside the ONF may only be a single outgoing, and exponentially decaying, evanescent field, required for conservation of total wavevector. Therefore, a consistency condition for β must be satisfied [8, 16, 168], which is the eigenvalue problem for guided modes. For each specification of the fiber (radius a, refractive index n_1), and of the free-space wavevector k, there exist a finite number of β values satisfying the consistency condition, with the number of β values determined by the dimensionless fiber parameter

$$V = ka\sqrt{n_1^2 - 1}. \tag{2.11}$$

In the ONF a distinction can be made for the guided modes by mode type N describing the field polarizations: one finds hybrid (H) modes, modes in which both electric and magnetic fields have a component in the longitudinal direction; this may be contrasted with the transverse (T) modes, in which one of the electric or magnetic fields is entirely transverse. Within these categories we further specify the dominantly longitudinal field for hybrid modes, leading to labelling HE and EH for dominant electric and magnetic field respectively, whilst for the transverse fields we used notation TE (transverse electric) and TM (transverse magnetic) respectively. Within these mode specifications, the electric field is only further distinguished by distinct solutions β to the eigenvalues problem, which are labelled by $m = 1, 2, \ldots$ for each l, and again the polarization index $p = \pm 1$. The guided modes are then completely specified by the super-index

$$\mu = (k, N, l, m, p, f), \tag{2.12}$$

where $N =$ (HE,EH,TE,TM), and (l, m) may only take finitely many values for each k. Up to degeneracies in p and f, the mode type is typically written as N_{lm}. With these derivations complete, one numerically obtains the electric field profile by simply solving the nonlinear eigenvalue equation for β and inputting this into the electric field profiles obtainable from (2.6) and (2.7). A plot of the effective wave numbers available for varying fiber radius is given in Fig. 2.3(a), and the key feature for our purposes is that there always exists a guided mode – the *fundamental mode* HE_{11} – for all values of a, or equivalently V. One also observes in Fig. 2.3(b) the field intensity profile of the fundamental mode. The large in-fiber concentration of the electric field as well as the jump in intensity when heading out of the fiber are apparent. In the regime where only the single solution β_0 exists, the fiber is said to be single-mode, and any guided solution of Maxwell's equations must be proportional to $e^{i\beta_0 z}$, yielding the Green's function corresponding to Eq. (1.24) when radiation modes are disregarded. Relating to the Green function magnitude, the effective mode radius $r_{\text{eff}} = \sqrt{A_{\text{eff}}^{(2)}/\pi}$ (recall Eq. (1.6)) is given in Fig. 2.4 (a). One observes an optimal effective mode radius below the diffraction limit $\lambda/2$ for the fundamental HE_{11} mode, and from Fig. 2.4, one sees that a significant portion of the field is concentrated in the vicinity of the surface. In interfacing single emitters outside the fiber, it is important that neither the field concentration inside the fiber nor the effective mode area are too large. A good measure of concentration inside the fiber is the fractional power inside the waveguide, given for an eigenmode as [8]

$$\eta_p = \frac{P_{\text{in}}}{P}, \tag{2.13}$$

where $P_{(\text{in})}$ is the propagating power (inside the fiber) [8, 16]. The fractional power in the fiber can be seen in Fig. 2.4(b), where more and more of the power (and hence electric field) becomes spread out in the region outside the fiber, resulting in reduced coupling to a single emitter. These considerations usually lead to experimental ONF radii of 200 nm being used [22, 120, 134, 154, 157], where both r_{eff} is small and η_p is not too small.

2.4 Coupled optical fiber systems

2.4.1 Background

Introducing a second ONF into the system results in evanescent coupling between two optical elements and thus a relative phase between propagating rays of the two ONFs.

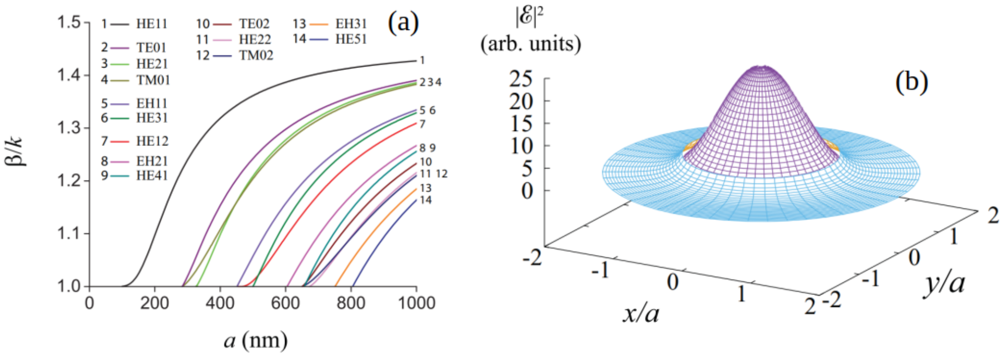

Figure 2.3: (a) Propagation constant normalized to the free-space wavenumber as a function of fiber radius a, for $\lambda = 780$ nm , $n_1 = 1.4537$. (b) Intensity profile of the (quasicircularly polarized) HE_{11} mode for $a = 400$ nm, λ and n_1 as in (a). Taken from [8], with figures relabelled.

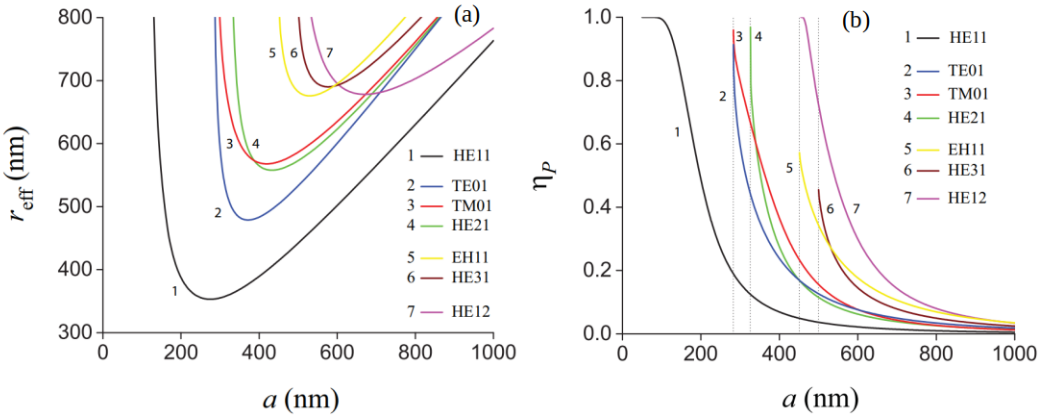

Figure 2.4: (a) The effective mode radius for the eigenmodes of the ONF for varying fiber radius. Constant parameters are the same as Fig. 2.3. (b) Fraction of modal power given (Eq. (2.13)) lying outside of the fiber, with constant parameters same as (a). Taken from [8], with figures relabelled.

These two principles guide the usage of coupled waveguide systems as optical elements and when interfacing with emitters, realising a wealth of applications including as couplers, sensors, interferometers and improved light-matter platforms. On the side of fundamental physics, arrays of many coupled waveguides allow for the simulation of solid-state physics in periodic media. With the rise of the ONF in the early 2000s, one of the first proposals featuring the two-fiber system was given in 2005 in [169], where the two fibers each play the role of an arm of a Mach-Zehnder inteferometer, and one fiber acts as sample probe. This setup was experimentally realised shortly after in 2008 [30], with the ONF providing a minimally-invasive, low-cost, and flexible platform for sensitive measurements. In addition the coupled ONF region can also directly play the measuring role when sensing temperature as in [31]. Recently, Fabry-Perot Resonators were even formed from a single looped ONF, where the region of coupling between the fiber and itself acts as a tunable beam splitter [32]. Of course, a finite-length coupling region can also simply serve to transport light from an undesirable channel to a more desirable one, with single photons efficiently collected by a plasmonic waveguide coupled to a nearby low-loss ONF for transportation [170]. With this single-emitter integrated system as just one example, multiple-waveguide style setups also naturally have a range of applications in the quantum optical domain.

Moving into the realm of quantum optics, the coupled-waveguide system has seen recent employment in particular due to the additional elements of field confinement and symmetry provided by the extra waveguide. For two waveguides close to one another the strong hybridization of the individual fiber modes can give rise to eigenmodes with effective wavevectors closer to that of vacuum than single fibers, i.e., much of the guided field lies in the vaccuum region between the two waveguides, and strengthens coupling to emitters using further confinement in the transverse plane (as opposed to group velocity engineering, see (1.24)). An early experimental realisation of an effective two-waveguide system was given in a 'slotted' waveguide [171], where new guided modes with effective index close to that of the external region were indeed observed. The effective coupled waveguide setup has additionally been proposed for trapping of cold atoms [35, 172] and realized for the trapping of nanoparticles [173], where the trapping schemes mentioned in Section 2.2.1 can produce greater intensities for trapping at identical powers due to the field localization in the slotted region. A high-profile and recent use of an effective two-waveguide system in cold-atom platforms is the 'alligator' photonic crystal waveguide, whose principles were conceptualized in [61] and which was consequently realised in [65]. Further benefits of atom trapping in the center of the two-waveguide geometry were highlighted in the theory here, such as restoring Casimir-Polder forces helping to deepen the trapping potential in a transverse direction, and the application of trapping in low-intensity minima [34, 174, 175] surrounded by regions of large intensity which further works to reduce scattering losses. As a final bonus, the low-intensity minimum of the mode used for trapping is compensated by a high intensity maximum for the aforementioned partnering super-mode, which is strongly coupled to atoms situated in the trap and can be used for effective probing. The powerful atomic trapping and interfacing platform offered by the two-waveguide geometry forms a strong foundation upon which the principles of photonic crystal waveguides have been applied, resulting in a plethora of novel experimental [37, 92] observations and proposals [28, 35, 53, 176] for exploring quantum light-matter platforms in the past decade (note that in current realisations in the 'alligator' crystal, the atoms are actually trapped slightly above the surface due to technical limitations. This has been addressed in [114], and trapping at the center of the structure should soon be possible). Finally, and most recently, a pure two-fiber system has also been explored in the context of coupling to emitters, where in-fiber coupling efficiencies up to 55% where found [33] at optical wavelengths, which can be compared with approximately 30% for the single fiber [62].

A final example of optical couplers goes beyond the two-waveguide setups introduced previously, featuring periodic 1D or 2D arrays, where photons emulating electrons travelling in the solid-state. 1D arrays of ONFs received the first treatment in 1965 [177] which was followed by a experimental realisation in Gallium arsenic in 1972 [178]. Here, diffraction characteristic of a *discrete* 1D system was observed. As the relationship between Maxwell's equations and Schrödinger's equation became more firmly rooted, coupled waveguide lattices found a place simulating quantum dynamical phenomena difficult to observe in traditional solid-state. A classical example is that of Bloch oscillations [179, 180] – whereas the small ratio of electron scattering time (due to defects) to oscillation period has precluded observation in natural crystals [181], arrays of coupled waveguides do not suffer from this shortcoming, and have allowed for direct observation [182] in space, where the spatial waveguide axis plays the role of time and refractive index modulations effect the potential. Furthermore, readily realisable complex variations of the refractive index has allowed for the extension of such simulations into the $\mathcal{PT}$-symmetric [183] domain [184]. With $\mathcal{PT}$-symmetric theory of coupled optical waveguides established only in 2007 [185], experimental observations in the past 5 years [186] have paved the way for exploration of non-Hermitian physics in higher dimensions, with very tangible applications in lasing [187] and topological matter [188]. Heading towards the quantum realm, classical analogues of the quantum zeno effect are further readily observable in arrays of optical waveguides [189], where again the conditions of observation are readily satisfied [181, 189, 190]. Recalling the quantized nature of the electromagnetic field, low photons numbers finally allow for the exploration of all the aforementioned effects and more in conjunction with the non-classical nature of light [191], [192], providing a foundation for investigating $\mathcal{PT}$-symmetric quantum mechanics as part of future quantum systems.

2.4.2 Coupled mode theory for two coupled fibers

The ubiquitous approximation used to describe the approximate eigenmodes of a system of evanescently coupled optical waveguides is *coupled mode theory* [16, 168] (CMT). This is, at its core, a perturbative method of describing the equations of motion for the full system mode amplitudes as an approximate linear combination of eigenmodes of the single waveguide systems, whereby the effective wavevectors of the joint system can be determined as eigenvalues of the (linear) equations of motion. Analysis of coupled waveguides was first carried out using CMT in 1954 [193, 194], where linear equations of motion for the single-waveguide modes amplitudes were determined in the full two-waveguide system by heuristic considerations. A more rigorous approach was taken in 1958 [195], where variational minimization was used to give the 'best' approximation to a system of two microwave tubes using only linear combinations of the single-tube systems. Applications to the specific case of ONFs was given in the 1970s [196, 197], whilst the treatment not assuming orthogonal modes [198, 199] gave the general coupled mode equations typically used in current works [184, 186, 190]. The coupled theory is well-suited to investigations where there is not a severe overlap of the evanescent mode of one waveguided with the (large) refractive index modulations caused by another [200, 201]. This means that the two ONFs may even be touching, provided the refractive index variations are not too large [202]. In this regime of 'weak coupling', linear combinations of the single fiber modes describe the two-fiber system well. Note, however, that these are rough qualitative criteria and no systematic conditions for validity of the CMT have been determined yet. Certainly, for optical wavelengths, moderate refractive indices $n_1 \sim 1.5$, and separations on the order of μm, the CMT reproduces the wavevectors of the two-ONF systems well [200, 203], and has been used to great effect in treating couplers [204, 205] and interferometers [32] employed in experiments [30, 131], in addition to usage in the wealth of investigations treating arrays of coupled waveguides[206, 207, 207, 208].

In brief, CMT condenses the interactions between single-waveguide modes down to three processes: (i) coupling between bare amplitudes of distinct modes (ii) self-coupling of modes of a single waveguide (i.e., distinct polarizations) due to scattering from the other waveguides (iii) coupling between longitudinal amplitude gradients of modes (*butt coupling*) [168]. In almost all of the literature – including in studies of coupled ONFs – the weak coupling conditions are deemed well satisfied and, further, only the amplitude coupling effect is taken into account. This is in contrast to the fact that as the weak-coupling conditions become closer to being violated, the latter two coupling effects may become significant, and cannot be neglected in general [16, 168]. In particular, advancements in optical fabrication have lead to routinely produced coupled-waveguide systems on the nanoscale and with short separation distances [30, 32, 131, 209], where it is not clear that the inclusion of only condition (i) is satisfactory; more accurate predictions including all the effects is necessary when operating in these regimes.

2.4.3 Summary and investigation outline

Returning to the early historical realisations, one of the simplest non-trivial case of two coupled waveguides is that of two lossless ONFs, which offers analytical tractability and simplicity whilst providing insight into the dynamics of more complex coupled-waveguide systems. Given the theoretical and experimental relevance of this system, it is crucial to provide accurate theoretical predictions corresponding to current state-of-the-art and near-future experimental setups. In this section, I therefore analyze the eigenmodes of the coupled-two-ONF system, using the approximate CMT and the exact eigenmode expansion. The eigenvalues are numerically calculated using both methods for experimentally realisable parameters, and I analyze the validity of the approximate theory in this regime. The approximate theory can be invalidated for experimentally relevant regimes where the CMT is typically used in the literature, and I further analyze the effective coupling between single-ONF eigenmodes in the full two-ONF system using the CMT. For particular parameters, the single-ONF modes may completely decouple from one another in the CMT. I finally analyze the electric field profiles of eigenmodes using the exact theory and observe that one mode has a large intensity in the region between the fibers – ideal for probing emitters – and one mode has a zero-intensity minimum in the region between the fibers – ideal for use in blue-detuned atomic traps. These results simultaneously provide theoretical predictions directly relevant to experimental ONF state-of-the-art, offer insight into general coupled-waveguide systems, and reaffirm the current usage of two-waveguide style systems in quantum optics.

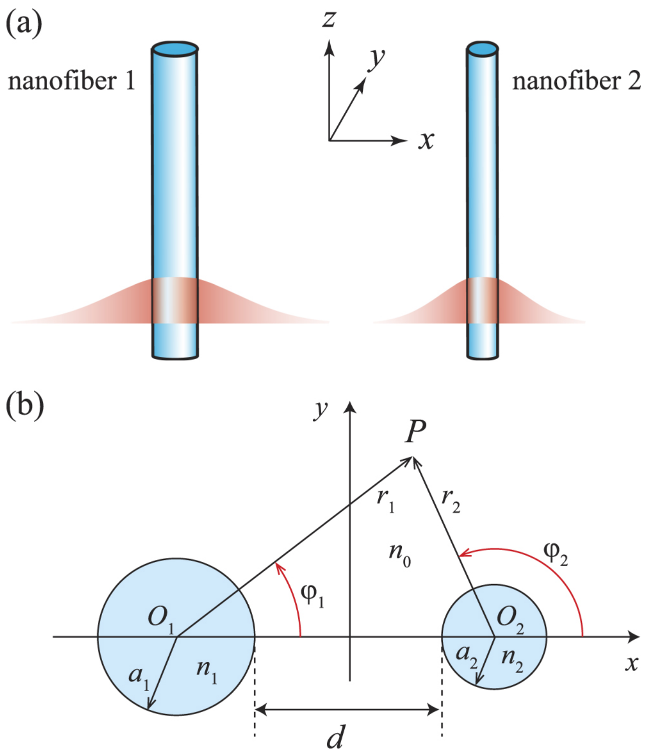

Figure 2.5: (a) The two ONF system. (b) Cross-section of the two-fiber geometry. Taken from [2]

2.4.4 Coupled Mode Theory: Mathematical Details

The goal is to obtain an approximate description of the eigensolutions of the two-ONF system shown in Fig. 2.5 in terms of the eigensolutions of the single-fiber systems. Take the fibers to have radius a and a minimal surface-to-surface separation of d. Due to the non-orthogonality of a pair of modes with one chosen as an eigenmode of each fiber, scattering from the opposite waveguide in general couples an eigenmode of one fiber to every other eigenmode of the other waveguide. However, in a waveguide with continuous translational symmetry, coupling between modes of different propagation constant is relatively weak due to the phase mismatch [16, 168, 170, 210], which means that one may select a single frequency-wavevector pair $(\omega, \beta(\omega))$, for frequency $\omega = ck$ and free-space wavenumber k and wavelength $\lambda = 2\pi/k$ respectively, and focus on the coupling between modes with these parameters. As the guided modes are typically the working photonic component, we focus on these modes, noting again that due to phase mismatch the coupling to radiation modes within the light line is in general weak. With the frequency-wavevector pair fixed, the polarization index p is the only free variable, and one assumes the total electric and magnetic fields of the two fiber system with free space wavevector k takes the form

$$\mathbf{E} = \textstyle\sum_{jp} A_j^{(p)} \mathbf{E}_j^{(p)}, \tag{2.14}$$

$$\mathbf{H} = \textstyle\sum_{jp} A_j^{(p)} \mathbf{H}_j^{(p)}. \tag{2.15}$$

Here, use j to refer to the each of the fibers 1 and 2. Substituting these fields into the variational expression for the eigenvalue ω^2 and minimizing functionally over amplitudes [16, 168, 199, 210] leads to the approximate coupled mode equations:

$$\sum_{j'p'} c_{jj'}^{(pp')} \frac{dA_{j'}^{(p')}}{dz} - i \sum_{j'p'} \nu_{jj'}^{(pp')} A_{j}^{(p')} = 0, \tag{2.16}$$

with

$$\begin{aligned} \nu_{jj'}^{(pp')} &= \frac{\omega\epsilon_0 \int d\mathbf{r}\ (n^2 - n_{j'}^2)(\boldsymbol{\mathcal{E}}_j^{(p)*} \cdot \boldsymbol{\mathcal{E}}_{j'}^{(p')})}{2\int d\mathbf{r}\ \mathrm{Re}[\boldsymbol{\mathcal{E}}_j^{(p)*} \times \boldsymbol{\mathcal{H}}_j^{(p)}]_z}, & (2.17)\\ c_{jj'}^{(pp')} &= \frac{\int d\mathbf{r}\ \{[\boldsymbol{\mathcal{E}}_j^{(p)*} \times \boldsymbol{\mathcal{H}}_{j'}^{(p')}]_z + [\boldsymbol{\mathcal{E}}_{j'}^{(p')} \times \boldsymbol{\mathcal{H}}_j^{(p)*}]_z\}}{2\int d\mathbf{r}\ \mathrm{Re}[\boldsymbol{\mathcal{E}}_j^{(p)*} \times \boldsymbol{\mathcal{H}}_j^{(p)}]_z}. & (2.18) \end{aligned}$$

In the above $n = n(\mathbf{r})$ is the refractive index variation due to both of the fibers, whilst $n_j = n_j(\mathbf{r})$ is that due to the fiber j. The elements $\nu_{jj'}^{(pp')}$ have inverse units of length, which upon normalization via $c_{jj'}^{(pp')}$ give a characteristic length scale over which a transfer of amplitudes occur. When the mode fields are normalized, one obtains for the dimensionless parameters [16]

$$c_{jj}^{(pp')} = \delta_{pp'}, \tag{2.19}$$

and a physical distinction between $\nu_{jj'}^{(pp')}$ for $j = j'$ and $j \neq j'$ can also be made – these quantities correspond to the self-wavenumber shift and butt coupling constants respectively [1, 168]. Assuming identical and lossless waveguides, we note the Hermiticity relation (for equal propagation constants)

$$\sigma_{jj'}^{(pp')*} = \sigma_{j'j}^{(p'p)}, \qquad \sigma = c, \nu. \tag{2.20}$$

Note that for far separated fibers, one can argue by inspection of the integrand in Eq. (2.18) that $v_{jj}^{(pp')} \sim e^{-dq} v_{jj'}^{(pp')}$ if $d \gg 1/q$ [168], and where $q = \sqrt{\beta^2 - k^2}$ is the inverse penetration length of the evanescent field, so that neglecting $\nu_{jj}^{(pp')}$ is justified. On the other hand Eq. (2.18) represents a power overlap [16, 168, 210], so that $c_{jj'}^{(pp')} \ll 1$ (i.e., reducing to an identity matrix) again for large fiber separations and $j \neq j'$. Applying the inverse of the c-matrix in Eq. (2.16) yields the standard linear equations of motion

$$\frac{dA_j^{(p')}}{dz} - i \sum_{j'p'} \xi_{jj'}^{(pp')} A_j^{(p')} = 0, \tag{2.21}$$

where under the assumptions of $c_{jj'}^{(pp')} \ll 1$ and $v_{jj}^{(pp')} \ll v_{jj'}^{(pp')}$ the ξ-matrix is approximately Hermitian, yielding the tight-binding equations of motion commonly employed in the literature [206, 207, 207, 208]. Note that almost all works considering evanescent waveguide coupling neglect the self-coupling and butt coupling. In general, for forward co-propagating modes $\beta_j = \beta_{j'} > 0$ the c-matrix should be positive definite [211], yielding a $\mathcal{PT}$-symmetric effective Hamiltonian (i.e., the ξ-matrix in Eq. (2.21)) when the inverse is applied. As a side note, typically in the literature the $\mathcal{PT}$-symmetry in waveguide arrays is obtained by introducing an imaginary component to the waveguide refractive indices [184, 185, 186, 188] as the c-matrix is chosen to be the identity. To my knowledge, there exists no investigations into the $\mathcal{PT}$-symmetric effects induced by the inclusion of the c-matrix elements. Returning to the present discussion, the symmetry of the particular two-fiber system dictates that the orthogonal quasi-linear polarizations along and perpendicular to the axis joining the two fibers do not couple to one another. We can then select the (quasi)linearly x- and y-polarized fiber modes [8] as the single fiber basis elements, and see that

$$\sigma_{jj'}^{(pp')} = 0, \tag{2.22}$$

for $p \neq p'$, so that (2.21) further reduces to

$$\frac{dA_j^{(p)}}{dz} - i \sum_j \xi_{jj'}^{(p)} A_j^{(p)} = 0, \tag{2.23}$$

for each p, where the double (pp) superscript has been abbreviated to (p). The linear equations then suggest coherent oscillations akin to Rabi oscillations between the two modes for each polarization. Assuming initial amplitudes $A_1^{(p)}(0), A_2^{(p)}(0)$, the amplitudes of the two fibers then evolve as

$$\begin{bmatrix} A_1^{(p)}(z) \\ A_2^{(p)}(z) \end{bmatrix} = e^{i\delta_p z} \begin{bmatrix} \cos(\eta_p z) & i\sin(\eta_p z) \\ i\sin(\eta_p z) & \cos(\eta_p z), \end{bmatrix} \begin{bmatrix} A_1^{(p)}(0) \\ A_2^{(p)}(0) \end{bmatrix}, \tag{2.24}$$

where the eigenvalues of the two-fiber system are given for each polarization and can be written as

$$\lambda_p = i(\delta_p \pm \eta_p), \tag{2.25}$$

$$\delta_p = \frac{\nu_{jj}^{(p)} - c_{jj'}^{(p)} \nu_{jj'}^{(p)}}{1 - c_{jj'}^{(p)2}}, \tag{2.26}$$

$$\eta_p = \frac{\nu_{jj'}^{(p)} - c_{jj'}^{(p)} \nu_{jj}^{(p)}}{1 - c_{jj'}^{(p)2}}, \tag{2.27}$$

which leads to $\lambda_p \sim \pm i\eta_p$ under assumptions of $c_{jj'}^{(p)} \ll 1$ and $v_{jj}^{(pp')} \ll v_{jj'}^{(pp')}$. On one hand the single-fiber propagation constant splits due to two-fiber coupling as $\beta \rightarrow \beta + \delta_p \pm n_p$, with corresponding two-ONF eigenmodes given as the (anti)-symmetric sum of the single fiber modes. On the other hand, the coefficients η_p and δ_p represent an inverse length over which power transfer and a global phase rotation occur respectively, so that the assumptions above lead to neglecting of the phase shift caused due to coupling. However, this is not in general a valid assumption; in the following, the coupling coefficients obtained using the CMT in a standard two-ONF system will be investigated, along with the deviations from the commonly employed results obtained by neglecting self-coupling and butt coupling.

2.4.5 Findings

Let us study typical ONF parameters realisable in current state-of-the-art silica ONF systems [30, 32, 131, 209]: a refractive index of $n_1 = 1.45$, optical wavelength $\lambda = 800$ nm, and fiber radii of 100nm and up, with arbitrary separation permissible. In Figs. 2.6 and 2.7, the dependence of the coupling coefficients in Eq. (2.16) are shown, with the prescription

$$\kappa_p = \nu_{jj'}^{(pp)}, \tag{2.28}$$

$$c_p = c_{jj'}^{(pp)}, \tag{2.29}$$

$$\chi_p = \nu_{jj}^{(pp)}. \tag{2.30}$$

The immediate observation from Fig. 2.6 (b) and (c) is that neither c_p nor χ_p are negligible for a range of d up to around $d \approx \lambda/2$; this then results in δ_p taking values comparable to η_p, at least for closer fiber separations $d \approx 100$ nm. Retaining the butt coupling c_p and self-energy coupling χ_p takes on further importance upon inspection of Fig. 2.6(a) and (2.27). In Fig. 2.6(a), κ_p takes strictly positive values, so that neglecting c_p, χ_p results in η_p taking positive values only also. However, inclusion of all terms allows competition between self-energy and coupling to drive the power transfer coefficient to zero, effectively decoupling the waveguides for judiciously chosen system parameters. This effect distinguishes coupling of vector electromagnetic waves from a scalar coupling between a TLS and field, for example, where the system is characterised by a single coupling strength generating oscillations at any non-zero value. Indeed, in Fig 2.7 one observes the power-transfer coefficient taking zero values for both the x- and y- polarizations. Note, however, that the zero-power transfer is obtained in the CMT, and exact analysis will generally need to be performed. As for the polarizations themselves, a noteworthy point is the distinct shift of propagation constant experienced by distinct polarizations. When an input beam that is a combination of both x- and y-polarizations is injected into a fiber, one will then observe a beating in the amplitude oscillatiaons due to competition between the two propagation constants. Denoting the power as

$$P_j^{(p)}(z) = |A_j^{(p)}(z)|^2 P_0, \tag{2.31}$$

the quasi-circular polarization can be obtained from the two quasi-linearly polarized fields as

$$\mathbf{E}^{\mathrm{circ}} = \frac{1}{\sqrt{2}}\big(\mathbf{E}^{(\mathbf{x})} \pm i\mathbf{E}^{(\mathbf{y})}\big), \tag{2.32}$$

so that one has the total power in a single ONF given by

$$P_j^{\mathrm{circ}}(z) = \big(|A_j^{(\mathbf{x})}(z)|^2 + |A_j^{(\mathbf{y})}(z)|^2\big)P_0, \tag{2.33}$$

which we simply shorten to P_j in Fig. 2.8. In Fig. 2.8(a) and (b), one observes the pure oscillation of amplitude between the two ONFs, although after two periods the difference in effective power-transfer already becomes apparent. This discrepancy then results in the beating observed in Fig. 2.8(c) for the quasicircularly polarized input

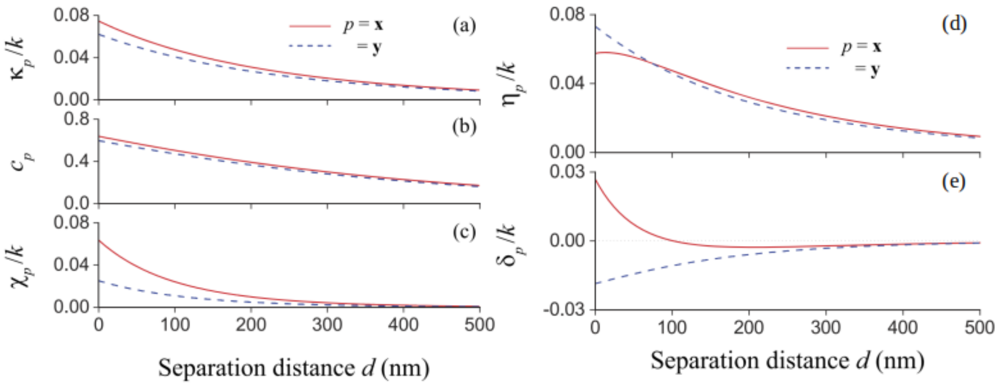

Figure 2.6: (a,b,c) The directional coupling coefficient, butt coupling coefficient, and self-coupling coefficient respectively, normalized to the free-space wavenumber k where applicable, for varying separation between two coupled ONFs. The wavelength of light is $\lambda = 800$ nm, with fiber radius $a = 200$ nm and core index $n_1 = 1.45$. The red solid (blue dashed) line gives coupling between x- (y-)polarizations. (d,e) The power-transfer coefficient and phase shift coefficient respectively, normalized to the free-space wavenumber, as a function of varying fiber radius. Parameters are the same as (a,b,c). Taken from [1]

field. It is worth noting that competition between the two modes results in an additional and highly-system-parameter-dependent length scale in the form of the beating length $\frac{2\pi}{\beta_1-\beta_2}$ [72]. In multi-mode single fibers, mode beating has been used to measure ONF radii to within angstroms [212] and for sensitive sensing within water [213]. In a similar manner the beating observed here could be used to characterise systems of coupled optical waveguides. As with the other results of this chapter, it is important to note that the results hold only in the approximation of the CMT, and in general an exact investigation is required.

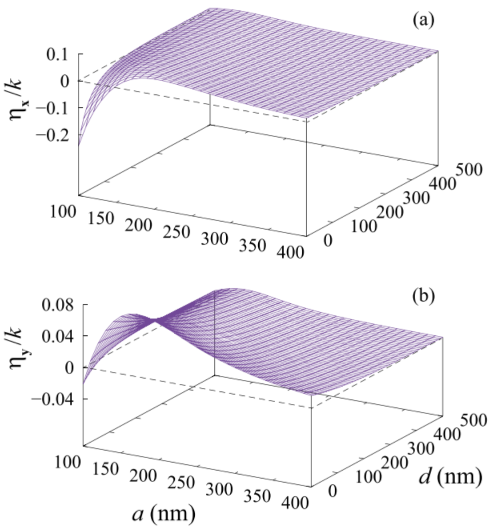

Figure 2.7: (a,b) Power transfer coefficient for the $x-$ and y- polarization respectively, normalized to free-space wavenumber, as a function of (identical) fiber radii and separation. All other parameters are the same as in Fig. 2.6(a,b,c). Taken from [1]

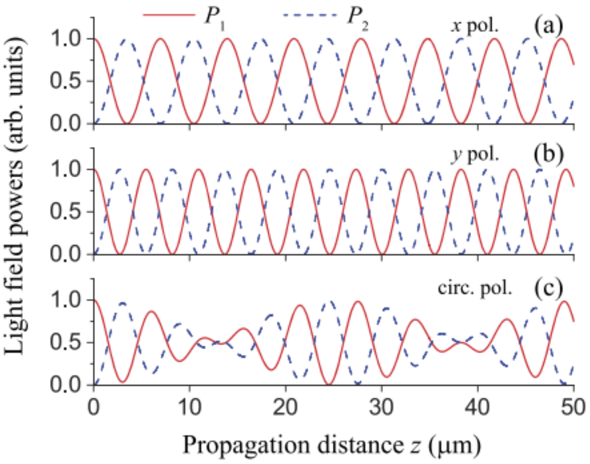

Figure 2.8: Power of the guided field in the two ONFs 1 and 2 respectively as a function of propagation distance z, in units of micrometers. in (a) and (b) the input field is x- and y- polarized respectively, whilst in (c) the input field in quasi-circularly polarized (see Eq. (2.32). Parameters are $a = 200$nm, $\lambda = 800$nm, $d = 0$, and $n_1 = 1.45$. Taken from [1]

2.4.6 Publication [1]: Coupling between guided modes of two parallel nanofibers

The results of this chapter are published in [1] as

Coupling between guided modes of two parallel nanofibers
F Le Kien, L Ruks, SN Chormaic, T Busch
New Journal of Physics **22** (12), 123007 (2020)

Dr Le Kien conceived of and initiated the project. I carried out all numerical simulations, and performed the analytical derivation of the differential equation solutions. All authors contributed to the interpretation of results and writing of the later versions of the manuscript.

2.5 Exact analysis of the two-fiber system

Whilst the approximate CMT has been employed to great success over many decades, experimental advances have miniaturized optical components down to the nanoscale, comparable to optical wavelengths and where the full coupled-mode theory can be invalidated due to strong hybridization of modes [202]; the effect can be a dramatic modification of the propagation constants [201] of the two-fiber system in addition to the eigenmode polarization profiles [203]. Notably, the CMT may even suggest the existence of eigenmodes beyond the cutoff of the full two-fiber system [201], whilst polarizations of the exact system are suggested to deviate strongly from a simple (anti)symmetric linear sum [203]. Amongst other scenarios, experimentally realised 'slot'-style waveguides [35, 37, 172, 173] and ONF couplers [30, 31, 32] frequently enter such regimes; despite the interest surrounding the two-ONF (and more generally, two waveguide) setup, there is not to my knowledge a comprehensive investigation treating the exact features of the electric field profiles in this fundamental setup. Such knowledge would both be directly applicable to existing multiple-ONF platforms and could provide insight that can carry over into other coupled-waveguide style setups. In this investigation, the analytical calculations behind the eigenmode expansion of a system of two coupled ONFs are detailed, and numerical calculations of the electric field profiles are explored. In addition, the discrepancy with the coupled mode approximation in the notable regime where the ONF radii, the wavelength of light, and the distance between the two fibers are all of the same order of magnitude are discussed.

2.5.1 Expansion into eigenmodes

I again consider the two-fiber system as shown in Fig. 2.5, but now seek the exact eigensolutions to Maxwell's equations. Before proceeding with the fine details, one can immediately draw up some expectations for the two-fiber system in the most relevant case of equal fibers. Although cylindrical symmetry of the system is destroyed, reflection about the x- and y-axes leave the fiber-system invariant. One then expects to be able to specify four polarization corresponding to combinations of the modes with even/odd symmetry about the x/y-axis. Indeed, we will see that these symmetries manifest as $\mathcal{E}_z \to \pm\mathcal{E}_z$ upon reflection about the x or y-axis. With these expectations in mind, and bearing in mind also the cylindrical symmetry of the single-fiber system, one proposes the expansion of the electric field *of guided modes* in terms of cylindrical harmonics of *both* fibers [202, 214] (recall from Eq. (2.7) that the transverse components can be obtained from the longitudinal components), where inside fiber j the field takes the form

$$\begin{aligned}
\mathcal{E}_z &= \sum_{n=0}^{\infty}[A_{nj}J_n(h_jr_j)\cos n\varphi_j + E_{nj}J_n(h_jr_j)\sin n\varphi_j], \\
\mathcal{H}_z &= \sum_{n=0}^{\infty}[B_{nj}J_n(h_jr_j)\sin n\varphi_j + F_{nj}J_n(h_jr_j)\cos n\varphi_j],
\end{aligned} \tag{2.34}$$

and outside the two fibers takes the form

$$\begin{aligned}\mathcal{E}_z &= \sum_{j=1}^{2}\sum_{n=0}^{\infty}[C_{nj}K_n(qr_j)\cos n\varphi_j + G_{nj}K_n(qr_j)\sin n\varphi_j],\\ \mathcal{H}_z &= \sum_{j=1}^{2}\sum_{n=0}^{\infty}[D_{nj}K_n(qr_j)\sin n\varphi_j + H_{nj}K_n(qr_j)\cos n\varphi_j]. \qquad (2.35)\end{aligned}$$

Here, we have introduced the fiber parameters

$$h_j = \sqrt{k^2n_j^2 - \beta^2}, \qquad q = \sqrt{\beta^2 - k^2}. \qquad (2.36)$$

We can first use the system symmetry to specify four types of polarizations in the two fiber system. One specifies the so-called even/odd modes via the prescription

$$X_{nj} = (-1)^n \nu X_{nj'}, \qquad X = A, B, C, D, E, F, G, H, \qquad (2.37)$$

where ν specifies whether the mode is even/odd, i.e., whether the $\mathcal{E}_z$ is unchanged/flips sign upon inversion $(x, y) \to (-x, -y)$ in the transverse plane. Note the convention that the odd mode corresponds to $\nu = 1$ (no sign flip) and the even mode to $\nu = 0$ (sign flip). Furthermore, Graf and Gegenbauer's addition theorem [215] shows that cosine and sine terms are not coupled to one another through the scattering process, so one may specify *$\mathcal{E}$-sine* modes (corresponding to x-quasilinear polarization, or TE-modes in [114]) with all $A_{nj}, B_{nj}, C_{nj}, D_{nj} = 0$, or *$\mathcal{E}$-cosine* modes (corresponding to y-quasilinear polarization, or TM modes in [114]) with all $E_{nj}, F_{nj}, G_{nj}, H_{nj} = 0$. Connecting to the CMT, the $2 \times 2 = 4$ specifications corresponding to combinations of the odd/even and sine/cosine specification approximately correspond to choosing the (anti)symmetric combinations of the $x-$ and y- (quasilinear-)polarizations for the single fibers. With the polarization specified, one obtains the eigenvalue equation for guided modes by applying Graf and Gegenbauer's addition theorem [215] to expand circular harmonics of one fiber in terms of the circular harmonics of the other, matching the angular orders via boundary conditions at each of the fiber interfaces. This yields eight equations for each mode order n. As our system is described by eight free parameters for each n, one again obtains a consistency condition to determine the effective wavevector β. As the other fiber couples all azimuthal numbers of one waveguide, the resulting system of equations is infinite, but for a fixed solution the coefficients drop off exponentially for $n \to \infty$, and a cutoff order of $N_{\max} < 19$ (in these calculations) is determined [202] such that the solution for β converges.

2.5.2 Findings

In the following the salient results obtained in the relevant case of two identical fibers are presented, with additional numerical simulations demonstrating the full field behaviour for non-equal fibers [2]. In Fig. 2.9, the propagation constants of the two-identical-ONF system are plotted for each of the four modes (we operate in the regime where no more than four modes of the two-ONF system exist) with varying fiber radii

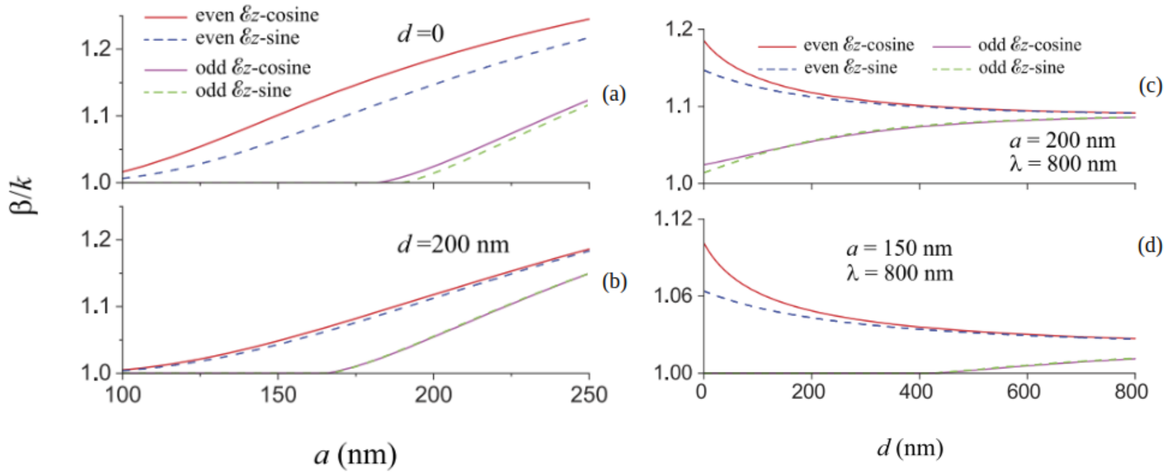

Figure 2.9: Propagation constants normalized to the free space wavenumber $k = 2\pi/\lambda$, for $\lambda = 800$ nm and $n_1 = 1.4533$ as (a,b) the (equal) fiber radii are varied with fiber separation d fixed (c,d) d is varied with the fiber radii remaining fixed. Taken from [2].

and distance. A stark difference between the predictions of the coupled-mode theory and the exact results can be seen in the cutoff $\beta = k$ for the odd modes when the fiber radii (Fig. 2.9(a,b)) or the two-fiber distance (Fig. 2.9(d)) are reduced. For any distance of separation, it can be expected that there is always a cutoff for the odd modes with reduction of radii (as observed in Fig. 2.9(a,b)), as the evanescent leakage from the core dominates and eigenmodes approach the (two) even polarizations of free space. For variation of d, the picture is somewhat more complex, as a cutoff occurs in Fig. 2.9(c) for fiber radii of $a = 200$nm, but not in Fig. 2.9(d), for fiber radii of $a = 150$nm. This could be attributed to the fact that for small enough radii and small enough separation, light at the given wavelength becomes unable to resolve the two separate structures, yielding the two polarizations expected of an (approximate) single-mode ONF. To compare with our previous results of the CMT, in Fig. 2.10 the difference

$$\eta_p = (\beta_{\nu}^{(p)} - \beta_{\nu'}^{(p)})/2, \tag{2.38}$$

between the odd ($\nu = 1$) and even ($\nu' = 1$) modes is plotted for the $p = x$ ($\boldsymbol{\mathcal{E}}_z$-cosine) and $p = y$ ($\boldsymbol{\mathcal{E}}_z$-cosine) polarizations respectively, alongside the predictions from the CMT. Excepting cutoffs, the CMT predicts η_p well, except for fibers with small radii that are (nearly) touching with $d \lessapprox 100$nm (Fig. 2.10(a,c)); for refractive index of $n_1 \approx 1.45$ corresponding to silica, one cannot then expect to obtain accurate results using CMT when the ONF separation is on the order of $d \lessapprox 100$nm, or when the ONF radius becomes too small, i.e. $a = 150$nm. However, if the mode cutoffs are taken into account, then for the remaining modes the CMT gives reasonably accurate results for the propagation constants.

A further crucial distinction between the exact theory and CMT can be seen upon inspection of the electric field profiles, particularly at the two-ONF center, $(x, y) =$

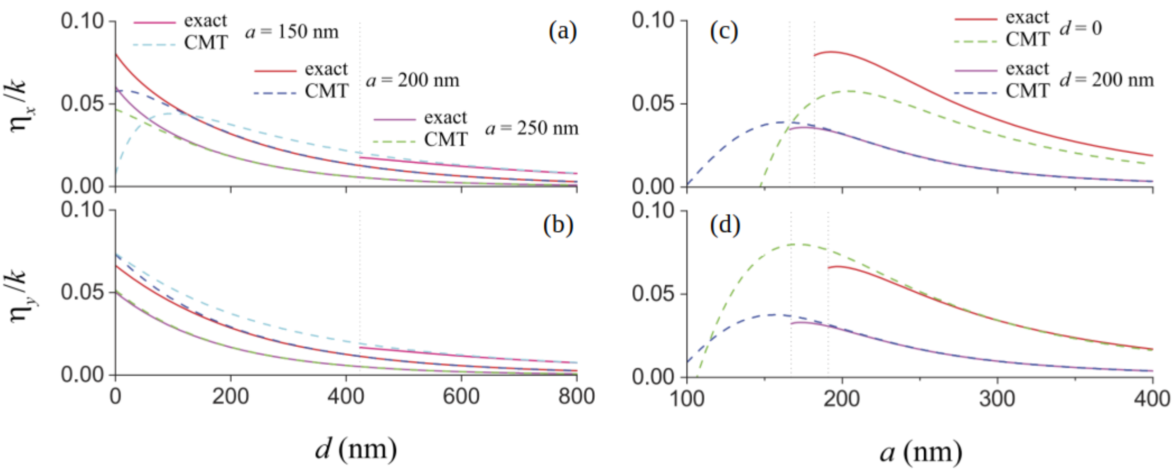

Figure 2.10: Power transfer coefficients (2.27) as the (a,b) fiber separation is varied (c,d) fiber radii are varied for the (a,c) $x-$polarized (b,d) y-polarized mode. Parameters are $\lambda = 800$ nm and $n_1 = 1.4533$. Taken from [2].

$(0, 0)$. Notably, every polarization component of the odd-$\mathcal{E}_z$-sine mode is odd under reflection about either the $x-$ or y-axis. This means that $\mathcal{E}(\mathbf{0}) = \mathbf{0}$, producing a *zero-intensity* minimum at the center of the two fibers, which can be observed in Fig. 2.11 (a,b,e). One can check that the CMT does not predict a zero-intensity minimum, which is hence a result of strong mode hybridization, and can apparently not be predicted by inspection of Maxwell's equations. The absence of any intensity is particularly relevant as an atom with polarizability $\alpha(\omega)$ experiences an average scattering rate

$$\langle \Gamma_{\rm sc} \rangle = \frac{\Im[\alpha(\omega)]}{4\hbar} \langle |\boldsymbol{\mathcal{E}}|^2 \rangle, \tag{2.39}$$

where the brackets denote expectation over atomic wavefunction. Assuming a Gaussian (in 1D, for simplicity) form of the atomic wavefunction with extent $a_r \ll \lambda$ and centered at $\mathbf{0}$, a non-zero intensity $\mathcal{E}(\mathbf{0}) \neq \mathbf{0}$ binds the scattering rate from below by $\langle \Gamma_{\rm sc} \rangle \sim \frac{\Im[\alpha(\omega)]|\mathcal{E}|^2}{4\hbar}$ [34], whilst for a zero intensity, the scattering then becomes gradient-limited, depending on the atomic spread $\langle \Gamma_{\rm sc} \rangle \sim \frac{\Im[\alpha(\omega)](|\boldsymbol{\mathcal{E}}|^2)'' a_r^2}{4\hbar}$, where the prime denotes the derivative in the spatial variable. This principle should play a significant role in a blue-detuned atomic trapping scheme, where scattering in the (zero)-intensity minimum would be greatly reduced, for the predicted heating rate *due to spontaneous emission* is given as

$$\frac{dE_{\rm sc}}{dt} = E_r \langle \Gamma_{\rm sc} \rangle, \tag{2.40}$$

for atom mechanical energy E and recoil energy $E_r = \frac{h^2 k^2}{2m}$. I note that both a fully quantum [216] and semiclassical [217] treatment revealed a heating term proportional to the gradient of the electric field, which is in principal on the same order of the scattering rate Eq. (2.39) and which is due to fluctuations in *absorption*. This result adds a correction to (2.40), and suggests even at zero intensities that intensity curvature

fundamentally bounds heating from below at lower temperatures. As atoms may now be cooled close to the limit of single motional quanta [158], it is desirable to reexamine the heating rates in the quantum regime for atoms trapped next to ONFs, and determine fundamental heating limits set by (two-color) beginning from first principles.
Whilst a complete theoretical characterisation of heating in evanescent traps is incomplete, blue-detuned traps nonetheless offer advantages of reduced scattering and undesirable level shifts for atoms traps in potential minima. Experiments applying zero-intensity blue-detuned traps have yielding promising results, with the zero-intensity minimum realising the core component of a bottle beam trap [218, 219] and being used in conjunction with the pondermotive force to create state-independent traps for Rydberg atoms [220]. However, I am not aware of any scheme employing zero-intensity minima in trapping of individual atoms via evanescent fields of coupled waveguide systems. The recent realisation of Rydberg states in the vicinity of ONFs [221] raises the possibility of coherent Rydberg trapping using a blue-detuned $\mathcal{E}_z$-sine mode. On the other hand, the even $\mathcal{E}_z$-cosine mode sees high intensity (see Fig. 2.11(c,d,f)) in the region between the two fibers, and is thus well suited to probing and interfacing nearby cold atoms. The particularly strong coupling to $\mathcal{E}_z$-cosine style modes has been noted in other two-waveguide style platforms [35, 61].

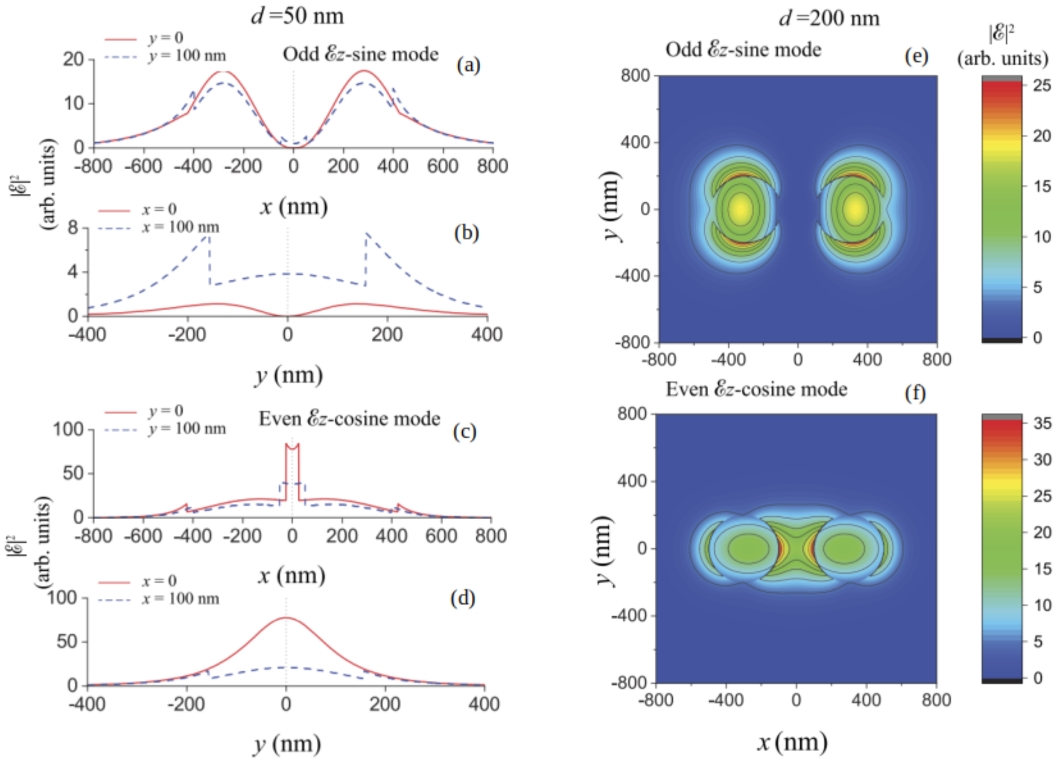

Figure 2.11: Electric field intensity profiles (a,b,c,d) along a slice in the transverse plane (e,f) in the full transverse plane for (a,b,c) the odd $\mathcal{E}_z$-sine mode (c,d,f) the even $\mathcal{E}_z$-cosine mode. The fiber radii are $a_1 = a_2 = 200$nm, and the refractive indices are $n_1 = n_2 = 1.4533$.

2.5.3 Publication [2]: Spatial distributions of the fields in guided normal modes of two coupled parallel ONFs

The results of this chapter are published in

Spatial distributions of the fields in guided normal modes of two coupled parallel optical nanofibers
F Le Kien, L Ruks, SN Chormaic, T Busch
New Journal of Physics **23** (4), 043006 (2021)

Dr Le Kien conceived of and initiated the project. I carried out all numerical simulations, and contributed to the analytical considerations of solutions. All authors contributed to the interpretation of results and writing of the later versions of the manuscript.

2.5.4 Experimental considerations

The presented results are directly applicable to current experimental setups realising coupled silica-ONF systems at optical wavelengths with separations on the order of 100s of nm or less [30, 32, 131, 209], where the weak-coupling assumption begins to break down. As a cold-atom platform, slot waveguides realising the effective 'two-waveguide' setup have recently seen coupling to thermal atomic gases [36], but to my knowledge maneuvering of individual cold atoms into the trapping sites at the center has not yet been experimentally realised. The recent proposal for atomic positioning within the 'alligator' photonic crystal using optical conveyor belts [114] suggests that in principle cold atoms can be positioned in the center of two waveguides with a spacing of $d = 250$ nm between the surfaces, so that a similar scheme could be realised in slotted [173] waveguides, and two-ONF systems. Whilst trapping is sensitive to as little as 10% size differences between the two waveguides [2, 34], ONFs can typically be fabricated with a small variations of $\pm 5\%$ in radius [212] even for ultra-thin 100nm fibers [222], which should then not pose a problem.

2.5.5 Outlook and conclusions

Since publishing, the works [1, 2] comprising this chapter have led to subsequent investigations in a variety of scenarios. Inclusion of the butt- and self-coupling coefficients allowed us to provide a more complete picture of the two-ONF interferometer/resonator scenario considered in [32], which has been taken into consideration by the authors. In a follow-up work by my collaborator Dr Le Kien, the odd $\mathcal{E}_z$-sine mode was exploited to create a long-lived atomic trap centered between the two waveguides [34], and reported greatly increased trapping and coherence times for Cesium atoms trapped with light blue-detuned from the D_1 ($\lambda = 894$ nm) and D_2 ($\lambda = 780$ nm) lines. Specifically, trap depths on the order of mK should be possible, similar to the current two-color trap standard [22, 115], but the predicted coherence-limited and recoil-limited trap lifetimes of 5.8 s and 4.8 hr respectively are orders of magnitude larger than those of the two color trap. Similarly attractive figures of merit could also be expected to be achieved in analogous two-waveguide geometries [61, 173]. Furthermore, even without exploiting the group velocity effect of PCWs [61], coupling of emission to the guided mode of a two-ONF system can reach 30% [33] for a separation $d = 150$ nm and radii $a = 135$ nm, which can be compared for couplings of 10% in the single-fiber setup [22]. In both cases the atom-fiber separation is 75nm. The combination of simultaneous efficient trapping and coupling means it would thus be beneficial to further explore [114] the experimental possibly of exploiting the two-waveguide geometry as a light-matter platform. Furthermore, the results of this work have lead to the forces ('optical bonding') between two ONFs being investigated [223], with possible applications to optically tunable mechanical structures. Finally, my colleague Dr Kritika Jain is following up on this work with a construction of the full Green's function for the full two-fiber system in order to investigate the effective emitter-emitter interactions induced through photons of the two-fiber system.

2.6 Ground State Dispersion Potential for two Emitters in the Presence of a Dielectric Cylinder

2.6.1 Background

The dispersion potential between neutral yet polarizable quantum emitters at zero temperature is a notable example of a pure quantum phenomenon in electrodynamics that demands fluctuations of the emitters and/or the EM field in their ground state. The dispersion interaction is long range, (i.e., decays as a power law) and is strong enough to dictate emergent dynamics in systems of varying scales. Notable examples in nature can be found in the dynamics of cell membranes [224] on the microscopic level and in the organism-surface adhesion mechanisms on the organism level [225], and even in contribution to the initial formation of orbiting bodies on the planetary scale [226]. Aside from these interests, dispersion interactions also play a prominent role in experimental quantum optical setups. One the one hand, the development of clean experimental light-matter systems has given us unprecedented control over single emitters/media and their environment, so that the dispersion potential may be used to study fundamental physics, including models of physics on small length scales [227], and play a key role in microscopy [228] and atomic manipulation [83] (one may see the review [38] for further applications). However, in the very same setups these dispersion forces can also have detrimental effects, chiefly in the form of the resulting attraction typically dominating at short range and causing atoms to stick to surfaces (adsorption) [114, 229, 230, 231] – this is especially a problem in interfacing Rydberg atoms with huge dipole moments with nanophotonic structures [221, 231, 232].

Whilst the celebrated results concerning the case of e.g., two identical emitters in a vacuum [233] and other basic geometries [234] have been around for many decades, more realistic predictions in nature and in advancing experimental setups require the study of dispersion interactions of emitters in the presence of general macroscopic media. In another success for the Green's function in QED, the dispersion interaction between two emitters in the presence of arbitrary linear dielectric media was derived in 2006 [235], which has amongst others, recently enabled the discovery of enhanced-magnitude Casimir-Polder interactions and enhanced chiral vdW forces for emitters in the vicinity of 2D materials [55], and 2D chiral media respectively [236]. On the other hand, optical waveguides offer a simplified quasi-1D geometry and experimentally realisable platform to probe natural manifestations of the dispersion interaction in a structured environment very much distinct from a 3D or 2D bulk. Here, significant deviations from the vacuum theory were found, with interactions reduced to short range exponential decay when placed on the axis of a perfectly reflecting hollow cylinder on one hand [39], and more recently, enhanced interaction magnitude and power law decay ($1/R^3$,compared with $1/R^6$) in transmission lines [41] found on the other. These effect can both enable more efficient probing of dispersion effects, and could be used in conjunction with other phenomena exploiting dispersion, i.e., the Rydberg blockade mechanism.

For spherically symmetric emitters, the polarizability – generally a tensor – reduces to a scalar, so that any anisotropy in the resulting emitter-emitter dispersion potential enters through the electromagnetic environment (the Green's function). For ground-state atoms, this isotropy assumption is typically made [41, 77, 235, 237]. However, this assumption is violated in, for example, molecules, and the dispersion potential between a single anisotropic particle and a surface has been explored in [42, 43, 238, 239, 240, 241], where a key feature is that anisotropy can result in *repulsive* forces as opposed to the typically attractive ground-state dispersion forces, whilst for particular orientations of the dipole transition matrix element particular power-law contributions can be eliminated. Moving to the case of body-assisted emitter-emitter dispersion interactions, recent investigations treated the case of identical emitters with preferred dipole orientations [39, 40] in a cylindrical geometry, whilst the case of distinct dipole matrix transition elements has been studied in the vacuum [42, 43, 44]. As with the surface-emitter interaction, the dispersion interaction can be enhanced or diminished (including elimination of particular power-law terms) by choosing specific dipole matrix transition elements, and the results shed light on the emitter anisotropy as an extra degree of freedom in engineering dispersion interactions.

2.6.2 Investigation outline

Despite the interest surrounding the dispersion interaction in polarizable media, to the best of my current knowledge there exist no studies investigating the integration of two emitters whose dipole transition matrix elements are misaligned, that is, $\mathbf{d}_j \neq \mathbf{d}_k$ in Eqs. (2.43), and in a 1D geometry. As experimental advances continue on the nanoscale, investigations into dispersion interactions featuring anisotropic emitters and environment could reveal new mechanisms for probing the fundamentals of QED and for manipulating matter on the nanoscale. In this chapter, I introduce the theory of and discuss the ground-state dispersion interaction between two emitters in the presence of one-dimensional cylindrical media. In particular, for atoms in a vacuum the Green's tensor does not couple two dipoles whose matrix elements are orthogonal and lie in the plane perpendicular to the line joining them, but the media-induced anisotropy then re-couples these elements, producing a dispersion interaction for this pair of dipole elements that is in a sense infinitely enhanced beyond the vacuum.
With this analytical observation as starting point, I numerically calculate the Green's function of dispersive and absorbing cylindrical media and determine the dispersion interaction between the two atoms as the distance along the waveguide axis is varied. I find that the interaction dispersion of two atoms with orthogonal dipole transition matrix elements may be considerably enhanced at longer ranges or diminished at shorter ranges compared to the dipole-averaged dispersion potential experienced by atoms in free space. In comparison to vacuum induced dispersion, the cylinder-mediated potential sees a minimum, which in principle permits ground-state optical binding along the cylinder axis. Considering the case of different dispersive (and lossy) media, I find the enhancement is greater for gold and silicon, in contrast to silica. The results are directly relevant for experimental cold-atom-ONF platforms, whilst offering more fundamental insights to dispersion effects induced purely by media scattering.

2.6.3 Theory

As expanded on in Chapter 1, a (single-body) energy shift is found at second order in the emitter-field coupling. Although derived as part of the (dynamical) master equation (1.52), the appearance of this self coupling term is made clearer considering stationary second-order perturbation theory for the full light-matter coupling Hamiltonian $\hat{H}_{\text{int}}$ (see (1.41)) [235]

$$\Delta E = -\sum_{I} \frac{\langle 0|\hat{H}_{\text{int}}|I\rangle\langle I|\hat{H}_{\text{int}}|0\rangle}{E_I - E_0}, \tag{2.41}$$

where the sum is made over intermediate states I distinct from the ground state and $|0\rangle$ denotes the vacuum. Note that the parity of the photon/atom creation/annihilation terms means that perturbative contributions at odd orders will be zero; retaining the counter-rotating terms in the Hamiltonian allows pair-creation terms such as $\hat{\mathbf{f}}^{+}(\mathbf{r},\omega)\hat{\sigma}_j^{+}$ to couple the vacuum to an intermediate state I containing one photon and one emitter excitation. I must then be coupled again to the vacuum via the corresponding pair-annihilation $\hat{\mathbf{f}}^{+}(\mathbf{r},\omega)\hat{\sigma}^{j}$, yielding only single-emitter energy shifts contributing to the full system. At fourth order in atom-field coupling, one obtains [235]

$$\Delta E = -\sum_{\text{I,II,III}} \frac{\langle 0|\hat{H}_{\text{int}}|\text{I}\rangle\langle \text{I}|\hat{H}_{\text{int}}|\text{II}\rangle\langle \text{II}|\hat{H}_{\text{int}}|\text{III}\rangle\langle \text{III}|\hat{H}_{\text{int}}|0\rangle}{(E_{\text{I}} - E_0)(E_{\text{II}} - E_0)(E_{\text{III}} - E_0)}. \tag{2.42}$$

Here, the intermediate states I and III are again pair-excitations of a single photon and single emitter, but these states need not correspond to the same emitter, as they can be coupled through II as a state containing (i) two photonic excitations (ii) two emitter excitations or (iii) two emitter and two photonic excitations. Isolating all contributions from intermediate states containing excitations of emitters j, k yields the two-body ground-state potential in terms of the system Green's function $\mathbf{G}$ and atomic polarizability tensor $\boldsymbol{\alpha}$ (recall (1.48)) [235]

$$\begin{aligned} U_{jk}(\mathbf{r}_j, \mathbf{r}_k, \omega_0) &= -\frac{2\mu_0^2}{\hbar\pi}\int_0^\infty \frac{du u^4 \omega_0^2}{(\omega_0^2 + u^2)^2}\left[\mathbf{d}_j \cdot \mathbf{G}(\mathbf{r}_j, \mathbf{r}_k, iu) \cdot \mathbf{d}_k^*\right]^2, \\ &= -\frac{\hbar\mu_0^2}{2\pi}\int_0^\infty du u^4 \text{Tr}\left[\boldsymbol{\alpha}_j(iu) \cdot \mathbf{G}(\mathbf{r}_j, \mathbf{r}_k, iu) \cdot \boldsymbol{\alpha}_k(iu) \cdot \mathbf{G}(\mathbf{r}_k, \mathbf{r}_j, iu)\right] \end{aligned} \tag{2.43}$$

for atomic dipole transition matrix elements $\mathbf{d}_j, \mathbf{d}_k$, positions $\mathbf{r}_j, \mathbf{r}_k$, and where identical transition frequencies ω_0 for two-level atoms are assumed. Tr denotes the trace.

Dependence on relative permitivity

In a dielectric and homogeneous isotropic medium (with the vacuum as a special case of a bulk medium), the Green's function is simply determined by the (scalar) relative permitivity $\epsilon(\omega)$. As an example, the permitivities corresponding to silica (SiO2), silicon (Si), and gold (Au) can be well modelled by the Sellmeier equation [242], the Drude [39], and the Drude-Lorenz [39] models respectively, which can all be captured in the standard Lorentzian dielectric response function

$$\epsilon(\omega) = \epsilon_\infty + \sum_j \frac{\omega_{pj}^2}{\omega_j^2 - \omega^2 - i\Gamma_j\omega}. \tag{2.44}$$

For gold and silicon, one considers only the single resonance, with $\epsilon_\infty = 1$, $\omega_p = 2\pi \times 2.07$ PHz, $\Gamma = 10^{-3} \times \omega_p$, $\omega_0 = 0$ Hz and $\epsilon_\infty = 1.035$, $\omega_p = 2\pi \times 21.7$ PHz, $\Gamma = 0$ Hz, $\omega_0 = 2\pi \times 6.6$ PHz respectively. The formula for silica, with multiple resonances, is given in [115]. Note that at imaginary frequencies $\epsilon(\omega)$ is (necessarily) real, and $\epsilon(\omega) \to 1$ as $\omega \to \infty$ due to causality [77] (whilst both choices $\epsilon_\infty \neq 1$ and $\Gamma = 0$ in Eq. (2.44) violate causality, the difference is acceptably small within optical wavelengths of interest, with the dielectric function for silica having seen application in [39]).

Example in a bulk medium

With this machinery in place, one may begin by considering the simplest bulk medium $\epsilon(\mathbf{r}, \omega) = \epsilon(\omega)$. For example, one obtains from Eq. (1.21) the standard results in free space for the retarded and non-retarded dispersion potentials as

$$U_{jk}^{\text{non-retarded}}(\mathbf{r}_j, \mathbf{r}_k, \omega_0) = -\tfrac{C_6}{R^6}, \tag{2.45}$$

$$U_{jk}^{\text{retarded}}(\mathbf{r}_j, \mathbf{r}_k, \omega_0) = -\tfrac{C_7}{R^7}, \tag{2.46}$$

for the vdW coefficients

$$C_6 = \frac{1}{32\pi^2\hbar\epsilon_0^2\omega_0}|\mathbf{d}_j \cdot \mathbf{d}_j^* - 3(\mathbf{d}_j \cdot \hat{\mathbf{R}})(\mathbf{d}_k^* \cdot \hat{\mathbf{R}})|^2, \tag{2.47}$$

$$C_7 = \frac{c}{32\pi^3\hbar\epsilon_0^2\omega_0^2}\big\{13|\mathbf{d}_j \cdot \mathbf{d}_k^*|^2 + 63|\mathbf{d}_j \cdot \hat{\mathbf{R}}|^2|\mathbf{d}_k^* \cdot \hat{\mathbf{R}}|^2 - 56\Re[(\mathbf{d}_j^* \cdot \mathbf{d}_k)(\mathbf{d}_j \cdot \hat{\mathbf{R}})(\mathbf{d}_k^* \cdot \hat{\mathbf{R}})]\big\}, \tag{2.48}$$

where the unit separation vector is given as $\hat{\mathbf{R}} = \frac{\mathbf{r}_j - \mathbf{r}_k}{|\mathbf{r}_j - \mathbf{r}_k|}$. In the absence of anisotropy in the state and transitions, one may average over dipole orientations to obtain a mean dispersion which, for the retarded potential, results in the dispersion coefficient of a homogeneous bulk medium

$$C_7 = \frac{23\hbar c}{64\pi^3\epsilon_0^2}\frac{\alpha_j(0)\alpha_k(0)}{n(0)\epsilon^2(0)}, \tag{2.49}$$

for $n(iu) = \sqrt{\epsilon(iu)}$, as only the long wavelengths ($u \to 0$) contribute significantly. The scalar polarizability is obtained by averaging as $\alpha_j(\omega) = \frac{1}{3}\mathrm{Tr}[\boldsymbol{\alpha}_j(\omega)]$. Note also that it is ideal to include the full dispersion of the material when calculating the dispersive interaction in order to prevent possible violations of no-go theorems [243] and as the frequency response across all (imaginary) frequencies is used in the calculation (2.43): in the non-retarded limit and after averaging over transition orientations one finds for i.e., bulk materials that the C_6 coefficient is in principle determined by the material

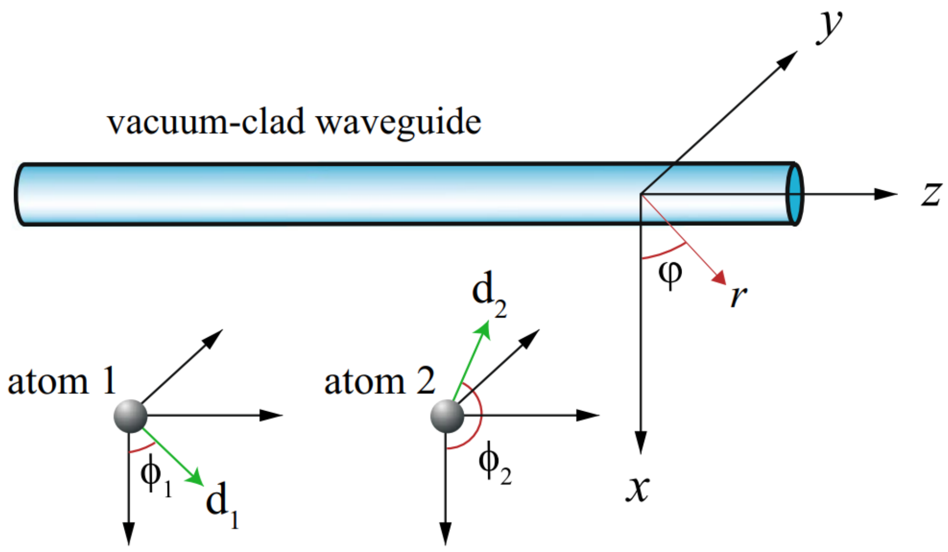

Figure 2.12: Schematic of two TLS near a cylindrical waveguide in the vacuum. Taken from [3].

and dipole response at all frequencies [235]

$$C_6 = \frac{3\hbar}{16\pi^3\epsilon_0^2}\int_0^\infty du \frac{\alpha_j(iu)\alpha_k(iu)}{\epsilon^2(iu)}, \tag{2.50}$$

which reduces to the expression in the vacuum for isotropic two-level atoms

$$\bar{C}_6 = \frac{d_j^2 d_k^2}{48\pi^2\hbar\epsilon_0^2\omega_0}. \tag{2.51}$$

For example, taking only the D2 transition of a ground-state caesium atom into account, one obtains [244] $d = 3.80 \times 10^{-29}$ Cm, yielding $\bar{C}_6 \approx 2.42 \times 10^{-73}$ Jm^6. In the presence of inhomogeneity, a $C_{6/7}$ coefficient alone will be insufficient to describe the dispersion interaction in either regime.

Dispersion interactions mediated through a cylinder

I now advance to the case of dispersion interactions featuring both anisotropic polarizabilities and inhomogeneous background media. Concretely, I consider a cylindrical medium, outside of which (in the vacuum) the emitters are situated – the setup is shown in Fig. 2.12. Due to cylindrical symmetry the (reflected part of the) Green's function can be determined analytically as the infinite sum over effective wavevectors, polarizations, and azimuthal mode number for both source and receiver outside of fiber [85]

$$\mathbf{G}^{(R)}(\mathbf{r},\mathbf{r}',\omega) = \frac{i}{8\pi}\sum_{\mathbf{F},\mathbf{F}'=\mathbf{M},\mathbf{N}}\sum_{n=-\infty}^{\infty}\int_{-\infty}^{\infty} d\beta \frac{R^n_{\mathbf{F}\mathbf{F}'}(\beta)\mathbf{F}_n(\beta,\mathbf{r})\otimes\mathbf{F}_n'^{*}(\beta,\mathbf{r}')}{\left(\sqrt{k^2-\beta^2}\right)^2}, \tag{2.52}$$

where the cylindrical vector functions $\mathbf{M}_n, \mathbf{N}_m$ correspond to TE/TM modes of the cylindrical geometry with azimuthal mode number n

$$\mathbf{M}_n(\beta, \mathbf{r}) = \nabla \times [\phi_n(\beta, \mathbf{r})\hat{\mathbf{z}}], \tag{2.53}$$

$$\mathbf{N}_n(\beta, \mathbf{r}) = \tfrac{1}{k}\nabla \times \mathbf{M}_n(\beta, \mathbf{r}), \tag{2.54}$$

$$(\nabla^2 + \beta^2)\phi_n = 0 \implies \phi_n = J_n(\beta_\perp \rho)e^{i(n\theta+\beta z)}, \tag{2.55}$$

and $R^n_{\mathbf{FF}'}$ are the Fresnel reflection coefficients for the source outside of the fiber and can be determined by applying the boundary conditions for the Green's function [85]. Note that the cylinder permitivity dependence is implicitly contained within $R^n_{\mathbf{FF}'}$. For real frequencies and in lossless media, numerical calculation of (2.52) is intricate due to the presence of both poles and branch points on the real axis [85, 107]. However, when imaginary frequencies are considered, the integrand is regular on the real axis. Combined with exponential decay of the integrand in β, I simply perform the integral in (2.52) for each n, and terminate upon sufficient convergence of the sum.

2.6.4 Findings

The key observation underlying this investigation lies in the fact that, considering emitter anistropy, one sees in the vacuum that

$$\mathbf{d}_j \cdot \mathbf{G}^{(0)}(\mathbf{r}_j, \mathbf{r}_k, iu) \cdot \mathbf{d}^*_k = 0,$$

for all $u > 0$ when the following are satisfied

$$\mathbf{d}_j \perp \mathbf{d}^*_k, \tag{2.56}$$

$$(\mathbf{d}_j \cdot \hat{\mathbf{R}})(\mathbf{d}^*_k \cdot \hat{\mathbf{R}}) = 0, \tag{2.57}$$

as a consequence of the vacuum plane-wave polarization. This condition yields a complete annihilation of the dispersion potential $U_{jk} = 0$ for all such configurations satisfying (2.56), and shows that preferred and distinct anisotropy axes for each dipole element can produce significantly different interactions than those exhibited by aligned dipoles, even in an isotropic environment. By exploiting the dipole orientations, one can then engineer dispersion interaction mediated entirely through the cylinder: recalling the decomposition of the Green's function $\mathbf{G} = \mathbf{G}^{(0)} + \mathbf{G}^{(R)}$ into vacuum part and scattered part, one finds for emitters satisfying (2.56) that the dispersive interaction is mediated purely through the cylinder-scattered part

$$U_{jk}(\mathbf{r}_j, \mathbf{r}_k, \omega_0) = -\tfrac{2\mu_0^2}{\hbar\pi}\int_0^\infty \tfrac{du u^4 \omega_0^2}{(\omega_0^2+u^2)^2}\left[\mathbf{d}_j \cdot \mathbf{G}^{(R)}(\mathbf{r}_j, \mathbf{r}_k, iu) \cdot \mathbf{d}^*_k\right]^2, \tag{2.58}$$

so that utilising anisotropy can allow one to remove background vacuum-induced effects, offering a clearer distinction. It is the dispersion (2.58) that I investigate here, and in order to provide a meaningful comparison between the cylinder-induced dispersion potential and that of the vacuum, I propose a measure of enhancement by the ratio between the observed dispersion potential and the *dipole-averaged* potential corresponding to free space

$$\frac{U_{jk}(\mathbf{r}_j, \mathbf{r}_k, \omega_0)}{\bar{U}^{(0)}_{jk}(\mathbf{r}_j, \mathbf{r}_k, \omega_0)}. \tag{2.59}$$

The bar here denotes that the potential $U^{(0)}$ corresponding to free space should be averaged over all dipole orientations (i.e., $\boldsymbol{\alpha} \to \frac{1}{3}\mathrm{Tr}[\boldsymbol{\alpha}]\mathbf{I}$), and will be crucial as a benchmark in our study as the interaction between the two orthogonal dipole orientations is zero in free space, which naively produces an infinite enhancement factor.

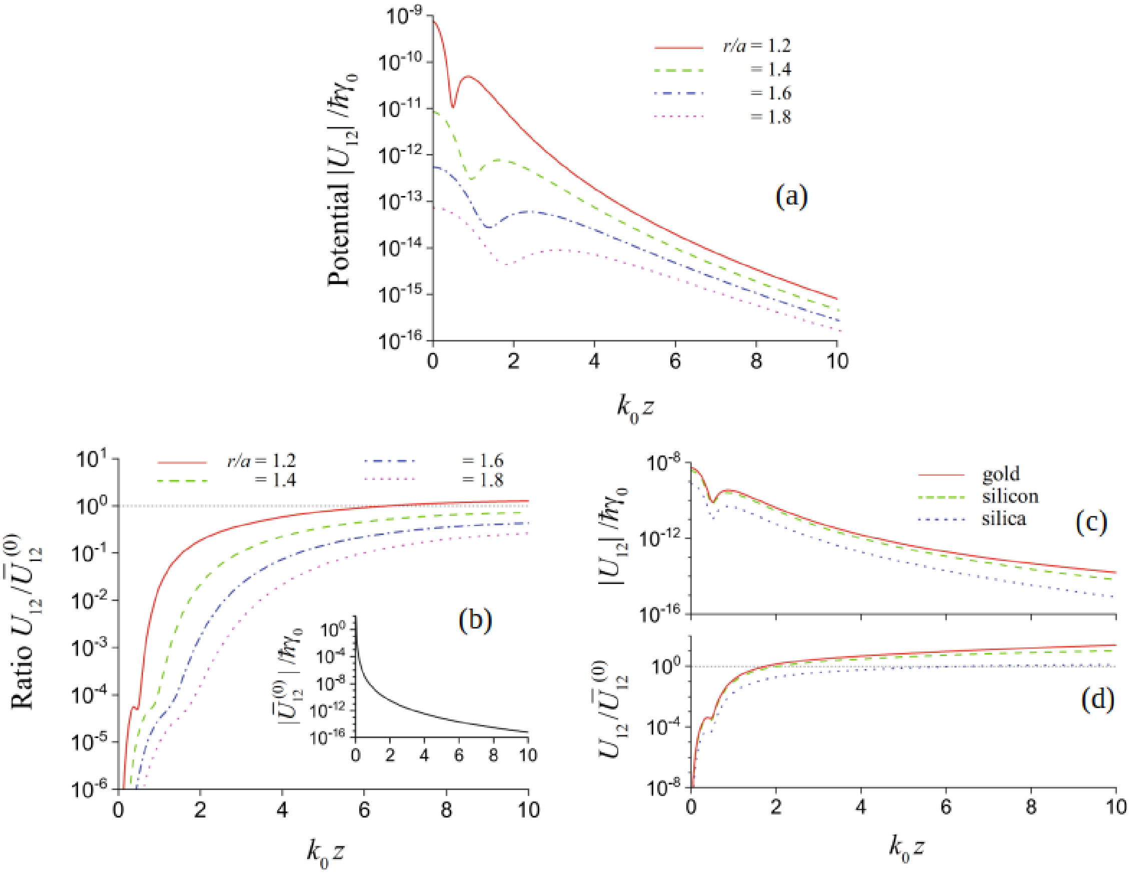

Figure 2.13: (a) Normalized absolute value of the dispersion potential as a function of normalized emitter separation $k_0z = k_0|z_1 - z_2|$ and for varying radial distance r/a in for emitters the vicinity of a silica ONF with radius a in the vacuum. (b) Dispersion enhancement factor (2.59) with varying k_0z and r/a for a silica ONF in vacuum. The inset shows the dipole-orientation-averaged dispersion potential in free space. (c) The normalized dispersion potential (d) The enhancement factor (2.59) with varying k_0z, for the three cylinder materials gold, silicon, and silica. In all Figures the fiber radius $a = 250$ nm, the free-space wavelength $\lambda_0 = 852$ nm, and the two dipoles have the orientations in Cartesian coordinates $\mathbf{d}_1 = \frac{d}{\sqrt{2}}(1,1,0), \mathbf{d}_2 = \frac{d}{\sqrt{2}}(1,-1,0)$. Unless specified otherwise, $r/a = 1.2$. Taken from [3].

The main findings of the work can be summarized in Fig. 2.13. As can be seen in

Fig. 2.13(a), the anisotropy induced by the fiber results in potential minimum as the separation between the two emitters is varied along the (silica) cylinder axis. This is in contrast to the purely attractive interactions observed for orientation-averaged dipoles in free space. Whilst not averaging in free space can produce repulsive interactions [42, 43], the potential is still monotonic as a function of distance. In contrast, provided that confinement in the radius and axial directions are provided in our case, one observes in Fig 2.13(a) that a stable binding of the two emitters is possible in the z-direction purely by virtue of the cylinder-mediated dispersion forces. This is not a violation of the no-go theorem [243] for dispersion mediated stable-binding configurations in ground state atoms as, similarly to that in the two-waveguide trap [34, 61], stable configurations via dispersion forces are possible along at most 2 axes, provided that a restoring mechanism is present along the others. The potential dip was also observed in the cylindrical geometry in [39], but for identically oriented dipoles, the monotonic vacuum contribution is larger and generally washes out the potential minimum. In Fig. 2.13 (b) and (d), one can further see a drastic reduction of the dispersion potential relative to the dipole-averaged free-space potential. Indeed, whilst the free-space potential diverges as (2.46), the contribution (2.58) from the cylinder tends to a finite value (seen in (a,c)) in the near-field. The vacuum free-space contribution always produces a divergence in the near field so that to annihilate this contribution the dipole orientations must be specifically chosen. The final key feature of the cylinder-induced dispersion can be seen in Fig. 2.13 (b,d), where the cylinder enhances the dispersion potential beyond the vacuum averaged dispersion potential for large separations. This is not an enhancement of the power-law [39, 41], but reflects the enhanced confinement of the guided modes over a range of frequencies contributing to the dispersion potential. Despite the loss present, for materials seeing large $\mathfrak{R}[\epsilon]$ (such as gold and silicon), an enhancement of the dispersion potential is observed over longer distances. Due to the lossy nature of these materials, however, the enhancement may be expected to be reduced for greater separations z.

2.6.5 Publication [3]: Waveguide-induced dispersion interaction between two two-level atoms with orthogonal in-transverse-plane dipoles

The main results of this chapter are published in

Waveguide-induced dispersion interaction between two two-level atoms with orthogonal in-transverse-plane dipoles
FL Kien, L Ruks, T Busch
Applied Physics B **125** (11), 1-7 (2019)

Dr Le Kien conceived of and initiated the project. I carried out all numerical simulations, and contributed to the analytical considerations of the dispersion potential. All authors contributed to the interpretation of results and writing of the later versions of the manuscript.

2.6.6 Experimental prospects

As the long-range enhancement in our setup is simply a multiplicative factor due to material, we focus on observing the dispersion with the near-field vacuum contribution cancelled at short ranges. As can be seen from e.g., Fig 2.13 (b,d) in the cylindrical geometry the largest dispersion induced collective frequency shift is on the order of $10^{-8}\gamma_0 \sim 2\pi\times 0.52$ Hz ~ 0.025 nK for $z=0$ and in the case of gold, so that the effect is currently far too small to be observed in existing cold-atom-ONF style platforms [158]. As explored in [41], performing this experiment in superconducting transmon qubits coupled to a coplanar-waveguide transmission line in principle allows the resulting collective frequency shift (due to finite contribution from the TEM mode) to be on the same order or larger than dephasing and decay, and so should in principle be observable in terms of magnitude only. Experimentally the qubit orientation, and thus the dipole orientation, can be modulated by physically rotating the qubits [245, 246], which in turn allows one to tune coupling with the waveguide modes. However, more detailed calculations are necessary due to the differing polarization structure in transmission lines.

2.6.7 Conclusions and outlook

In this section I explored the dispersion potential between two neutral polarizable emitters in the ground state, in the presence of a dielectric cylinder and when preferred and distinct dipolar orientations are selected for the emitters. Choosing the dipole orientations and emitter separation vector all to be orthogonal to one another results in a zero dispersion potential due to transverse free-space modes at all frequencies. This resulted in a zero dispersion potential at all distances, in contrast to the power-law divergence and decay observed in the near- and far-field respectively for isotropic dipoles. In the presence of a dielectric cylinder, anisotropy due to scattering from the cylinder re-couples the two emitters, so that a dispersion potential purely due to cylinder scattering is obtained. This dispersion potential was numerically investigated as a function of the emitter separation along the cylinder axis, for different dispersive and absorbing materials, and found that the dispersion potential can be severely diminished compared to free space in the near-field, or enhanced in the far field, with a stable potential minimum appearing in the intermediate regime. The near-field diminishing is due to the cancellation of the divergent vacuum contribution to dispersion, whilst the far-field enhancement is due to the presence of guided modes of the cylinder.

Since publication, the work comprising this chapter [3] has seen reference in [247], where the dispersion potential in band-gap style cylindrically layered media was investigated, where dispersion was found to be inhibited with increasing emitter separation along the cylinder axis (e.g., as in [39, 248]). In [249], the many magnetic sub-levels and distinct dipole orientations corresponding to these transitions were summed up to give experimental predictions for the dispersion potential for a single realistic multi-level cesium atom in the vicinity of an ONF.

Chapter 3

Quenches Across a Phase Transition in Quantum Metrology

3.1 Introduction

3.1.1 Background

Measurement is a core aspect of any physical science, and the central aim of quantum metrology is to use the additional correlations available to quantum system in order to improve measurement precision beyond that obtainable in classical systems, with all other resources set equal. Specifically, whilst measurement by N classically uncorrelated probes produces a sample deviation of the sample mean scaling as $1/\sqrt{N}$ (the *standard quantum limit* (SQL)), entanglement between the probes allows one to go beyond; for example, using maximally entangled states of N two-level atoms, one obtains a $\frac{1}{N}$ scaling [250] bound for precision determined by fundamental quantum uncertainty. Our understanding of quantum metrology, and protocols along with it, have been theoretically developed over many decades [251, 252, 253, 254], with improvements over the SQL realised in proof-of-concept experiments[250, 255, 256] in a range of platforms. By their nature, advancements in quantum metrology are intertwined with a deepened understanding of quantum systems, and a recent avenue exploiting a fundamental quantum phenomenon for metrological purposes is *critical quantum metrology* [47, 48, 49, 257, 258]. Critical quantum metrology exploits high system sensitivity to parameters driving a phase transition when near the critical point to generate a correspondingly high sensitivity in parameter estimation. These protocols use well-established and robust adiabatic preparation [259, 260] of the ground state near the phase transition as part of a dynamic protocol that further takes into account the system preparation time, also an important resource in metrology [260]. On one hand, critical metrological protocols have been shown to operate in some circumstances at the optimal limit [48] (albeit with the requirement of nonstandard measurements), whilst in other systems only a modest and sub-optimal improvement of scaling over the SQL has been achieved [49, 260, 261]. Critical quantum metrology remains in an early stage, and whilst the standard approach of (non-adiabatic) evolution near the critical point is commonly studied, it is crucial to contrast this approach with alternatives in order to understand the limits and assess suitability for specific applications.

3.1.2 Chapter outline

In this chapter I introduce key concepts in quantum metrology and critical quantum metrology. Within the archetypal Dicke model of cavity QED, I discuss the possibility of exploiting quenches across the superradiant phase transition as a dynamical metrological protocol in critical quantum metrology, as opposed to the commonly employed (non)-adiabatic evolution near the vicinity of the critical point and in a single phase. In this framework, I summarize my calculations detailing system evolution following a quench in the Dicke model and the statistics of the homodyne measurement performed after the quench; my calculations were used in showing that the optimal sensing with a sensitivity exponentially increasing in time can be achieved using this protocol. More generally, the calculations play a role in showing that quenches across the critical point followed by homodyne measurement in the Dicke model (which is realised in a host of quantum platforms) can be used for optimal sensitivity in a simple protocol that takes into account probe preparation, and offers an alternative approach to precision sensing in critical quantum systems.

3.2 Quantum Metrology in critical systems

The basic idea of metrology is to gain information on a system parameter λ by making measurements. To see this effect in action, consider an unbiased estimator $\hat{\Theta}$ of a system parameter λ classically, such that

$$E[\hat{\Theta}|\lambda] = \lambda. \tag{3.1}$$

A bound on the variance can be provided by the *classical Fisher information* (CFI) $\mathcal{F}$

$$\mathrm{Var}[\hat{\Theta}] \geq \frac{1}{\mathcal{F}(\lambda)}, \tag{3.2}$$

which is given by

$$\mathcal{F}(\lambda) = \int dx \left(\frac{\partial \log f(x;\lambda)}{\partial \lambda} \right)^2 f(x;\lambda), \tag{3.3}$$

where $f(x;\lambda)$ is the underlying probability distribution of observing x given that the true parameter is λ. Classically, one estimates λ by repeating N independent runs of the experiment, inducing an estimator $\hat{\Theta}_j$ for each run and an overall distribution $f_N(\mathbf{x};\lambda) = \prod_{j=1}^{N} f(x_j;\lambda)$. Fisher information is additive under independent runs, $\mathcal{F}_N(\lambda) = N\mathcal{F}(\lambda)$, so that the (say) unbiased estimator $\hat{\Theta}_N = \frac{1}{N}\sum_{j=1}^{N} \hat{\Theta}_j$ satisfies

$$\mathrm{Var}[\hat{\Theta}_N] \geq \frac{1}{\mathcal{F}_N(\lambda)} = \frac{1}{N\mathcal{F}(\lambda)}, \tag{3.4}$$

that is, N independent measurements may yield a variance reduced by a factor of N – the SQL. However, no such statement is made for correlated probe measurements. By utilising quantum correlations in conjunction with non-local measurements, one may hope to surpass this limit. When estimating a parameter λ of a quantum system, one prepares the density matrix $\hat{\rho}(\lambda)$ and the positive operator-valued measurement that together define a probability distribution and the corresponding CFI. The quantum Fisher information (QFI) is then given as the maximum of the CFI over all choices of positive operator-valued measurements [262], and the quantum Cramer-Rao (CR) bound then is naturally defined in analogy with the CFI as

$$\mathrm{Var}[\hat{\Theta}] \geq \frac{1}{\mathcal{I}(\lambda)}, \tag{3.5}$$

for the QFI $\mathcal{I}(\lambda)$. Its expanded state space allows one to go beyond the $\frac{1}{N}$ scaling in variance set by classical uncorrelated probes. At an absolute maximum, the QFI may scale as the size of the Hilbert space, resulting in $\mathcal{I} \sim 2^N$ in a system of N spins [263]. However, in the typical physical scenario, where for each N there are k-body (for constant k) parameter-sensitive coupling terms present, one instead observes a scaling $\mathcal{I} \sim N^k$ [264]. At face value, there is then an attractive enhancement to be gained in metrology by exploiting the larger quantum state space. In practice, however, the time taken to prepare the system also constitutes a finite resource. This can be accounted for by allowing the density matrix $\hat{\rho}$ to be time dependent, evolving according to the preparation procedure until measurement. Recent investigations have accounted additionally for the time taken to prepare probes states [265, 266, 267] as part of dynamical metrological protocols, which often gives a sobering reality check on apparently attractive protocols that can require longer state preparation times [260]. In the following I discuss the case of metrology in critical quantum systems, where state preparation time is of crucial importance.

3.2.1 Critical quantum metrology

Given the system parameter λ, one may quantify how eigenstates (say, the ground state) $|\Psi(\lambda)\rangle$ change under (adiabatic) variation of λ via the fidelity susceptibility $\chi(\lambda)$

$$|\langle\Psi(\lambda)|\Psi(\lambda+d\lambda)\rangle| = 1 - \frac{1}{2}\chi(\lambda)(d\lambda)^2 + O((d\lambda)^3), \tag{3.6}$$

where $\chi(\lambda) = \frac{1}{4}\mathcal{I}(\lambda)$ [260]. Assuming that λ can drive a quantum phase transition, one expects a divergence in the susceptibility of system states around the transition in the thermodynamic limit (or a maximum in a finite system), which has been explored extensively in the context of metrology [49, 257, 260] and naively corresponds to a diverging QFI. However, despite the surface-level divergence one observes in the QFI, inclusion of the (diverging) time taken to adiabatically prepare a near-critical state restores the realised QFI within the CR bound [260], and often produces sub-optimal sensitivity in the form of a small constant prefactor [49] or a reduction in the power-law scaling of the QFI with the number of elementary subsystems N either up until a given time [260], or even for all times [48]. Further, attempts to compensate for time using optimized non-adiabatic state preparation (*shortcuts to adiabaticity*) over arbitrarily short times have recently been show to fail in attaining the Heisenberg limit in general [261]. Nonetheless, critical quantum metrology in principle has the potential to provide optimal sensing and represents a novel fusion of two current topics of great interest yet in its early stages.

However, one might instead ask about the effect of quenching *through* the critical point, which in general takes the system out of the ground state. Recent studies have shown quenches near the critical point within a single system phase can rapidly generate squeezing [268] useful for metrology and allow for sensitivity saturating the CR bound up to a constant prefactor [47, 48], although these results say nothing with respect to the QFI theoretically obtainable when quenching through the critical point. In the following, I present my calculations detailing the evolution of the archetypal *Dicke model* when quenched across the superradiant phase transition, along with the measurement statistics corresponding to the consequent homodyne measurement. In the bigger picture, my calculations have formed a key component of a proposal with my collaborator Dr. Karol Gietka showing that quenches across phase transitions can be employed as an alternative metrological protocol optimally saturating the CR bound in critical quantum systems.

3.2.2 Dicke model

The famous Dicke model [45, 46, 269] describes a privileged bosonic mode interacting with a collective spin via the dipole-coupling style Hamiltonian

$$\hat{H}_{\mathrm{D}} = \Omega \hat{S}^z + \omega \hat{a}^+ \hat{a} + \frac{g}{\sqrt{N}}(\hat{a} + \hat{a}^+)\hat{S}^x, \tag{3.7}$$

for spin frequency Ω, boson frequency ω, and coupling (Rabi frequency) g. The spin operators satisfy $[\hat{S}^\alpha, \hat{S}^\beta] = i\epsilon_{\alpha\beta\gamma}\hat{S}^\gamma$, with $\hat{S}^{x2} + \hat{S}^{y2} + \hat{S}^{z2} = S(S+1)$ for spin length $S = N/2$ (N is the number of contributing spin-1/2 systems) whilst the bosonic commutation relation $[\hat{a}, \hat{a}^+] = 1$ is satisfied. The Dicke model has been realised in the context of coupling a cavity to the bosonic phonon modes of ultracold gases [270], similarly in the coupling of center-of-mass excitations to spins in a Coulomb crystal [271], and finally for atoms in optical cavities, using Raman-laser-assisted transitions [272]; attempts to realise the Dicke model are aplenty due to its relevance to fundamental quantum mechanics and applied quantum optics. On the one hand, the Dicke model offers a particularly simple construction for a quantum system featuring a zero-temperature phase transition, and is a rich playground for studying entanglement, quantum chaos [273], and quantum information [274]. On the applications side the coherent pumping mechanism offered by the counter-rotating terms allows for the study of lasing-like dynamics [275], whilst the possibility to generate entangled cat states [271, 276] offers a promising metrological resource for quantum sensing.

The superradiant phase transition

For our purposes, the key feature of the Dicke model is the *superradiant phase transition.* The number of total excitations

$$\hat{N} = \hat{a}^+ a + \hat{S}^z + N/2, \tag{3.8}$$

gives a conserved quantity in the parity $\hat{P} = (-1)^{\hat{N}}$, whose symmetry characterises the two phases of the system: the *normal* phase and the *superradiant* phase, where the ground states preserve/spontaneously break the symmetry respectively. One may analyze the thermodynamic limit $S \to \infty$ using a mean-field approximation [269, 277] to find a phase transition at the critical coupling strength

$$g_c = \sqrt{\Omega\omega}. \tag{3.9}$$

In the original quantum model (3.7) in the thermodynamic limit, one finds an energy gap $\sqrt{\delta_e}$ scaling near the critical point as

$$\sqrt{\delta_e} \sim \omega\sqrt{1 - \frac{g^2}{g_c^2}}, \tag{3.10}$$

which is responsible for the critical slowing down [48, 258, 260] experienced by adiabatic protocols evolving the system in the ground state near the critical point. Beyond the critical point, the former vacuum(-like) ground state with $\langle\hat{a}\rangle/\sqrt{N} \sim 0$ becomes unstable, birthing two symmetry-broken ground states with macroscopic bosonic occupations near the transition scaling as

$$\frac{\langle\hat{a}\rangle}{\sqrt{N}} \sim \pm\left(\frac{g}{g_c} - 1\right)^{1/2}. \tag{3.11}$$

The instability of the vacuum ground state combined with the macroscopic photonic occupation in the new ground state provides the ingredients for generation of large photon numbers on short timescales. Before moving on to the metrological protocol exploiting this phenomena, I detail the dynamical evolution of the Dicke model beginning from the vacuum state and present my calculations.

3.2.3 Quenches across the superradiant phase transition

Analysis of the Dicke model near the thermodynamic limit can be greatly simplified by a Schrieffer-Wolff transformation [278] that provides an effective spin-free description in terms of free-field evolution combined with squeezing. For $\frac{\omega}{\Omega} \to 0$, the Schrieffer-Wolff transformation [278] yields the low-energy effective Gaussian Hamiltonian $\hat{H}_G$ for the bosonic mode only when projected onto the spin-down state $|{\downarrow}\rangle$ with $\hat{S}^z$ eigenvalue $-N/2$

$$\langle{\downarrow}|\frac{\hat{H}_{\mathrm{D}}}{\omega}|{\downarrow}\rangle \approx \frac{\hat{H}_{\mathrm{G}}}{\omega} = \left(1 - \frac{g^2}{2g_c^2}\right)\hat{a}^{+}\hat{a} - \frac{g^2}{4g_c^2}(\hat{a}^{+2} + \hat{a}^2) = \frac{\omega}{2}\left(\hat{p}^2 + \left(1 - \frac{g^2}{g_c^2}\right)\hat{x}^2\right), \tag{3.12}$$

for the standard quadrature $\hat{\mathbf{x}}, \hat{\mathbf{p}}$. With this approximation the spectrum is unbounded from below for $g > g_c$ and (3.12) can not be used to describe the eigenstates there, but for an initially prepared vacuum state, the Hamiltonian is valid dynamically for photon numbers up to the order of [279]

$$\langle\hat{n}\rangle = \langle\hat{a}^{+}\hat{a}\rangle \sim \frac{N\Omega}{\omega}\left(\frac{g^2}{g_c^2} - \frac{g_c^2}{g^2}\right), \tag{3.13}$$

i.e., until the higher powers of $\hat{a}$ become relevant. In the following I assume (3.13) to be valid, which can always taken to be the case by choosing N large. The resulting Hamiltonian is quadratic in the bosonic operators and can be solved exactly in the Heisenberg picture via a Bogoliubov transformation. The linear equations of motion are obtained as

$$\frac{d}{dt}\begin{bmatrix} \hat{a}^{+} \\ \hat{a} \end{bmatrix} = i\omega \begin{bmatrix} 1-\frac{g^2}{2g_c^2} & -\frac{g^2}{2g_c^2} \\ \frac{g^2}{2g_c^2} & -(1-\frac{g^2}{2g_c^2}) \end{bmatrix} \begin{bmatrix} \hat{a}^{+} \\ \hat{a} \end{bmatrix} = iA \begin{bmatrix} \hat{a}^{+} \\ \hat{a} \end{bmatrix}, \tag{3.14}$$

yielding

$$\begin{bmatrix} \hat{a}^{+}(t) \\ \hat{a}(t) \end{bmatrix} = \exp(iAt) \begin{bmatrix} \hat{a}^{+}(0) \\ \hat{a}(0) \end{bmatrix}. \tag{3.15}$$

Assuming an inital vacuum state, the first moments vanish at all times and the (Gaussian) system is completely characterised by the second moments. As a key example, the photon number is then given by

$$\langle \hat{n} \rangle (t) = \frac{1}{2\left|\frac{g_c^2}{g^2}-\frac{g^2}{g_c^2}\right|}\frac{g^2}{g_c^2}\left|\sin\left(\omega t\sqrt{1-\frac{g^2}{g_c^2}}\right)\right|^2, \tag{3.16}$$

displaying an exponential growth due to squeezing as the vacuum is unstable in the superradiant phase [280]; this growth is analogous to that observed in classical linear dynamical systems, and is central to the metrological proposal for quenching across a phase transition

3.2.4 Metrological protocol

With the Dicke model and salient evolution dynamics established, I now briefly present the proposed metrological protocol. Concretely, we consider to prepare an initial vacuum photonic state corresponding to the ground state of the Dicke Hamiltonian (3.7) deep within the normal regime $g \ll g_c$. We then quench the system (far) into the superradiant phase $g \gg g_c$, and after some time perform the square of the measurement $\hat{Q}$ defined by an angle ϕ

$$\hat{Q}(\phi) = \frac{\hat{a}e^{i\phi} + \hat{a}^{+}e^{-i\phi}}{\sqrt{2}}, \tag{3.17}$$

which has been shown to offer (near)-optimal measurement in a number of quantum metrological protocols [48, 49, 281], although the optimal homodyne measurement in the superradiant phase has not been treated to my knowledge. In our case we can choose to measure the bosonic or spin frequency, $\lambda = \omega, \Omega$, but the general conclusions remain identical. As the QFI associated with measuring the frequency λ of the single-mode bosonic systems scales as $\mathcal{I}(\lambda) \sim \langle \hat{n} \rangle^2$ [253], one could expect at most exponential growth of the QFI in time according to (3.16). Indeed, numerical simulations in the full Dicke model performed by Dr Gietka [4] confirm the exponential growth of QFI with a leading order scaling

$$\mathcal{I}(\lambda) \sim \exp(\sqrt{|\delta_e|}t), \tag{3.18}$$

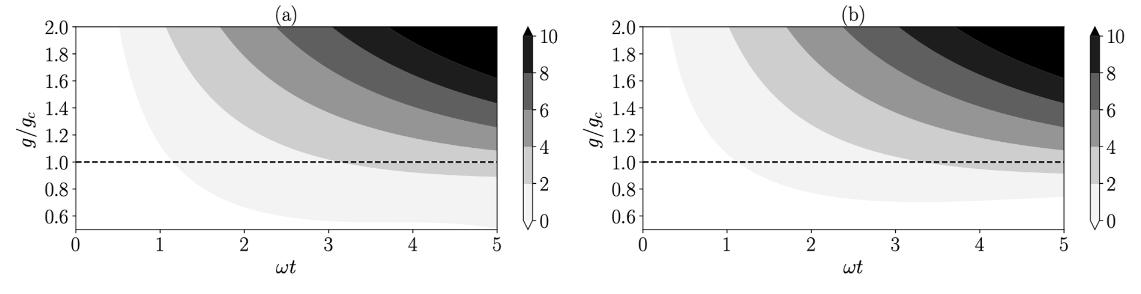

Figure 3.1: Logarithm of the normalized QFI $\log(\mathcal{I}(\lambda)\lambda^2)$ for (a) $\lambda = \omega$ (b) $\lambda = \Omega$ as a function of normalized time $t\omega$, and the normalized coupling g/g_c. The dashed line indicates the critical point $g = g_c$ for comparison. Taken from [4].

which is shown in Fig. 3.1, for measurement on ω or Ω. Recalling the definition (3.10), this indeed means that in the superradiant phase $\mathcal{I} \sim \langle \hat{n} \rangle^2$ to leading order. In summary, a quench into the superradiant phase triggers an exponential growth of photons over time, which in turn is associated with an exponentially growing QFI. The squeezing of the photons results in the factor of $\mathcal{I} \sim \langle \hat{n} \rangle^2$. It remains to show that the QFI can be saturated using a practically realisable measurement, which I show to be the case for a homodyne detection scheme in the following.

Homodyne detection

As our Hamiltonian is Gaussian and the homodyne measurement is linear, the resulting distribution for the measurement statistics of the evolved state is also Gaussian. Furthermore, the Hamiltonian (3.12) does not displace the photonic state away from the vacuum, so that $\langle \psi(t;\lambda) | \hat{Q}(\phi) | \psi(t;\lambda) \rangle = 0$, for the initial vacuum state $|\psi(0)\rangle$. As mentioned previously, we can characterise the measurement by the second moment

$$\langle \psi(t;\lambda) | \hat{Q}^2(\phi) | \psi(t;\lambda) \rangle. \tag{3.19}$$

Indeed, considering the CFI for a Gaussian distribution with parameter dependence variance and zero mean, we see that the Fisher information for the second-moment measurement on the evolved state admits the simple expression

$$\mathcal{F}_{\hat{Q}(\phi),|\psi\rangle}(t;\lambda) = \mathcal{F} = \frac{(\partial_\lambda E[\hat{Q}(\phi)^2])^2}{\mathrm{Var}[\hat{Q}(\phi)^2]}, \tag{3.20}$$

where expectations are taken in the state $|\psi(t;\lambda)\rangle$. In the superradiant phase one sees from the linear equations (3.14) that all products of operators will exponentially grow/decay in time, or be constant. Exact expressions are in general cumbersome and are given in [4], but the particular case of $g = \sqrt{2} g_c$ (corresponding to pure squeezing in (3.12)) gives the simple expression when ω is considered the unknown parameter

$$\mathcal{F}(t;\lambda) = \frac{2\cos^2(2\phi)\sinh^4(\omega t)}{\omega^2(\cosh(2\omega t) - \sin(2\phi)\sinh(2\omega t))^2}. \tag{3.21}$$

Fixing $\phi = \pi/4 - \epsilon/2$ for $\epsilon \ll 1$ one finds

$$\mathcal{F}(t;\lambda) \approx \frac{2\epsilon^2 \sinh^4(\omega t)}{\omega^2(\cosh(2\omega t) - (1-\epsilon^2/2)\sinh(2\omega t))^2}, \tag{3.22}$$

whilst for $t \gg \log(\epsilon)/\omega$ one drops all the exponentially small terms in t and the notable result is obtained

$$\mathcal{F}(t,\lambda) \sim \frac{1}{2\omega^2(\phi - \pi/4)}. \tag{3.23}$$

That is, the Fisher information can be made arbitrarily large over time scales (ignoring the relatively inconsequential $\log\epsilon$) $t \sim \omega^{-1}$ provided one has precise control over the quadrature angle. In general, one can produce an arbitrarily large QFI for any final value of g/g_c, but as per the earlier discussion, one should ensure to choose the quadrature within range of the optimal angle

$$\phi_{\text{opt}} = \cos^{-1}\left(\sqrt{\left|1 - \frac{g^2}{g_c^2}\right|}\right), \tag{3.24}$$

which can be seen in Fig. 3.2. As ϕ is chosen futher from ϕ_{opt}, one observes a long-time CFI exponentially smaller than the QFI, which saturates according to (in the example of $g = \sqrt{2}g_c$) (3.23). In existing works [48, 49, 281] it is typically implicitly assumed that a quadrature measurement for any given ϕ is exactly attainable, whilst these results show that in practice small deviations from the desired value can result in an obtainable CFI even exponentially smaller than the QFI. In addition, this result extends the results of [49] to show that standard quadrature measurements can also in principle be optimal in the superradiant phase of the Dicke model.

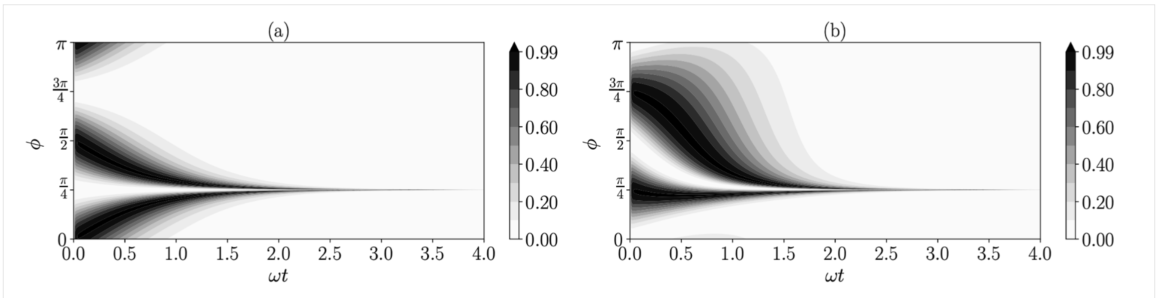

Figure 3.2: Ratio of the classical Fisher information induced by the quadrature measurement $\hat{Q}(\phi)$ to the quantum Fisher information $\mathcal{F}_{\hat{Q}}(\lambda)/\mathcal{I}(\lambda)$ as a function of normalized time ωt for (a) $\lambda = \omega$ (b) $\lambda = \Omega$. Taken from [4].

,

3.3 Publication: Understanding and Improving Critical Metrology. Quenching Superradiant Light-Matter Systems Beyond the Critical Point[4]

The results presented in this chapter are contained in the manuscript [4] as

Understanding and Improving Critical Metrology. Quenching Superradiant
Light-Matter Systems Beyond the Critical Point
K Gietka, L Ruks, T Busch
Quantum **6**, 700 (2022)

The project was conceived of and initiated by Dr Gietka. In addition, the numerical simulations and the analytical results concerning the QFI was obtained by Dr Gietka. I carried out the analytical calculations concerning the dynamical evolution of the Dicke model under the Schrieffer-Wolff transformation, and the calculations concerning the CFI under the quadrature measurement scheme, which was used to compare with numerics in Fig. 3.2. All authors contributed to the interpretation of results and the editing of the later versions of the manuscript.

3.4 Conclusions and outlook

I have derived the exact evolution for the quadratic bosonic Hamiltonian dynamically approximating the Dicke model and used it to obtain exact analytical forms for the CFI under the quadrature measurement. In conjunction with the results of my collaborator Dr. Karol Gietka, we found that that quadrature measurements of the bosonic mode of a Dicke mode quenched deep into the superradiant regime can result in a measuring sensitivity exponentially increasing with time and saturating the CR bound, which also shows for the first time that homodyne measurements can be optimal in the superradiant phase. I have additionally derived the long-time limit of the FI obtained in the homodyne measurement, and shown that it is also bounded in practice by the precision with which the quadrature angle in the detection scheme can be prepared; this final result serves as a reminder that the ability to prepare the desired measurement basis is also a limiting factor in metrology.

In the greater picture this work sheds light on quenches in quantum critical systems as part of quantum metrological schemes operating at or near the fundamental Heisenberg limit, in contrast to protocols operating near, but not beyond, the critical point. In addition, the saturation of the QFI using quadrature measurements in the superradiant phase is also a novel result, whilst the observation that obtainable FI is bounded by controlability of the measurement device is also not typically addressed in the field. Since publication, our work has been cited and used as a platform for further study of dynamical quantum metrological protocols in critical systems, including a nonlinear Rabi model [282] and in the sensing of qubit frequency when coupled to a two-photon

Kerr resonator [283]. Moving forward, further theoretical investigations are required to determine in what practical scenarios the standard approach of critical quantum metrology and our proposed approach of quenching are appropriate. An additional avenue is to explore the protocol experimentally. The scheme can in principle be applied to any setup simulating the Dicke model, from optical cavities [284], to ion traps [271], and ultracold gases [270]. In these setups either the frequency of the bosonic or the spin mode can be measured using this scheme. Indeed, the (dynamical) phase transition and exponential growth of photons has been experimentally observed in the self-organization of a Bose-Einstein condensate coupled to an optical cavity in [285], and this platform is routinely realised, making it ideal for realising the protocol.

Chapter 4

Wave Propagation and Emission in Discrete Baths Exhibiting Hyperbolic Dispersion

4.1 Background

In the previous chapters I have introduced two ends of the spectrum in quantum optics; one is the single-mode optical cavity, whilst the other is the open optical nanofiber supporting a continuum of modes. For spatially extended systems exhibiting a *discrete* translational symmetry, however, one gains access to both control over dimensionality and dispersion of travelling waves, which offers new degrees of control over the excitations in the bath. Originally, these structured baths were manifest as photonic crystals in the optics community, where a wide range of applications were found in controlling classical waves for sensing, imaging, and information transport [17, 286]. In the quantum optics community, the endgame of bath engineering typically lies in the potential applications when coupling to a quantum emitter; here one may seek to simulate condensed matter systems in the spin degree of freedom [28], or imprint the quantum statistics generated by spins into photons [93]. The results are typically witnessed via coupling of an emitter to the bath: dispersion engineering allows for the shaping of emission in space for focussing [287], subwavelength imaging [9], and complete photonic localization [52]. In the Markovian approximation, emitter-emitter interactions mediated through a bath have an accompanying spatial dependence, which can result in coherent population transfer when the emitters are resonant outside of the band[52] or perfectly super-subradiant states in higher dimensional baths [288]. Periodic and discrete media are realisable in a host of controllable Hamiltonian systems beyond the solid-state, including photonic crystals [66, 113, 289], cold atoms in optical lattices [19], and coupled cavity-like systems in superconducting circuits [290], as well as transmission lines [291] and metamaterials [292]. With these experimental advancements, more and more exotic tailoring of baths has come within reach, and I will now introduce two particular paradigms of importance along with their current state – those of hyperbolic materials and magnetic baths.

4.1.1 Hyperbolic media

Hyperbolic media first gained attention in the optics community [293] after their initial realisation in plasmas [294]. The enhancement, instead of decay, of evanescent waves in hyperbolic materials, enables a slew of potential imaging applications [295] in these settings, with a perfect negative-refractive-index lens chief among them [296], and now analogue simulators of hyperbolic materials can in principle be realised in many of the setups mentioned previously. Specific realisations for a hyperbolic material have been reported in metamaterials [9, 55], in optical lattices [297], transmission lines [291], and coupled cavity systems [298]. Under the assumption of an effective continuum medium, hyperbolic media features both a diverging density of states [9] and a diverging decay lengths [10, 55, 299] of the system Green's function. When coupled to quantum emitters, this results in infinite broadband Purcell factors and infinite-range interactions respectively. These two features form the backbone of quantum optics investigations with hyperbolic emitters [299], with the former feature being particularly attractive when contrasted with optical cavities. The main applications include engineering of single-body [300] and collective [55] spontaneous and thermal [54, 301] emission. Recently, long-range emitter-emitter interactions mediated through hyperbolic metamaterials was experimentally observed [302], whilst hyperbolic materials coupled to optical nanofibers have been shown to act as a platform for efficient broadband single-photon collection [303].

The continuous medium approximation

Although it can offer a clear picture of the dynamics with analytically tractable calculations, the continuous treatment of hyperbolic media ignores the finite length scale of the underlying crystal used to effect the hyperbolic material, and a treatment taking into account the discrete nature of the crystal is both necessary to tame divergences and to discover the realistic contribution of finite-size effects. To this end, direct studies on the effects of discreteness in effective counterparts [11, 56] in hyperbolic media have been carried out, although inclusion of effects such as polarization and the full electromagnetic field continuum makes it difficult to establish salient physical phenomena in the former, and only a basic comparison on the spatial profile of field emission was made with the continuum case in the latter. Most recently, tight-binding lattices with similar features to hyperbolic material were investigated in the context of tilted Dirac cones [304, 305], and were shown to feature highly anisotropic and tunable emitter-emitter interactions, which can furthermore be experimentally implemented in sub-wavelength arrays of quantum emitters. However, in these studies an association with hyperbolic media was not explicitly drawn, and the focus was rather on the Dirac-cone bound states. Whilst a wealth of results exist both for structured baths treated by tight-binding models and hyperbolic media separately, the salient phenomena of emitter-emitter interactions mediated through discrete baths featuring hyperbolic-like dispersion has so far eluded investigation.

4.1.2 Magnetic baths for quantum emitters

In conjunction with all of the above techniques for dispersion engineering, an additional layer of functionality is realised when an artificial magnetic field is effected on the lattice, unlocking the power to simulate charged electrons of the solid state in a clean environment. Since theoretical proposals in the 2010s [306, 307, 308] experimental realisations of artifical magnetic fields, or *artifical gauge fields* in real space have been reported in photonic [309], cold-atom [310], and superconducting qubit [311] systems, where as an added bonus effective magnetic field strengths far exceeding their condensed matter counterparts can be realised. Whilst topological bosonic lattices are of interest with simulation of the solid-state in mind, in the past 10 years the introduction of nonlinearities in the form of quantum emitters have gained attention through theoretical investigations. On the one hand, qubits may be coupled en-masse to sites of the bath, creating a playground to explore strongly interacting topological phases of matter [312, 313]. On the other hand, the case of few emitters may be employed to study decay into topological baths [314, 315] and the associated emitter-emitter interactions. In two dimensions in particular, a magnetic field pointing out of the lattice naturally defines a setup akin to the 2D electron system, albeit of strongly interacting polaritons [13] that engage in chiral and long-range interactions with one-another to allow for the study of a range of topological spin systems. Despite the separate interest in artificial gauge fields for photons, and in materials exhibiting hyperbolic-like dispersion, the two have not been studied in conjunction in the quantum optics community, to the best of my knowledge. Such a combination is well documented in the condensed matter community where many studies of magnetic fields applied to ‘quasi-1d conductors’ (materials exhibiting hyperbolic-like dispersion, or an ‘open Fermi surface’) have been carried out [316, 317, 318], and recently a link has been established between hyperbolic-like dispersion and nonlinear magneto-resistance in layered transition metal dichalcogenides [319]. However, the focus in these systems is typically on the spectral properties of the electronic system, whilst this avenue is as of yet unexplored in the context of coupled quantum emitters.

4.1.3 Background and chapter summary

Emitters coupled to structured baths have wide ranging applications from the simulation of condensed matter systems to quantum nonlinear elements in optics. Hyperbolic materials and baths subject to effective magnetic fields have applications in emission engineering and the study of topological matter respectively, but the emitter-emitter interactions of the former have not yet been investigated in the simple tight-binding toy model most suited to uncovered the salient physics, and there has also not yet been an investigation in conjunction with the latter.

In this chapter I build upon studies of toy models of structured baths by considering emission into tight-binding lattices mimicking hyperbolic media and featuring photons subject to artifical gauge fields. I explore the RDDI for two emitters coupled to a hyperbolic bath and find regimes offering directionally tunable exponentially decaying interactions between emitters and notably, interactions becoming almost purely incoherent for certain directions. Whilst exponentially decaying coherent interactions are a well-known consequence of emitters coupled beyond a band edge [28, 52, 91, 320], exponentially decaying *incoherent* interactions are a much less documented and studied phenomenon; these interactions thus open up simulation possibilities for an additional class of dissipative short-range spin models, and throw a spotlight on hyperbolic materials for use in cold-atom simulator systems.

On the other hand, I also explore the intersection of hyperbolic and magnetic baths by studying emission into a bath with anisotropic hoppings in addition to phase accumulation effected by an artificial gauge field, finding that emission into the magnetic and hyperbolic bath is quasi-1D and topologically protected. I investigate the emission profile using semiclassical theory, and demonstrate an application in the form of effective cavity modes generated in the 2D bath using the emitters as effective mirrors [7, 59]. My results offer new methods for transporting and storing photons in higher-dimensional media.

4.2 Model and basic analysis

As necessary, the approximation of considering only the lowest orbitals allows a continuum physical system (photonic crystals, atomic lattices, waveguide lattices, etc.) to be described in the single-excitation regime by the tight-binding Hamiltonian. Restricting to two dimensions, and a square-like lattice symmetry, one obtains the bosonic Hamiltonian (for $N \times N$ sites) as

$$\hat{H} = \sum_{\langle jk \rangle} J_{jk} \hat{a}_j^{+} \hat{a}_k, \tag{4.1}$$

for $[\hat{a}_j, \hat{a}_k^{+}] = \delta_{jk}$ with j indexing the lattice site with position $\mathbf{r}_j = (x_j, y_j)$, and coupling is nearest-neighbor with $J_{jk} = J_x$ (J_y) for two neighboring sites in the x (y) direction. The lattice vectors are given by $\boldsymbol{a}_{x\ (y)} = a\hat{\boldsymbol{x}}$ $(a\hat{\boldsymbol{y}})$. As the rotating frame can be used to eliminate the (identical) single-site terms, we assume that the bosonic frequency is equal to zero. The system is assumed translationally invariant, and I expand the site-localized bosonic operators in terms of momentum-localized operators as per the Bloch theorem. One therefore expands for $\mathbf{k} = (k_x, k_y)$ with $k_{x/y} = \frac{2\pi}{Na}(-N/2, \dots, N/2 - 1)$

$$\hat{a}_{\mathbf{r}_j} = \tfrac{1}{N} \textstyle\sum_{\mathbf{k}} e^{i\mathbf{k}\cdot\mathbf{r}_j} \hat{a}_{\mathbf{k}}, \tag{4.2}$$

$$\hat{a}_{\mathbf{k}} = \tfrac{1}{N} \textstyle\sum_{\mathbf{r}_j} e^{-i\mathbf{k}\cdot\mathbf{r}_j} \hat{a}_{\mathbf{r}_j}, \tag{4.3}$$

with

$$[\hat{a}_{\mathbf{k}}, \hat{a}_{\mathbf{k}'}^{+}] = \delta_{\mathbf{k}\mathbf{k}'}. \tag{4.4}$$

Substituting this into the Hamiltonian (4.1) gives the Bloch Hamiltonian

$$\hat{H} = \sum_{\mathbf{k}} \omega(\mathbf{k}) \hat{a}_{\mathbf{k}}^{+} \hat{a}_{\mathbf{k}}, \tag{4.5}$$

with $\omega(\mathbf{k}) = 2[J_x \cos(k_x a) + J_y \cos(k_y a)]$ describing the dispersion relation of the single band in the thermodynamic limit. The dispersion is shown for $J_y = 2J_x = 2J$ in Fig.

4.3(a). As the quantum problem is also linear, one may apply the Green's function in the same manner as the full continuum electromagnetic field case, namely, as the inverse of the eigenvalue operator

$$\hat{G}(\Delta) = (\Delta + i0 - \hat{H})^{-1}, \tag{4.6}$$

whilst the matrix elements describing the propagation of a bosonic excitation of frequency Δ from site k to site j are given by [321]

$$G(\mathbf{r}_j, \mathbf{r}_k, \Delta) = \langle 0 | \mathbf{a}_{\mathbf{r}_j} \hat{G}(\Delta) \hat{a}^+_{\mathbf{r}_k} | 0 \rangle, \tag{4.7}$$

where $|0\rangle$ denotes the lattice vacuum state. In the thermodynamic limit $N \to \infty$, the Green's function satisfies the discrete wave equation in the presence of a point-source [322]

$$\begin{aligned} \delta_{m,0}\delta_{n,0} = & 2\Delta G(m\mathbf{a}_x + n\mathbf{a}_y, \Delta) \\ & - J_x[G((m+1)\mathbf{a}_x + n\mathbf{a}_y, \Delta) + G((m-1)\mathbf{a}_x + n\mathbf{a}_y, \Delta)] \\ & - J_y[G(m\mathbf{a}_x + (n+1)\mathbf{a}_y, \Delta) + G(m\mathbf{a}_x + (n-1)\mathbf{a}_y, \Delta)], \end{aligned} \tag{4.8}$$

for zero-boundary-conditions at infinity, which admits the solution

$$G(\mathbf{r}_j, \mathbf{r}_k, \Delta) = G(\mathbf{r}_j - \mathbf{r}_k, \Delta) = G(\boldsymbol{\rho}, \Delta) = \frac{\mathcal{A}}{(2\pi)^2} \int_{\mathrm{BZ}} d\mathbf{k} \frac{\psi(\mathbf{k}, \mathbf{r}_j)\psi^*(\mathbf{k}, \mathbf{r}_k)}{\Delta + i0 - \omega(\mathbf{k})}, \tag{4.9}$$

where the Bloch wavefunction ψ in the square lattice takes the basic form $\psi(\mathbf{k}, \mathbf{r}) = e^{i\mathbf{k}\cdot\mathbf{r}}$, and the unit cell area is $\mathcal{A} = a^2$. In the thermodynamic limit, one integrates over the Brillouin zone (BZ) $k_{x/y} \in [-\pi/a, \pi/a]$, and the Green's function depends only on the separation $\boldsymbol{\rho} = \mathbf{r}_j - \mathbf{r}_k$ in the square lattice. We see the standard expansion in terms of system eigenfunctions and eigenvalues similarly to (1.16) in Chapter 1. The difference lies in the rotating wave approximation effectively having been already made, and the eigenvalue of the electromagnetic eigenvalue problem being equal to Δ^2. An analogous role of the Green's function Eq. (4.9) is played when considering Markovian coupling of two emitters to the bath ($|g| \ll |J_{x/y}|$)

$$\hat{H} \to \hat{H} + \frac{\Delta}{2}(\hat{\sigma}^z_j + \hat{\sigma}^z_k) + g\big[(\hat{\sigma}_j \hat{a}^+_{\mathbf{r}_j} + \hat{\sigma}^+_j \hat{a}_{\mathbf{r}_j}) + (\hat{\sigma}_k \hat{a}^+_{\mathbf{r}_k} + \hat{\sigma}^+_k \hat{a}_{\mathbf{r}_k})\big], \tag{4.10}$$

for the usual Pauli matrices with $[\hat{\sigma}^\alpha_j, \hat{\sigma}^\beta_k] = 2i\hat{\sigma}\epsilon_{\alpha\beta\gamma}\hat{\sigma}^\gamma_j \delta_{jk}$. Tracing out the bath degrees of freedom then gives the master equation (1.53) from Chapter 1, although this time we have coupling coefficients

$$\Omega = g^2 \Re[G(\boldsymbol{\rho}, \Delta)], \tag{4.11}$$

$$\Gamma = -2g^2 \Im[G(\boldsymbol{\rho}, \Delta)], \tag{4.12}$$

so that wave propagation (and thus emitter-emitter coupling in the Markovian approximation) is entirely determined by the dispersion relation $\omega(\mathbf{k})$ and the detuning Δ of the atomic frequency from the (zero) bosonic frequency. Further analysis can be made upon inspection of the imaginary part of the Green's function, which we can rewrite as a regular sum of plane waves weighted by the local density of states

$$\Gamma_{jk} = \mathcal{A} \int_S \frac{d\mathbf{k}}{2\pi} \frac{e^{i\mathbf{k}\cdot\boldsymbol{\rho}}}{v(\mathbf{k})}, \tag{4.13}$$

for the *resonant level set*, or *isosurface*, $S = S(\Delta)$, the set of all wavevectors $\mathbf{k}$ such that $\omega(\mathbf{k}) = \Delta$. The group velocity magnitude $v(\mathbf{k}) = |\mathbf{v}(\mathbf{k})| = |\nabla\omega(\mathbf{k})|$ is encountered in the denominator. To make analytical observations, one can consider the limit where $\rho = |\boldsymbol{\rho}|$ exceeds any length scale set by the variation of $\omega(\mathbf{k})$. The integrand is highly oscillatory for large ρ and a modification of the stationary phase argument for manifolds [323, 324] reveals that the dominant contribution results in a power law decay coming from the neighbourhood of the wavevector(s) $\mathbf{k}_0$ such that

$$\mathbf{v}(\mathbf{k}_0) \propto \boldsymbol{\rho}, \tag{4.14}$$

i.e., from the wavepackets propagating from the source to the receiver. Indeed, assuming that a single $\mathbf{k}_0$ exists, then in this case the full Green's function may be approximated as [5, 287]

$$|G| \sim \mathcal{A} \sqrt{\frac{|\mathbf{m}(\mathbf{k}_0)|}{|\mathbf{v}(\mathbf{k}_0) \cdot \mathbf{m}(\mathbf{k}_0) \cdot \mathbf{v}(\mathbf{k}_0)|}} \left(\frac{v(\mathbf{k}_0)}{2\pi\rho}\right)^{1/2}, \tag{4.15}$$

for the effective mass tensor $[\mathbf{m}^{-1}(\mathbf{k})]_{jl} = \frac{\partial^2\omega}{\partial k_j \partial k_l}$, exhibiting the characteristic $\rho^{(d-1)/2}$ dependence observed in the far field of a dD bath. It is long been alluded to, and has recently been clearly documented [325], that the (local) shape and (global) volume of the isosurface S has a strong connection with the far-field profile of travelling waves, and in particular, the effective emitter-emitter interactions induced. The relation is manifest for short-range interaction globally on S in (4.13), and for long-range interactions locally on S in (4.15). In order to craft emitter-emitter interactions, one then changes the shape and volume of S; in the isotropic square lattice with $J_x = J_y$, for example, S takes the form of a perfect square at $\Delta = 0$, so that wave packets with only four group velocities $\mathbf{v} \propto (\pm 1, \pm 1)$ exist. Although the Markovian approximation breaks down when coupling emitters to this non-smooth dispersion, the spatial emission profile is well-captured by this intuition, and one observes perfectly directional emission into one of four directions into the far-field, producing quasi-one dimensional waves in the 2D bath, and allowing the formation of perfectly subradiant states [288]. On the other hand, reducing the volume of S (and allowing the group velocity to go to zero) means that a large $\boldsymbol{\rho}$ is required to produce oscillations with a much smaller length scale than that set by S – the interaction range of two emitters becomes inversely proportional to the volume of S, producing long range oscillating interactions [325]. Finally, reducing the volume of S whilst retaining finite group velocity would suggest that the incoherent interactions in (4.13) should tend to zero, retaining only the coherent part Ω_{jk}. This situation naturally arises in the case of band degeneracies – *Dirac points* [50] in two dimensions and *Weyl points* [51] in three dimensions – where again the Markovian approximation breaks down, while emitter-emitter interactions resonant at the degeneracy are purely coherent. As is further witnessed in the latter, control of the shape of S as the degeneracy is approached (with respect to Δ) also allows the power-law decay of the coherent interactions to be tuned in different directions [51]. Whilst a plethora of effective emitter-emitter interactions are available by these simple modulations of the dispersion relation, within the tight-binding model one may effect particularly exotic dispersion when the (nearest-neighbor) interaction is allowed to be anisotropic and/or complex. These cases give rise to the hyperbolic-like media and to *artifical gauge fields* for photons respectively. As I show, the former is directly an application of modifying the shape of the dispersion relation, and I begin with this.

4.3 Hyperbolic media

4.3.1 Continuum medium analysis

Hyperbolic media were traditionally considered in the context of continuum dielectric materials, and I first discuss them in this context in order to contrast with the discrete case of the tight-binding lattice. Considering a non-magnetic material with diagonal and anisotropic permitivity in the Cartesian basis, $\epsilon_{xx} = \epsilon_\perp, \epsilon_{yy} = \epsilon_\perp, \epsilon_{zz} = \epsilon_\parallel$, the dispersion relation is given by [9]

$$\frac{k_x^2 + k_y^2}{\epsilon_\parallel} + \frac{k_z^2}{\epsilon_\perp} = \left(\frac{\omega}{c}\right)^2 = k^2, \tag{4.16}$$

which for different signs of the permittivities is plotted in Fig. 4.1. In practice, deep-subwavelength periodicity and anisotropy are jointly employed in order to produce effective negative permitivities for light, and in turn produce effective negative refractive indices when homogenized over larger length scales [326]. For $\epsilon_\parallel \epsilon_\perp < 0$, one obtains a hyperbola for the isofrequency surfaces, hence the phrasing ‘hyperbolic medium’. The realistic finite-size dispersion is seen in the periodic termination at the edge of the BZ, similar to that observed in the tight-binding model in Fig. 4.3. Crucially, the key distinction between the hyperbolic-like dispersions and the dispersions of the previous chapter is one of global topology; the ‘open’ nature of the dispersion has notable consequences on resonant emission into and wave propagation within the bath, as we now see. Taking the leading order approximation for the electromagnetic Green’s function due to extraordinary waves (including polarization) with $\epsilon_\perp < 0, \epsilon_\parallel > 0$, gives [10]

$$\mathbf{G}(\boldsymbol{\rho}, \Delta) = \frac{-ik^2 e^{ik\rho_e}}{\sqrt{|\epsilon_\perp|}\rho_e}\hat{\boldsymbol{\epsilon}}, \tag{4.17}$$

for the permittivity-induced effective ‘distance’

$$\rho_e = \sqrt{\boldsymbol{\rho} \cdot \hat{\boldsymbol{\epsilon}} \cdot \boldsymbol{\rho}}, \tag{4.18}$$

and

$$\hat{\boldsymbol{\epsilon}} = \epsilon_\perp \epsilon_\parallel \boldsymbol{\epsilon}^{-1}. \tag{4.19}$$

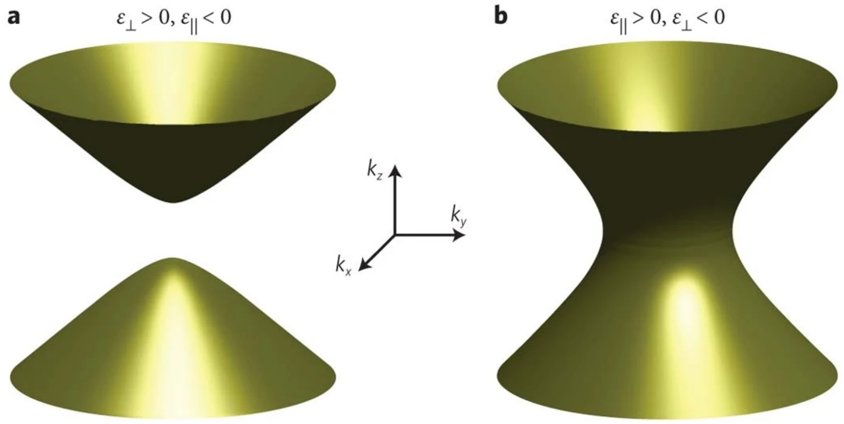

Figure 4.1: Constant-ω dispersion surfaces (4.16) for differing signs of permittivity. Taken from [9].

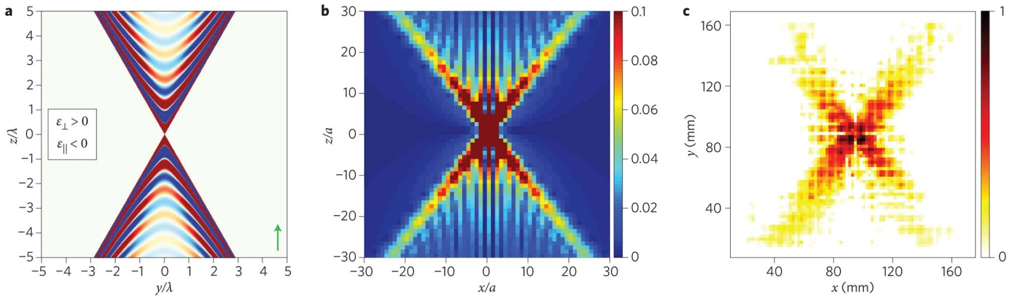

Figure 4.2: (a) Electric field amplitude for the emission of a dipole aligned along the z-axis [10]. (b) Green's function for a discrete lattice taking into account the discrete nature of a metamaterial [11]. (c) Experimental image of magnetic field in hyperbolic metamaterial constructed from a 2D transmission line [12].

We then see that beyond the cone defining $\rho_e = 0$, the Green's function changes from oscillating along rays to exponentially decaying, with the hyperbola (4.16) admitting the cone as asymptote. One sees an effective *light cone* for emission, which is shown in Fig. 4.2 as a drastic drop of the electric field amplitude outside of the light cone, whose boundary – the *caustics* – are determined as the rays whose angle θ with the x-y plane is the solution to $\epsilon_{\|} \sin^2\theta + \epsilon_{\perp} \cos^2\theta = 0$.

On the caustic itself, the field intensity and the Green's function (4.17) see a divergence, which is associated with a diverging decay length

$$l_{\text{eff}} = \left(k\sqrt{\hat{\boldsymbol{\rho}} \cdot \hat{\boldsymbol{\epsilon}} \cdot \hat{\boldsymbol{\rho}}}\right)^{-1}, \tag{4.20}$$

for the field for $\hat{\boldsymbol{\rho}} = \boldsymbol{\rho}/\rho$ almost oriented along the caustic [55]. I note, as referenced earlier, that the diverging volume of the isofrequency surface corresponds to a divergence in the imaginary part of the self-Green's function – the density of states [9] – which in turn gives an diverging Purcell factor in continuum media.

4.3.2 Hyperbolic-like dispersion in the tight-binding lattice - Section IV of [5]

Starting from the square tight-binding model (4.1) and setting $J_y = 2J_x = 2J$ yields the hyperbolic-like dispersion shown in Fig. 4.3. Note that in the tight-binding model a hyperbolic dispersion may also be obtained simply by inducing anistropy, in contrast to the complex schemes required in dielectrics to induce negative permitivities. Choosing $\Delta = -J$, no such $\mathbf{k}_0$ satisfying (4.14) is available for a range of $\boldsymbol{\rho}$, specifically such that the set

$$\{\mathbf{v}(\mathbf{k}) \text{ with } \mathbf{k} \text{ in } S(\Delta)\}, \tag{4.21}$$

contains no vector proportional to $\boldsymbol{\rho}$. In this case, the most 'extremal' group velocity vector defining the boundaries of the light cone can be seen to lie at the point $\mathbf{k}_\infty$ such that

$$|\mathbf{m}(\mathbf{k}_\infty)| \to \infty, \tag{4.22}$$

which is denoted as the white dot in Fig. 4.3(a). That is, the caustics are defined by wavepackets of diverging effective mass and correspond to zero-curvature points on the isosurface, which result in the longer range interactions on the caustic. Specifically, degenerate stationary-phase arguments [323] predict a power-law decay due to infinitely massive excitations of $\rho^{-1/3}$ on the caustic, in contrast to the $\rho^{-1/2}$ decay observed strictly within the light-cone. Beyond the caustic, the principle of non-stationary phase [323] applied to (4.13) dictates a decay of Γ faster than any polynomial, whilst extra calculations show this to be the case for Ω also [5, 287]. Hence, one observes a drastic drop in emission along the x-axis in Fig. 4.2, corresponding to exponentially decaying tails of evanescent waves. For comparison the continuum limit of $\frac{\Delta}{J}, ka \to 0$ ($k = |\mathbf{k}|$) yields effectively homogenous media [10, 56], where the Green's function is [327]

$$G(\boldsymbol{\rho}, \Delta) \approx \frac{1}{4}\sqrt{\left|\frac{J_y}{J_x}\right|} H_0^{(1)}\left(\frac{1}{a}\sqrt{\boldsymbol{\rho}\cdot\boldsymbol{\sigma}\cdot\boldsymbol{\rho}}\right) = \frac{1}{4}\sqrt{\left|\frac{J_y}{J_x}\right|} H_0^{(1)}\left(\frac{\rho}{a}\sqrt{\hat{\boldsymbol{\rho}}\cdot\boldsymbol{\sigma}\cdot\hat{\boldsymbol{\rho}}}\right), \tag{4.23}$$

for some real amplitude A, where

$$\boldsymbol{\sigma} = \begin{bmatrix} \sigma_x & 0 \\ 0 & \sigma_y, \end{bmatrix} = \begin{bmatrix} \frac{\Delta}{J_x} & 0 \\ 0 & \frac{\Delta}{J_y}, \end{bmatrix} \tag{4.24}$$

is an anisotropy tensor and $\hat{\boldsymbol{\rho}} = \boldsymbol{\rho}/\rho$. Eq. (4.23) plays the role of the Green's function (4.9) for hyperbolic media in a scalar and 2D baths. Similarly to previously, when $\sigma_x\sigma_y < 0$, the equation $\sigma_x\rho_x^2 + \sigma_y\rho_y^2 = 0$ determines the caustics, beyond which purely real exponential decay is observed. Fixing $\hat{\rho}_y/\hat{\rho}_x$ gives an effective decay length as in (4.20), but where $\boldsymbol{\sigma}$ plays the role of $\hat{\boldsymbol{\epsilon}}$. Specifically, κ approaches 0 as $\kappa \sim \sqrt{\tilde{\theta}}$, where $\sqrt{\tilde{\theta}}$ is the angle between the caustic and $\boldsymbol{\rho}$. However, there are notable distinctions between the observations of the continuum model and the discrete model, whose behaviour is summed up in Fig. 4.3: in (b) and (c) one observes the exponential decay of the magnitude of Green's function elements along the rays lying outside the caustics, with the decay length $1/\kappa$ diverging near the caustic. In contrast to the divergence predicted by (4.23), a divergence of $1/\kappa$ happens in the sense that a profile $|G| \sim \exp(-\kappa\rho)$ is no longer valid, as at the caustic finite Green's function elements with decay $\propto \rho^{-1/3}$ are observed in contrast to the divergence in the continuum. Within the light cone $\propto \rho^{-1/2}$ as mentioned in (4.15). I also note that in the discrete case $\kappa \sim \tilde{\theta}^{3/2}$ near the caustic, in contrast to $\kappa \sim \sqrt{\tilde{\theta}}$ of the continuum case; this can be attributed to the existence of finite $\mathbf{k}$ with $\mathbf{v}(\mathbf{k})$ proportional to the caustic, in contrast to the continuum case where such $\mathbf{v}(\mathbf{k})$ only asymptotically approaches the caustic line. In Fig. 4.3(e) the analytical prediction of this scaling law is compared with the κ obtained by fitting the 2D evanescent wave profile

$$\frac{\exp(-\alpha\tilde{\theta}^{3/2}\rho)}{\rho^{1/2}}, \tag{4.25}$$

to the exact numerically obtained magnitude of the Green's function, where α is determined by higher-order derivatives of ω at $\mathbf{k}_\infty$. A final and key feature of system dynamics may be found in Fig. 4.3(d), where the ratio of real and imaginary parts of the Green's function are observed. Approximately outside of the light cone, Ω drops by orders of magnitude relative to Γ, so that G is almost purely imaginary there. A clearer comparison is given in the inset of (c), when travelling along the ray $y = 0$, one observes an exponential decay of Γ, which itself is orders of magnitude larger than Ω is the vicinity of zero separation. This finding is one of the main results of [5], as to my knowledge exponentially decaying and incoherent interactions between emitters are seldom discussed in the literature (see below).

As Γ drops off exponentially, one can then construct purely dissipative interactions corresponding to incoherent short-range spin flips in the effective non-Hermitian Hamiltonian. For example, coupling a chain of spins to the x-axis of the lattice, one approximately obtains the dissipator acting effectively only on nearest neighbors in the Born-Markov approximation

$$\mathcal{L}[\rho] = \frac{\Gamma}{2}\sum_{jk}\frac{\exp(-\alpha|j-k|)}{|i-j|^{1/2}}\left([\sigma_k\rho, \sigma_j^+] + [\sigma_k, \rho\sigma_j^+]\right). \tag{4.26}$$

This is in contrast to the standard exponentially decaying *coherent* coupling (recall Eq. (1.26)) typically observed for emitters resonant outside of a band [91, 91, 105, 320], and the incoherent contribution from travelling (Hankel) waves that typically decay as a power law. Assuming a small decay-length, one may then approximate the above via nearest-neighbor interactions (care should be taken to ensure positive-definiteness). (Driven-)dissipative spin systems are a recent topic of focus [328, 329, 330], but short-range dissipative interactions of this form have not yet been studied to my knowledge. As an opposite limit to all-to-all cavity interactions (excluding the trivial single-body emission case), such models could shed further light on the nature of many-body dissipative quantum dynamics. Given the flexibility of light-matter systems, the above dissipator could also be engineered in conjunction with driving in order to extend to analysis on driven-dissipative systems.

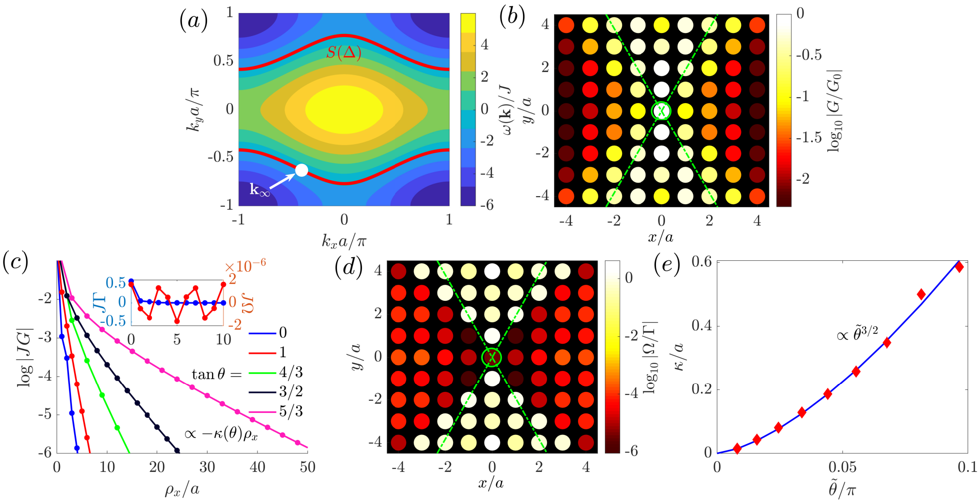

Figure 4.3: (a) Dispersion relation for $J_y = 2J_x = 2J$, with $\Delta = -J$. The white dot $\mathbf{k}_\infty$ denotes the line's inflection point with $\frac{|\mathbf{m}(\mathbf{k}_\infty)|}{\mathbf{v}(\mathbf{k}_\infty)\cdot\mathbf{m}(\mathbf{k}_\infty)\cdot\mathbf{v}(\mathbf{k}_\infty)} \to \infty$, where $\mathbf{v}(\mathbf{k}_\infty)$ gives one of the caustic vectors (see (b)), upon which symmetry then gives the other. (b) Magnitude of the ratio of the Green's function (omitting the frequency argument) $G(\mathbf{0}, \boldsymbol{\rho})$ to $G_0 = G(\mathbf{0}, \mathbf{0})$ on a log scale, where each dot denotes a lattice site. Dash-dotted green lines denote the caustics, given as the group velocity vector $\mathbf{v}(\mathbf{k}_\infty)$ and its mirror image in the BZ. (c) $\log|JG|$ for varying $\tan\theta = \rho_y/\rho_x$. For reference, $\arg[\mathbf{v}(\mathbf{k}_\infty)] \approx 1.92$. Inset: $J\Omega$, $J\Gamma$ for $\theta = 0$. (d) Ratio between $|\Omega|$ and $|\Gamma|$ on a log scale. (e) Dimensionless inverse decay length κ/a of Γ beyond the caustic. The diamonds (the solid line) give the value through exact calculation of the Green's function (obtained by fitting to (4.25)). Taken from [5].

4.4 Artificial gauge fields for bosons

One challenge faced at first glance by quantum optical systems for structured baths is that the neutral system excitations (phonons and photons) lack a net charge, in contrast to electrons in the solid-state. In addition to forming a central component in many working devices such as accelerators and microscopes, the interaction of charged particles with electromagnetic fields gives rise to the celebrated quantum Hall effect [331], which has notable implications in both theoretical and applied topological physics; clean and highly tunable simulators of such systems would therefore be ideal. In the tight-binding lattice picture, a magnetic field is manifest as a Peierl's phase accumulated along with hopping:

$$J_{jk}\hat{a}_j^\dagger\hat{a}_k \to J_{jk}e^{i\phi_{jk}}\hat{a}_j^\dagger\hat{a}_k, \tag{4.27}$$

for

$$\phi_{jk} = \int_{\mathbf{r}_j}^{\mathbf{r}_k} \mathbf{A}(\mathbf{r}) \cdot d\mathbf{r}, \tag{4.28}$$

given a gauge field $\mathbf{A}(\mathbf{r})$, corresponding to the magnetic field $\mathbf{B}(\mathbf{r}) = \nabla \times \mathbf{A}(\mathbf{r})$. The potential $\mathbf{A}$ is unique up to $\mathbf{A} \to \mathbf{A} + \nabla\chi$ for arbitrary χ, and so the total phase $\Phi = \sum_{\square} \phi_{jk}$ accumulated over hopping around the plaquette $\square$ is uniquely defined. In order to circumvent a lack of charge, novel proposals for generating the Peierls phase by periodically modulating the lattice couplings J_{jk} [306, 307], or through generation of a relative phase between two internal states [308] have been made. These phases can also be applied in conjunction with anisotropy in the hopping parameters, which brings us to the current investigation.

4.4.1 Emission into magnetic baths - Section V of [5]

In the following section I introduce an artifical gauge field onto the square lattice exhibiting anisotropic couplings. The analysis is carried out in 2D, but similar conclusions can be made in higher dimensions. To the best of my knowledge at the time this work was carried out, the analytical and computational analysis of the Green's function was impractical in this regime due to the splitting into (a possibly infinite) number of sub-bands. Since then I have become aware of [332], which in principle allows one to readily calculate the Green's function including artifical gauge fields. Hence, I here resort to semiclassical arguments concerning the trajectory of wavepackets, along with real-time simulation of emission for one or more emitters coupled to the bath. As discussed earlier, the effect of an artifical gauge field on the tight-binding lattice is to include a complex hopping phase. In free space, the dispersion relation is isotropic, and from the continuum limit of the lattice model with equal x and y couplings, for example, one may reproduce the standard Landau orbits [13, 333] of electrons in a magnetic field. In the spirit of the lattice length scale becoming small, one may instead consider the semiclassical equations of motion for a wavepacket localized around $\mathbf{k}_0$ in momentum space, whose spatial extent far exceeds a single lattice site. The square lattice does not exhibit Berry curvature, and so the semiclassical equations of motion for the wavepacket are dependent purely on the isofrequency contour and the real-space magnetic field

$$\dot{\mathbf{r}} = \mathbf{v}(\mathbf{k}), \tag{4.29}$$

$$\dot{\mathbf{k}} = -\mathbf{v}(\mathbf{k}) \times \mathbf{B}. \tag{4.30}$$

Taking the case of the magnetic field pointing out of the lattice, $\mathbf{B} = \frac{\Phi}{a^2}\hat{\mathbf{z}}$, one sees from (4.29) that the wavevector simply traces out the isosurface that contains $\mathbf{k}_0$, and from there the wavepacket evolution in position space is determined. The wavepacket evolution is then confined to a closed loop, or to a semi-infinite trajectory depending on whether S is open (an *open orbit*) or closed (a *closed orbit*). In the case of the open orbit, one finds the characteristic length and temporal periods

$$\mathbf{l} = \int d\mathbf{r} = \tfrac{1}{B}\int_S \tfrac{d\mathbf{k}\mathbf{v}(\mathbf{k})}{v(\mathbf{k})} = \tfrac{\hat{\mathbf{a}}_y}{\alpha}, \tag{4.31}$$

$$\tau = \int dt = \tfrac{1}{B}\int_S \tfrac{d\mathbf{k}}{v(\mathbf{k})} = \tfrac{\Gamma}{2\alpha}, \tag{4.32}$$

for the flux

$$\alpha = \frac{\Phi}{2\pi}, \tag{4.33}$$

and where Γ is the imaginary part of the self-Green's function element for a single emitter. Viewing resonant emission as approximately a transfer of excitation into a sum of wavepackets lying on S then suggests that full emission profile itself should have the characteristic length and time scales of (4.31). As the emitter enforces an initially localized excitation, one should expect to see re-localization of the emission profile at each spatial period also, up to evanescent waves. Indeed, this effect is witnessed in the excitation profiles given in Fig. 4.4(a,b): after a time $n\tau = \frac{n\Gamma}{2\alpha}$ one sees the complete formation of n spatial periods with length $l = a/\alpha = 100a$. Particularly of note is the fidelity of the refocussing – in (c) a cross-section of the lattice is presented along the x-axis (where the emitter lies), and at (x, l) (after one spatial period). Any exponential tails due to evanescent fields present at $y = 0$ are almost completely non-existent by $y = l$, where one sees that the lattice population at $t = 6\tau$ is effectively negligible at all but the central 'refocussing' site at $(0, l)$, corresponding to the initial single-site-localization originating from the emitter. It is worth noting that once the magnetic field strength α is fixed, the spatial period is only dependent on the lattice vector, whilst the single-site resolution refocussing is in principle preserved for arbitrary system parameters that result in periodic orbits. In general, when band transitions and Berry curvature can be neglected these statements should hold for arbitrary lattices, whilst the specific profile of the emission pattern will be determined by the microscopic particulars. As one varies the emitter detuning Δ, the period will remain constant until becoming ill defined at $\Delta = \pm 2J$, where S crosses the van-Hove singularities $(k_x, k_y) = (0, \pm\pi/a), (\pm\pi/a, 0)$ (see Fig. 4.3(a)) – at this point $\Gamma \to \infty$ and a topological transition of the dispersion relation is observed, with the open orbit discontinuously deformed into a closed orbit, reproducing again Landau levels for emission. The quasi-1D emission can then be said to be topologically robust *with respect to the dispersion relation* $\omega(\mathbf{k})$. This is in contrast to the standard topology of the literature where topologies of the system can be determined by the Bloch wavefunction, with two distinct topologies possible for identical dispersion relations [292, 334, 335]. The transition corresponding to dispersion was observed in polaritons in hyperbolic materials in a work published shortly after the initial submission of my own [336], albeit without an effective magnetic field. In the present discussion, the topological nature of 1D emission naturally affords robustness to scattering from local perturbations, where beyond the near-field, scattered fields are again confined by local gauge constraints to travel in one dimension. In addition, weak global perturbations (such as random disorder producing a distribution of bosonic frequencies) that do not appreciably couple the emitter to waves beyond the Van-Hove singularity also do not destroy the (average) quasi-1D transport in the system. A

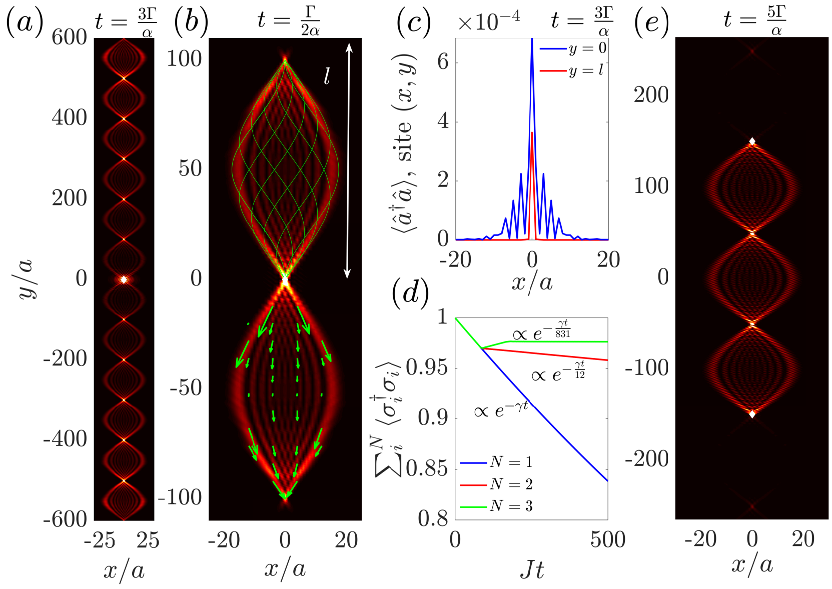

Figure 4.4: Emission into the magnetic bath 111 (1201) sites across in the $x(y)$ direction. $J_y = 2J_x = 2J$ and $\Delta = -J$, with $\alpha = 0.01$. In (a-c), $g = 0.1J$, and in (d-e), $g = 0.025J$. (a) Bath population at $t = 6\tau$ for an emitter prepared in the excited state, and located at the central white diamond. (b) Bath population at $t = \tau$. Green lines give semiclassical trajectories evolving from the emitter with $\mathbf{k}$ sampled from S. Arrows correspond to photonic current [13]. (c) Bath population along the x axis when $y = 0, l$. (d) Total emitter population for one, two, and three emitters, each separated by $3l$. The two-atom (three atom) subradiant state Eq. (4.34) (Eq. (4.35)) is prepared. (e) Bath population at $t = 10\tau$ for two emitters separated a distance $3l$ and prepared as in (d). Taken from [5].

summary of this behaviour is contained in Fig. 4.5. Perhaps the most remarkable feature is observed in (c-f): even for moderate spread χJ of the bosonic frequency on the order of the x-hopping strength J, the 'focussing' of emission is well retained on average. One may also examine the bosonic populations on a bath cross-section $(x, 2l)$ (for free x) after a time of 3τ, as in Fig. 4.4(c). The central 'refocussing' site sees average population orders of magnitude large than its immediate neighbors, even beyond a standard deviation of the neighboring populations.

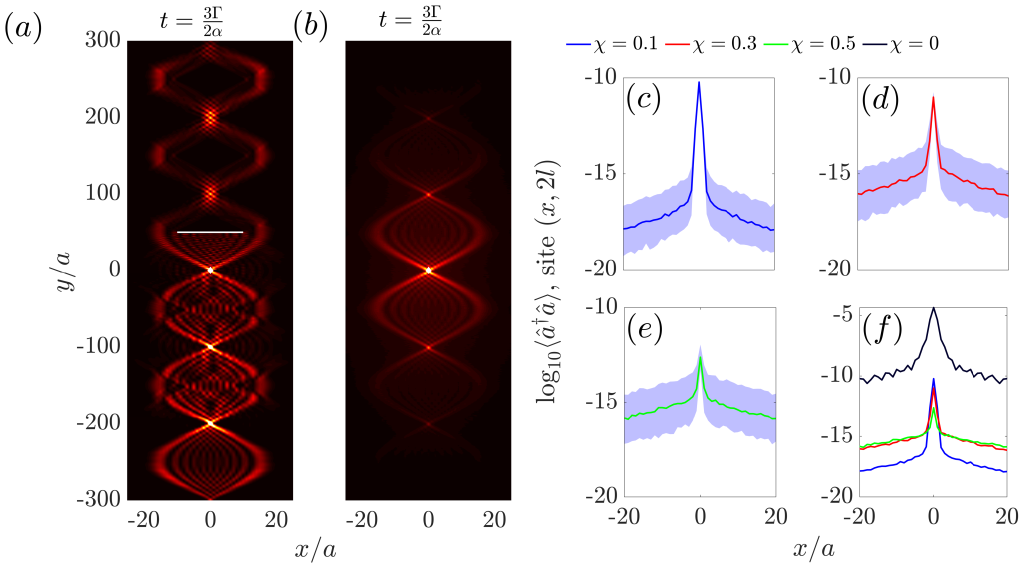

Figure 4.5: Parameters are as in Figure 4.4 with $g = 0.025J$. (a) Bath population at $t = 3\tau$ in the presence of an obstruction (white line) at $y = l/2, x \in [-10a, 10a]$ obtained by decoupling all obstruction sites from the lattice. (b) Averaged bath population at time $t = 3\tau$ for disorder $\chi = 0.5$. (c-f) Average log-populations for the cross-section $y = 2l$ in the presence of varying disorder parameter χ. The solid lines give the average whilst the shadow denotes a standard deviation. In (f) the population in the presence of no disorder corresponding to Figure 4.4(a) is shown for comparison. Taken from [5].

The robust refocussing capability of emission in the hyperbolic and magnetic bath lends credibility to a final application that I now present. Recall that the coupling of an emitter to a photon is dependent upon the ratio of the emitter cross-section to the photon 'area'. In the current investigation, a situation akin to a quasi-1D system occurs where waves resonant with the emitter are confined to travel in one dimension, and thus the emitter-field coupling will depend on the transverse extent of the field relative to that (single-site-extent) of the emitter. Notably, at the refocussing point the travelling wave is almost localized down to the single site (see Fig. 4.4), identical to the spatial extent of the emitter. Neglecting the exponential tails away from the central focussing point, this means that an emitter placed at the refocussing point should have a near unity probability to interact with the incoming wave, creating an almost ideal 1D waveguide QED scenario, where the atoms can act as perfect mirrors [7, 59] – in particular, perfectly superradiant and subradiant states should be possible. In [5], I consider the case of multiple emitters coupled to the bath, placed at integer multiples of the characteristic length apart from one another. Although imperfect, the emitters form an approximate bound state in the continuum [337], where the photon is localized between the two emitters, which themselves exist in the (approximately) subradiant state

$$|\psi\rangle \propto \frac{1}{\sqrt{2}}\left(\hat{\sigma}_1^+ - \hat{\sigma}_2^+\right)|0\rangle\,, \tag{4.34}$$

for the system vacuum state $|0\rangle$. As mentioned, the sites around the refocussing points are populated (albiet almost vanishingly), meaning that there is a transmission of the photon simply associated with the photon at these sites not interacting with the emitter. Placing additional emitters at further refocussing points along the unperturbed emission trajectory then allows one to interface with the remaining component of the photon, enhancing the fidelity of the subradiant state for each extra emitter. I present the results in Fig. 4.4(d) for one, two, and three emitters. After an initial delay associated with photonic propagation [337], the bound state in the continuum is formed for 2 and 3 emitters, with the single emitter decay rate γ being cut by approximately a factor of 10 for each extra emitter. For reference, the three emitter subradiant state is given as

$$|\psi_3\rangle \propto \frac{1}{\sqrt{6}}\left(\sigma_1^+ - 2\sigma_2^+ + \sigma_3^+\right)|0\rangle \,. \tag{4.35}$$

4.5 Publication [5]: Green's functions of and emission into discrete anisotropic and hyperbolic baths

Many of the results of this chapter are published in [5] as

Green's functions of and emission into discrete anisotropic and hyperbolic baths
L Ruks, T Busch
Physical Review Research **4** (2), 023044 (2022)

I conceived of and initiated the project, carried out all analytical calculations and numerical simulations, and wrote the manuscript. All authors contributed to the final interpretation of results and writing of the final version.

4.6 Outlook

4.6.1 Experimental considerations

The tight-binding model realising hyperbolic dispersion in a discrete lattice is experimentally feasible in metamaterial-based transmission lines [12, 291, 338], and coupled cavity-type systems in superconducting circuits [290, 292] operating at microwave frequencies, in addition to the approximate realisations as the lowest band in optical lattices [19] and photonic crystals [60], and natural hyperbolic media [55]. On the other hand, the artifical gauge field can be realised in coupled microwave [298] and optical resonators [339], and even using cold atoms as an effective waveguide (in the single photon regime) [340]. At present, realisation of qubit coupling and artificial gauges fields is ideal in the microwave regime. Whilst current realisations of quantum emitters coupled to magnetic baths (with the possibility for distinct coupling strengths) exist in 1D [292], the realisation of qubits within 2D bosonic lattices should also be possible using current state-of-the-art in superconducting qubit circuits [341], with integration of emitters into 2D array of microwave cavities [313] and into coupled topological arrays of resonators [342, 343] the most promising paths. As an example, we consider a setup similar to [298] consisting of a lattice of microwave cavities that in principle support coupling to transmon qubits, and refer to experimentally realisable parameters cited in the supplemental material of [13], where a similar consideration was made. The bosonic frequency ranges from $\omega_c \sim 0.1 - 10$ GHz with a near-negligible broadening of $\Delta\omega_c \sim \pm 1$ Mhz and quality factor $Q \sim 10^3 - 10^5$ corresponding to possible decay rates of $\gamma_c \sim 5 \times 10^{-2}$-1 MHz, whilst the transmon qubits have frequencies of $\omega_0 \sim 3 - 5$ GHz (and can be tuned over ranges of $\delta\omega_0 \sim 100$ MHz) with decay into other channels $\gamma_0 \sim 1$ KHz. The spin-boson coupling can take values $g \sim 1 - 100$ MHz. Hoppings can be tuned between $J \sim 20 - 100$ MHz, with deviations of about $\Delta J \sim 1$ MHz. Additionally, whilst equal couplings in the x- and y- directions are chosen in [298], the evanescent coupling between the cavities should in principle be adjustable via the physical dimensional of the cavity setup, inducing anisotropy and weaker coupling in (say) the x- direction. The final consideration lies in the flux α: in [313], α takes distinct values $\alpha = 1/4, 1/6$. Here, whilst the periodic quasi-1D emission will remain, the validity of the semiclassical approximation is not as clear. Nonetheless, in similar setups the option of tuning α freely is available [311]. One then chooses the parameters so that the magnetic temporal period is much less than the decay corresponding to the boson/spin decay

$$\tau \ll 1/\gamma_e, 1/\gamma_0. \tag{4.36}$$

Approximating the emitter decay rate into the non-magnetic bath as $\gamma \sim \frac{g^2}{J}$ with Green's function element $\Gamma \sim J^{-1}$, one arrives at reasonable parameters producing a detuning $\Delta = \omega_0 - \omega_c \sim -J$ given by

$$\begin{gathered}\omega_c = 5.1 \times 10^3 \text{ MHz}, \gamma_c = 5 \times 10^{-2} \text{ MHz},\ \omega_0 = 5 \times 10^3 \text{ MHz}, \\ \gamma_0 = 5 \times 10^{-2} \text{ MHz}, \alpha = 1/50,\ J = 100 \text{ MHz},\ g = 5 \text{ MHz}, \\ \tau^{-1} = \frac{2\alpha}{\Gamma} = 4 \text{ MHz}, \gamma = 0.25 \text{ MHz}.\end{gathered} \tag{4.37}$$

That is, both the emitter timescale γ and the magnetic period τ^{-1} are at least an order of magnitude greater than the associated decay frequencies γ_c, γ_0, and so the dynamics should be observable whilst remaining in the semiclassical regime ($\alpha \ll 1$) and Markovian regime ($g \ll J$.) As in this case the hopping deviations saitsfy $\Delta J/J \sim 1/100$, the fluctuations in hopping strengths should not be too detrimental to observing dynamics.

4.6.2 Conclusions and continuations

One of the main results of this work was to shed light on the emitter-emitter interactions that can be mediated by lattices with hyperbolic-like dispersion when using a toy tight-binding model where the discrete nature of the lattice is taken into account and salient dynamics can be deduced. In addition to analytic derivations regarding emission into a discrete bath featuring hyperbolic-like dispersion, the notable finding was that directionally-tunable exponentially decaying interactions that are dominantly disspative can be realised in this regime. When considered in the context of the corresponding spin models, these incoherent terms translate into purely dissipative and exponentially decaying interactions. Dissipative interactions are usually associated with travelling waves generating long-range power-law-type interactions, and exponentially decaying kernel represents an unconventional medium between typical long-range collective dissipation and individual decay. Theoretical investigations on driven-dissipative systems experiencing this short-range collective dissipation may be fruitful in order to pin down the role of incoherent dynamics in quantum spin systems. In addition, my results shed further light on hyperbolic materials as a medium for engineering emitter-emitter interactions for spin models, and it could be fruitful to explore how dynamics might be realised in the full three dimensional material with polarization effects included.

The other main result of the work was the exploration of emission into a magnetic bath exhibiting hyperbolic dispersion. The results represent a departure from the studies of closed Landau orbits [13], but reveal alternative methods for transporting photons and shaping emitter-emitter interactions in higher-dimensional media, with a novel application in the ‘atomic mirror’-based cavity [7, 59]. In addition, my results highlight the role of topological transitions with respect to dispersion, where discontinuous changes in topology of isosurfaces fundamentally alters emission dynamics. From here one might try to devise a 3D tight-binding mode exhibiting traditional topological phases recreating those discovered in the full 3D metamaterials [344], whilst one could also explore applications in polaritonic 2D materials following the recent high profile experimental realisation of polaritons in hyperbolic metamaterials [336].

Conclusion

In this thesis, I have studied wave propagation in continuum and discrete media, together with its implications when coupled to quantum emitters in studies of the dispersion potential and the Dicke model of cavity QED. I have systematically studied the travelling waves of coupled optical nanofibers, and complemented the studies with an investigation of the two-body ground-state dispersion potential between two atoms situated next to a nanoscale cylinder. In the setting of cavity QED, I have provided key analysis of out-of-equilibrium dynamics in the Dicke model in order to support the concept of quenches in critical quantum systems for metrological protocols. Finally, I have analysed wave propagation and emission in discrete hyperbolic media, with the unconventional inclusion of artifical gauge fields on the lattice. My work has resulted in 5 peer-reviewed publications. Brief summaries of the chapters and works contained within are given below.

4.7 Optical Nanofibers For Light-Matter interfaces

I have investigated the travelling waves of a system consisting of two parallel nanofibers, using the approximate coupled mode theory and an exact eigenmode expansion. The former provides a realistic characterisation of power coupling between two fibers for existing experimental parameters, moving beyond approximations typically employed in the literature. The latter explores and highlights when the approximate mode theory can break down, and in particular sheds light on the strongly hybridized electric field profiles of two coupled fibers; the insights have lead to further extensions with the inclusion of quantum emitters, leading to theoretical observation of high coupling into guided modes, and improved atomic traps, in the two-fiber system. I have, in addition, investigated the ground-state dispersion potential between two cold atoms situated next to an optical nanofiber, and found that the fiber-induced anisotropy in conjunction with a preference for the atomic dipole may enhance or diminish the interaction potential by orders of magnitude with respect to free space. Whilst the results of the publication were obtained in the context of a nanoscale cylinder where the effect is too weak to be measured, they may be experimentally measurable in transmission lines. The works have been published in *New Journal of Physics* 22.12 (2020): 123007; *New Journal of Physics* 23.4 (2021): 043006; *Applied Physics B* 125.11 (2019): 1-7.

4.8 Quenches Across a Phase Transition in Quantum Metrology

I have analytically derived the full out-of-equilibrium dynamics of the linear bosonic Hamiltonian effectively approximating the Dicke model, and used the results to calculate the classical Fisher information corresponding to a quadrature measurement following a quench of the Dicke model into the superradiant regime. My results have shown that a quadrature measurement may be optimal in the superradiant phase of the Dicke model, and they have been applied to show that an exponentially growing and optimal Fisher information can be obtained following a quench through a critical point. This offers a possible alternative to standard critical quantum metrology for high-precision sensing. The results are published in *Quantum* 6 (2022): 700.

4.9 Wave Propagation and Emission in Discrete Baths Exhibiting Hyperbolic Dispersion

In this finally study I have investigated the Green's function of a discrete lattice exhibiting hyperbolic-like dispersion, and explored the consequences when emitters are coupled to the bath in the Born-Markov approximation. I have investigated the Green's function beyond the usually studied light-cone in the anisotropic square lattice. Here I found exponentially decaying and dominantly dissipative interactions that can be used for engineering unconventional spin models with a high tunability through the relative orientation of the emitters. I further considered the inclusion of an artifical gauge field on the lattice, which to the best of my knowledge is currently unexplored in the literature when considered in conjunction with a hyperbolic-like dispersion. Here I have found topologically protected quasi-1D emission into higher-dimensional baths, which resulted in the formation of quasi-1D dark states formed between two or more emitters coupled to the lattice. My results offer new methods for transporting and storing photons in linear media and open up the class of effective spin models available to quantum emitters coupled through structured media. This work has been published in *Physical Review Research* 4.2 (2022): 023044.

Bibliography

[1] Fam Le Kien, Lewis Ruks, Síle Nic Chormaic, and Thomas Busch. Coupling between guided modes of two parallel nanofibers. *New Journal of Physics*, 22 (12):123007, 2020.

[2] Fam Le Kien, Lewis Ruks, Síle Nic Chormaic, and Thomas Busch. Spatial distributions of the fields in guided normal modes of two coupled parallel optical nanofibers. *New Journal of Physics*, 23(4):043006, 2021.

[3] Fam Le Kien, Lewis Ruks, and Thomas Busch. Waveguide-induced dispersion interaction between two two-level atoms with orthogonal in-transverse-plane dipoles. *Applied Physics B*, 125(11):1–7, 2019.

[4] Karol Gietka, Lewis Ruks, and Thomas Busch. Understanding and improving critical metrology. quenching superradiant light-matter systems beyond the critical point. *Quantum*, 6:700, 2022.

[5] Lewis Ruks and Thomas Busch. Green's functions of and emission into discrete anisotropic and hyperbolic baths. *Physical Review Research*, 4(2):023044, 2022.

[6] Saman Jahani, Sangsik Kim, Jonathan Atkinson, Justin C Wirth, Farid Kalhor, Abdullah Al Noman, Ward D Newman, Prashant Shekhar, Kyunghun Han, Vien Van, et al. Controlling evanescent waves using silicon photonic all-dielectric metamaterials for dense integration. *Nature Communications*, 9(1):1–9, 2018.

[7] Darrick E Chang, L Jiang, AV Gorshkov, and HJ Kimble. Cavity QED with atomic mirrors. *New Journal of Physics*, 14(6):063003, 2012.

[8] Fam Le Kien, Thomas Busch, Viet Giang Truong, and Síle Nic Chormaic. Higher-order modes of vacuum-clad ultrathin optical fibers. *Physical Review A*, 96(2): 023835, 2017.

[9] Alexander Poddubny, Ivan Iorsh, Pavel Belov, and Yuri Kivshar. Hyperbolic metamaterials. *Nature Photonics*, 7(12):948–957, 2013.

[10] Andrey S Potemkin, Alexander N Poddubny, Pavel A Belov, and Yuri S Kivshar. Green function for hyperbolic media. *Physical Review A*, 86(2):023848, 2012.

[11] Alexander N Poddubny, Pavel A Belov, Pavel Ginzburg, Anatoly V Zayats, and Yuri S Kivshar. Microscopic model of Purcell enhancement in hyperbolic metamaterials. *Physical Review B*, 86(3):035148, 2012.

[12] Alyona V Chshelokova, Polina V Kapitanova, Alexander N Poddubny, Dmitry S Filonov, Alexey P Slobozhanyuk, Yuri S Kivshar, and Pavel A Belov. Hyperbolic transmission-line metamaterials. *Journal of Applied Physics*, 112(7):073116, 2012.

[13] Daniele De Bernardis, Ze-Pei Cian, Iacopo Carusotto, Mohammad Hafezi, and Peter Rabl. Light-matter interactions in synthetic magnetic fields: Landau-photon polaritons. *Physical Review Letters*, 126(10):103603, 2021.

[14] Cristiano MB Cordeiro, Marcos AR Franco, Giancarlo Chesini, Elaine CS Barretto, Richard Lwin, CH Brito Cruz, and Maryanne CJ Large. Microstructured-core optical fibre for evanescent sensing applications. *Optics Express*, 14(26): 13056–13066, 2006.

[15] Andrew D Ludlow, Martin M Boyd, Jun Ye, Ekkehard Peik, and Piet O Schmidt. Optical atomic clocks. *Reviews of Modern Physics*, 87(2):637, 2015.

[16] Allan W Snyder and John Love. *Optical waveguide theory.* Springer Science & Business Media, 2012.

[17] John D Joannopoulos, Steven G Johnson, Joshua N Winn, and Robert D Meade. Photonic crystals. In *Photonic Crystals.* Princeton university press, 2011.

[18] Philip Jones, Onofrio Maragó, and Giovanni Volpe. *Optical tweezers.* Cambridge University Press Cambridge, UK, 2015.

[19] Dieter Jaksch, Christoph Bruder, Juan Ignacio Cirac, Crispin W Gardiner, and Peter Zoller. Cold bosonic atoms in optical lattices. *Physical Review Letters*, 81 (15):3108, 1998.

[20] Roy J Glauber. Nobel lecture: One hundred years of light quanta. *Reviews of Modern Physics*, 78(4):1267, 2006.

[21] Crispin Gardiner, Peter Zoller, and Peter Zoller. *Quantum noise: a handbook of Markovian and non-Markovian quantum stochastic methods with applications to quantum optics.* Springer Science & Business Media, 2004.

[22] E Vetsch, D Reitz, G Sagué, R Schmidt, ST Dawkins, and A Rauschenbeutel. Optical interface created by laser-cooled atoms trapped in the evanescent field surrounding an optical nanofiber. *Physical Review Letters*, 104(20):203603, 2010.

[23] Takao Aoki, Barak Dayan, Elizabeth Wilcut, Warwick P Bowen, A Scott Parkins, TJ Kippenberg, KJ Vahala, and HJ Kimble. Observation of strong coupling between one atom and a monolithic microresonator. *Nature*, 443(7112):671–674, 2006.

[24] Itay Shomroni, Serge Rosenblum, Yulia Lovsky, Orel Bechler, Gabriel Guendelman, and Barak Dayan. All-optical routing of single photons by a one-atom switch controlled by a single photon. *Science*, 345(6199):903–906, 2014.

[25] Demetrios N Christodoulides, Falk Lederer, and Yaron Silberberg. Discretizing light behaviour in linear and nonlinear waveguide lattices. *Nature*, 424(6950): 817–823, 2003.

[26] DE Chang, JS Douglas, Alejandro González-Tudela, C-L Hung, and HJ Kimble. Colloquium: Quantum matter built from nanoscopic lattices of atoms and photons. *Reviews of Modern Physics*, 90(3):031002, 2018.

[27] Onur Hosten, Nils J Engelsen, Rajiv Krishnakumar, and Mark A Kasevich. Measurement noise 100 times lower than the quantum-projection limit using entangled atoms. *Nature*, 529(7587):505–508, 2016.

[28] James S Douglas, Hessam Habibian, C-L Hung, Alexey V Gorshkov, H Jeff Kimble, and Darrick E Chang. Quantum many-body models with cold atoms coupled to photonic crystals. *Nature Photonics*, 9(5):326–331, 2015.

[29] Jun Rui, David Wei, Antonio Rubio-Abadal, Simon Hollerith, Johannes Zeiher, Dan M Stamper-Kurn, Christian Gross, and Immanuel Bloch. A subradiant optical mirror formed by a single structured atomic layer. *Nature*, 583(7816): 369–374, 2020.

[30] Yuhang Li and Limin Tong. Mach-Zehnder interferometers assembled with optical microfibers or nanofibers. *Optics Letters*, 33(4):303–305, 2008.

[31] Wanvisa Talataisong, Rand Ismaeel, Timothy Lee, Martynas Beresna, and Gilberto Brambilla. Optical nanofiber coupler sensors operating in the cut-off wavelength region. *IEEE Sensors Journal*, 18(7):2782–2787, 2018.

[32] Chengjie Ding, Vivien Loo, Simon Pigeon, Romain Gautier, Maxime Joos, E Wu, Elisabeth Giacobino, Alberto Bramati, and Quentin Glorieux. Fabrication and characterization of optical nanofiber interferometer and resonator for the visible range. *New Journal of Physics*, 21(7):073060, 2019.

[33] Luqing Shao, Hao Wu, Wei Fang, and Limin Tong. Twin-nanofiber structure for a highly efficient single-photon collection. *Optics Express*, 30(6):9147–9155, 2022.

[34] Fam Le Kien, Sile Nic Chormaic, and Thomas Busch. Optical trap for an atom around the midpoint between two coupled identical parallel optical nanofibers. *Physical Review A*, 103(6):063106, 2021.

[35] Wenfang Li, Jinjin Du, and Síle Nic Chormaic. Tailoring a nanofiber for enhanced photon emission and coupling efficiency from single quantum emitters. *Optics Letters*, 43(8):1674–1677, 2018.

[36] Ralf Ritter, Nico Gruhler, Helge Dobbertin, Harald Kübler, Stefan Scheel, Wolfram Pernice, Tilman Pfau, and Robert Löw. Coupling thermal atomic vapor to slot waveguides. *Physical Review X*, 8(2):021032, 2018.

[37] A Goban, C-L Hung, JD Hood, S-P Yu, JA Muniz, O Painter, and HJ Kimble. Superradiance for atoms trapped along a photonic crystal waveguide. *Physical Review Letters*, 115(6):063601, 2015.

[38] Stefan Yoshi Buhmann and Dirk-Gunnar Welsch. Dispersion forces in macroscopic quantum electrodynamics. *Progress in Quantum Electronics*, 31(2):51–130, 2007.

[39] Harald R Haakh and Stefan Scheel. Modified and controllable dispersion interaction in a one-dimensional waveguide geometry. *Physical Review A*, 91(5):052707, 2015.

[40] Ho Trung Dung. Interatomic dispersion potential in a cylindrical system: Atoms being off axis. *Journal of Physics B: Atomic, Molecular and Optical Physics*, 49 (16):165502, 2016.

[41] Ephraim Shahmoon, Igor Mazets, and Gershon Kurizki. Giant vacuum forces via transmission lines. *Proceedings of the National Academy of Sciences*, 111 (29):10485–10490, 2014.

[42] Kimball A Milton, Prachi Parashar, Nima Pourtolami, and Iver Brevik. Casimir-Polder repulsion: Polarizable atoms, cylinders, spheres, and ellipsoids. *Physical Review D*, 85(2):025008, 2012.

[43] Kimball A Milton, EK Abalo, Prachi Parashar, Nima Pourtolami, Iver Brevik, and Simen Å Ellingsen. Repulsive Casimir and Casimir–Polder forces. *Journal of Physics A: Mathematical and Theoretical*, 45(37):374006, 2012.

[44] DP Craig and EA Power. The asymptotic Casimir-Polder potential for anisotropic molecules. *Chemical Physics Letters*, 3(4):195–196, 1969.

[45] Robert H Dicke. Coherence in spontaneous radiation processes. *Physical Review*, 93(1):99, 1954.

[46] Barry M Garraway. The Dicke model in quantum optics: Dicke model revisited. *Philosophical Transactions of the Royal Society A: Mathematical, Physical and Engineering Sciences*, 369(1939):1137–1155, 2011.

[47] Yaoming Chu, Shaoliang Zhang, Baiyi Yu, and Jianming Cai. Dynamic framework for criticality-enhanced quantum sensing. *Physical Review Letters*, 126(1): 010502, 2021.

[48] Louis Garbe, Obinna Abah, Simone Felicetti, and Ricardo Puebla. Critical quantum metrology with fully-connected models: from Heisenberg to Kibble–Zurek scaling. *Quantum Science and Technology*, 7(3):035010, 2022.

[49] Louis Garbe, Matteo Bina, Arne Keller, Matteo GA Paris, and Simone Felicetti. Critical quantum metrology with a finite-component quantum phase transition. *Physical Review Letters*, 124(12):120504, 2020.

[50] Alejandro González-Tudela and J Ignacio Cirac. Exotic quantum dynamics and purely long-range coherent interactions in Dirac conelike baths. *Physical Review A*, 97(4):043831, 2018.

[51] Iñaki García-Elcano, Alejandro González-Tudela, and Jorge Bravo-Abad. Tunable and robust long-range coherent interactions between quantum emitters mediated by Weyl bound states. *Physical Review Letters*, 125(16):163602, 2020.

[52] P Lambropoulos, Georgios M Nikolopoulos, Torben R Nielsen, and Søren Bay. Fundamental quantum optics in structured reservoirs. *Reports on Progress in Physics*, 63(4):455, 2000.

[53] Ana Asenjo-Garcia, JD Hood, DE Chang, and HJ Kimble. Atom-light interactions in quasi-one-dimensional nanostructures: A Green's-function perspective. *Physical Review A*, 95(3):033818, 2017.

[54] Yu Guo, Cristian L Cortes, Sean Molesky, and Zubin Jacob. Broadband super-Planckian thermal emission from hyperbolic metamaterials. *Applied Physics Letters*, 101(13):131106, 2012.

[55] Cristian L Cortes and Zubin Jacob. Super-Coulombic atom–atom interactions in hyperbolic media. *Nature Communications*, 8(1):1–8, 2017.

[56] Alena V Shchelokova, Alexander N Poddubny, and Pavel A Belov. Effects of discreteness in the Green's function of a hyperbolic medium. *Physical Review A*, 90(2):023854, 2014.

[57] Kejie Fang, Zongfu Yu, and Shanhui Fan. Realizing effective magnetic field for photons by controlling the phase of dynamic modulation. *Nature Photonics*, 6 (11):782–787, 2012.

[58] Jean Dalibard, Fabrice Gerbier, Gediminas Juzeliūnas, and Patrik Öhberg. Colloquium: Artificial gauge potentials for neutral atoms. *Reviews of Modern Physics*, 83(4):1523, 2011.

[59] Mohammad Mirhosseini, Eunjong Kim, Xueyue Zhang, Alp Sipahigil, Paul B Dieterle, Andrew J Keller, Ana Asenjo-Garcia, Darrick E Chang, and Oskar Painter. Cavity quantum electrodynamics with atom-like mirrors. *Nature*, 569 (7758):692–697, 2019.

[60] Jonathan David Hood. *Atom-light interactions in a photonic crystal waveguide.* PhD thesis, California Institute of Technology, 2017.

[61] CL Hung, SM Meenehan, DE Chang, O Painter, and HJ Kimble. Trapped atoms in one-dimensional photonic crystals. *New Journal of Physics*, 15(8):083026, 2013.

[62] Fam Le Kien, S Dutta Gupta, VI Balykin, and K Hakuta. Spontaneous emission of a cesium atom near a nanofiber: Efficient coupling of light to guided modes. *Physical Review A*, 72(3):032509, 2005.

[63] Alfredo M Morales and Charles M Lieber. A laser ablation method for the synthesis of crystalline semiconductor nanowires. *Science*, 279(5348):208–211, 1998.

[64] Limin Tong, Rafael R Gattass, Jonathan B Ashcom, Sailing He, Jingyi Lou, Mengyan Shen, Iva Maxwell, and Eric Mazur. Subwavelength-diameter silica wires for low-loss optical wave guiding. *Nature*, 426(6968):816–819, 2003.

[65] S-P Yu, JD Hood, JA Muniz, MJ Martin, Richard Norte, C-L Hung, Seán M Meenehan, Justin D Cohen, Oskar Painter, and HJ Kimble. Nanowire photonic crystal waveguides for single-atom trapping and strong light-matter interactions. *Applied Physics Letters*, 104(11):111103, 2014.

[66] VSC Manga Rao and Stephen Hughes. Single quantum-dot Purcell factor and β factor in a photonic crystal waveguide. *Physical Review B*, 75(20):205437, 2007.

[67] Janos Perczel, Johannes Borregaard, Darrick E Chang, Susanne F Yelin, and Mikhail D Lukin. Topological quantum optics using atomlike emitter arrays coupled to photonic crystals. *Physical Review Letters*, 124(8):083603, 2020.

[68] TE Northup and R Blatt. Quantum information transfer using photons. *Nature Photonics*, 8(5):356–363, 2014.

[69] H Jeff Kimble. The quantum internet. *Nature*, 453(7198):1023–1030, 2008.

[70] Yoshihiro Akahane, Takashi Asano, Bong-Shik Song, and Susumu Noda. High-Q photonic nanocavity in a two-dimensional photonic crystal. *Nature*, 425(6961): 944–947, 2003.

[71] Philippe Lalanne, Christophe Sauvan, and Jean Paul Hugonin. Photon confinement in photonic crystal nanocavities. *Laser & Photonics Reviews*, 2(6):514–526, 2008.

[72] Thomas Nieddu, Vandna Gokhroo, and Síle Nic Chormaic. Optical nanofibres and neutral atoms. *Journal of Optics*, 18(5):053001, 2016.

[73] Ramachandrarao Yalla, Mark Sadgrove, Kali P Nayak, and Kohzo Hakuta. Cavity quantum electrodynamics on a nanofiber using a composite photonic crystal cavity. *Physical Review Letters*, 113(14):143601, 2014.

[74] Andreas Angerer, Kirill Streltsov, Thomas Astner, Stefan Putz, Hitoshi Sumiya, Shinobu Onoda, Junichi Isoya, William J Munro, Kae Nemoto, Jörg Schmiedmayer, et al. Superradiant emission from colour centres in diamond. *Nature Physics*, 14(12):1168–1172, 2018.

[75] Tim Byrnes, Na Young Kim, and Yoshihisa Yamamoto. Exciton–polariton condensates. *Nature Physics*, 10(11):803–813, 2014.

[76] G Facchinetti and Janne Ruostekoski. Interaction of light with planar lattices of atoms: Reflection, transmission, and cooperative magnetometry. *Physical Review A*, 97(2):023833, 2018.

[77] Stefan Yoshi Buhmann. *Dispersion Forces I: Macroscopic quantum electrodynamics and ground-state Casimir, Casimir–Polder and van der Waals forces*, volume 247. Springer, 2013.

[78] Cole P Van Vlack. *Dyadic Green functions and their applications in classical and quantum nanophotonics.* Queen's University (Canada), 2012.

[79] Thomas Søndergaard and Bjarne Tromborg. General theory for spontaneous emission in active dielectric microstructures: Example of a fiber amplifier. *Physical Review A*, 64(3):033812, 2001.

[80] Stephen M Barnett, Bruno Huttner, Rodney Loudon, and Reza Matloob. Decay of excited atoms in absorbing dielectrics. *Journal of Physics B: Atomic, Molecular and Optical Physics*, 29(16):3763, 1996.

[81] Martijn Wubs, LG Suttorp, and Aart Lagendijk. Multiple-scattering approach to interatomic interactions and superradiance in inhomogeneous dielectrics. *Physical Review A*, 70(5):053823, 2004.

[82] Peijun Yao, VSC Manga Rao, and Stephen Hughes. On-chip single photon sources using planar photonic crystals and single quantum dots. *Laser & Photonics Reviews*, 4(4):499–516, 2010.

[83] DE Chang, K Sinha, JM Taylor, and HJ Kimble. Trapping atoms using nanoscale quantum vacuum forces. *Nature Communications*, 5(1):1–9, 2014.

[84] Fam Le Kien, DF Kornovan, Síle Nic Chormaic, and Thomas Busch. Repulsive Casimir-Polder potentials of low-lying excited states of a multilevel alkali-metal atom near an optical nanofiber. *Physical Review A*, 105(4):042817, 2022.

[85] DF Kornovan, AS Sheremet, and MI Petrov. Collective polaritonic modes in an array of two-level quantum emitters coupled to an optical nanofiber. *Physical Review B*, 94(24):245416, 2016.

[86] Peijun Yao, C Van Vlack, A Reza, M Patterson, MM Dignam, and Stephen Hughes. Ultrahigh Purcell factors and Lamb shifts in slow-light metamaterial waveguides. *Physical Review B*, 80(19):195106, 2009.

[87] Peter Lodahl, Sahand Mahmoodian, Søren Stobbe, Arno Rauschenbeutel, Philipp Schneeweiss, Jürgen Volz, Hannes Pichler, and Peter Zoller. Chiral quantum optics. *Nature*, 541(7638):473–480, 2017.

[88] Jan Petersen, Jürgen Volz, and Arno Rauschenbeutel. Chiral nanophotonic waveguide interface based on spin-orbit interaction of light. *Science*, 346(6205): 67–71, 2014.

[89] Hannes Pichler, Tomás Ramos, Andrew J Daley, and Peter Zoller. Quantum optics of chiral spin networks. *Physical Review A*, 91(4):042116, 2015.

[90] Tomás Ramos, Hannes Pichler, Andrew J Daley, and Peter Zoller. Quantum spin dimers from chiral dissipation in cold-atom chains. *Physical Review Letters*, 113 (23):237203, 2014.

[91] Sajeev John and Jian Wang. Quantum electrodynamics near a photonic band gap: Photon bound states and dressed atoms. *Physical Review Letters*, 64(20): 2418, 1990.

[92] Jonathan D Hood, Akihisa Goban, Ana Asenjo-Garcia, Mingwu Lu, Su-Peng Yu, Darrick E Chang, and HJ Kimble. Atom–atom interactions around the band edge of a photonic crystal waveguide. *Proceedings of the National Academy of Sciences*, 113(38):10507–10512, 2016.

[93] Alejandro González-Tudela, Vanessa Paulisch, HJ Kimble, and J Ignacio Cirac. Efficient multiphoton generation in waveguide quantum electrodynamics. *Physical Review Letters*, 118(21):213601, 2017.

[94] DE Chang, Jeffrey Douglas Thompson, H Park, V Vuletić, AS Zibrov, P Zoller, and MD Lukin. Trapping and manipulation of isolated atoms using nanoscale plasmonic structures. *Physical Review Letters*, 103(12):123004, 2009.

[95] Dmitry S Bykov, Shangran Xie, Richard Zeltner, Andrey Machnev, Gordon KL Wong, Tijmen G Euser, and Philip St J Russell. Long-range optical trapping and binding of microparticles in hollow-core photonic crystal fibre. *Light: Science & Applications*, 7(1):1–7, 2018.

[96] Darrick E Chang, J Ignacio Cirac, and H Jeff Kimble. Self-organization of atoms along a nanophotonic waveguide. *Physical Review Letters*, 110(11):113606, 2013.

[97] Paul Adrien Maurice Dirac. The quantum theory of the emission and absorption of radiation. *Proceedings of the Royal Society of London. Series A, Containing Papers of a Mathematical and Physical Character*, 114(767):243–265, 1927.

[98] Roy J Glauber and M Lewenstein. Quantum optics of dielectric media. *Physical Review A*, 43(1):467, 1991.

[99] Reza Matloob, Rodney Loudon, Stephen M Barnett, and John Jeffers. Electromagnetic field quantization in absorbing dielectrics. *Physical Review A*, 52(6): 4823, 1995.

[100] T Gruner and D-G Welsch. Green-function approach to the radiation-field quantization for homogeneous and inhomogeneous Kramers-Kronig dielectrics. *Physical Review A*, 53(3):1818, 1996.

[101] Stefan Scheel, Ludwig Knöll, and Dirk-Gunnar Welsch. QED commutation relations for inhomogeneous Kramers-Kronig dielectrics. *Physical Review A*, 58(1): 700, 1998.

[102] Ho Trung Dung, Ludwig Knöll, and Dirk-Gunnar Welsch. Resonant dipole-dipole interaction in the presence of dispersing and absorbing surroundings. *Physical Review A*, 66(6):063810, 2002.

[103] David Dzsotjan, Anders S Sørensen, and Michael Fleischhauer. Quantum emitters coupled to surface plasmons of a nanowire: A Green's function approach. *Physical Review B*, 82(7):075427, 2010.

[104] RH Lehmberg. Radiation from an N-atom system. I. General formalism. *Physical Review A*, 2(3):883, 1970.

[105] Gershon Kurizki. Two-atom resonant radiative coupling in photonic band structures. *Physical Review A*, 42(5):2915, 1990.

[106] Xiangjin Kong, Darrick E Chang, and Adriana Pálffy. Green's-function formalism for resonant interaction of x rays with nuclei in structured media. *Physical Review A*, 102(3):033710, 2020.

[107] Ana Asenjo-Garcia, M Moreno-Cardoner, Andreas Albrecht, HJ Kimble, and Darrick E Chang. Exponential improvement in photon storage fidelities using subradiance and "selective radiance" in atomic arrays. *Physical Review X*, 7(3): 031024, 2017.

[108] Maria Moreno-Cardoner, David Plankensteiner, Laurin Ostermann, Darrick E Chang, and Helmut Ritsch. Subradiance-enhanced excitation transfer between dipole-coupled nanorings of quantum emitters. *Physical Review A*, 100(2):023806, 2019.

[109] E Stourm, Maxence Lepers, J Robert, S Nic Chormaic, K Mølmer, and E Brion. Spontaneous emission and energy shifts of a Rydberg rubidium atom close to an optical nanofiber. *Physical Review A*, 101(5):052508, 2020.

[110] Robert M White, Robert M White, and Bradford Bayne. *Quantum theory of magnetism*, volume 1. Springer, 1983.

[111] Jacques Des Cloizeaux. Analytical properties of n-dimensional energy bands and wannier functions. *Physical Review*, 135(3A):A698, 1964.

[112] Alejandro González-Tudela, C-L Hung, Darrick E Chang, J Ignacio Cirac, and HJ Kimble. Subwavelength vacuum lattices and atom–atom interactions in two-dimensional photonic crystals. *Nature Photonics*, 9(5):320–325, 2015.

[113] Su-Peng Yu, Juan A Muniz, Chen-Lung Hung, and HJ Kimble. Two-dimensional photonic crystals for engineering atom–light interactions. *Proceedings of the National Academy of Sciences*, 116(26):12743–12751, 2019.

[114] Alexander P Burgers, Lucas S Peng, Juan A Muniz, Andrew C McClung, Michael Joseph Martin, and Harry J Kimble. Clocked atom delivery to a photonic crystal waveguide. *Proceedings of the National Academy of Sciences*, 116 (2):456–465, 2019.

[115] Fam Le Kien, VI Balykin, and K Hakuta. Atom trap and waveguide using a two-color evanescent light field around a subwavelength-diameter optical fiber. *Physical Review A*, 70(6):063403, 2004.

[116] Adam T Black, James K Thompson, and Vladan Vuletić. On-demand superradiant conversion of atomic spin gratings into single photons with high efficiency. *Physical Review Letters*, 95(13):133601, 2005.

[117] René Reimann, Wolfgang Alt, Tobias Kampschulte, Tobias Macha, Lothar Ratschbacher, Natalie Thau, Seokchan Yoon, and Dieter Meschede. Cavity-modified collective Rayleigh scattering of two atoms. *Physical Review Letters*, 114(2):023601, 2015.

[118] Matthew A Norcia, Robert J Lewis-Swan, Julia RK Cline, Bihui Zhu, Ana M Rey, and James K Thompson. Cavity-mediated collective spin-exchange interactions in a strontium superradiant laser. *Science*, 361(6399):259–262, 2018.

[119] Hilton W Chan, Adam T Black, and Vladan Vuletić. Observation of collective-emission-induced cooling of atoms in an optical cavity. *Physical Review Letters*, 90(6):063003, 2003.

[120] Neil V Corzo, Jérémy Raskop, Aveek Chandra, Alexandra S Sheremet, Baptiste Gouraud, and Julien Laurat. Waveguide-coupled single collective excitation of atomic arrays. *Nature*, 566(7744):359–362, 2019.

[121] Pablo Solano, Pablo Barberis-Blostein, Fredrik K Fatemi, Luis A Orozco, and Steven L Rolston. Super-radiance reveals infinite-range dipole interactions through a nanofiber. *Nature Communications*, 8(1):1–7, 2017.

[122] Maximilian Zanner, Tuure Orell, Christian MF Schneider, Romain Albert, Stefan Oleschko, Mathieu L Juan, Matti Silveri, and Gerhard Kirchmair. Coherent control of a multi-qubit dark state in waveguide quantum electrodynamics. *Nature Physics*, 18(5):538–543, 2022.

[123] Vanessa Paulisch, HJ Kimble, and Alejandro González-Tudela. Universal quantum computation in waveguide QED using decoherence free subspaces. *New Journal of Physics*, 18(4):043041, 2016.

[124] Ibrahim Alghoraibi and Sandy Alomari. Different methods for nanofiber design and fabrication. *Handbook of Nanofibers*, pages 1–46, 2018.

[125] JM Ward, A Maimaiti, Vu H Le, and S Nic Chormaic. Contributed review: Optical micro-and nanofiber pulling rig. *Review of Scientific Instruments*, 85 (11):111501, 2014.

[126] JE Hoffman, S Ravets, JA Grover, P Solano, PR Kordell, JD Wong-Campos, LA Orozco, and SL Rolston. Ultrahigh transmission optical nanofibers. *AIP Advances*, 4(6):067124, 2014.

[127] Riccardo Pennetta, Daniel Lechner, Martin Blaha, Arno Rauschenbeutel, Philipp Schneeweiss, and Jürgen Volz. Observation of coherent coupling between super- and subradiant states of an ensemble of cold atoms collectively coupled to a single propagating optical mode. *Physical Review Letters*, 128(20):203601, 2022.

[128] Limin Tong, Jingyi Lou, and Eric Mazur. Single-mode guiding properties of subwavelength-diameter silica and silicon wire waveguides. *Optics Express*, 12 (6):1025–1035, 2004.

[129] Huakang Yu, Shanshan Wang, Jian Fu, Min Qiu, Yuhang Li, Fuxing Gu, and Limin Tong. Modeling bending losses of optical nanofibers or nanowires. *Applied Optics*, 48(22):4365–4369, 2009.

[130] Masazumi Fujiwara, Tetsuya Noda, Akira Tanaka, Kiyota Toubaru, Hong-Quan Zhao, and Shigeki Takeuchi. Coupling of ultrathin tapered fibers with high-Q microsphere resonators at cryogenic temperatures and observation of phase-shift transition from undercoupling to overcoupling. *Optics Express*, 20(17):19545–19553, 2012.

[131] Xu Zeng, Yu Wu, Changlun Hou, Jian Bai, and Guoguang Yang. A temperature sensor based on optical microfiber knot resonator. *Optics Communications*, 282 (18):3817–3819, 2009.

[132] Fei Xu, Valerio Pruneri, Vittoria Finazzi, and Gilberto Brambilla. An embedded optical nanowire loop resonator refractometric sensor. *Optics Express*, 16(2): 1062–1067, 2008.

[133] KP Nayak, PN Melentiev, M Morinaga, Fam Le Kien, VI Balykin, and K Hakuta. Optical nanofiber as an efficient tool for manipulating and probing atomic fluorescence. *Optics Express*, 15(9):5431–5438, 2007.

[134] Georgiy Tkachenko, Ivan Toftul, Cindy Esporlas, Aili Maimaiti, Fam Le Kien, Viet Giang Truong, and Síle Nic Chormaic. Light-induced rotation of dielectric microparticles around an optical nanofiber. *Optica*, 7(1):59–62, 2020.

[135] Aili Maimaiti, Viet Giang Truong, Marios Sergides, Ivan Gusachenko, and Síle Nic Chormaic. Higher order microfibre modes for dielectric particle trapping and propulsion. *Scientific Reports*, 5(1):1–8, 2015.

[136] Cindy Esporlas, Georgiy Tkachenko, Isha Sanskriti, Viet Giang Truong, and Síle Nic Chormaic. Efficient optical manipulation of Janus particles by optical nanofibers. *arXiv preprint arXiv:2108.00748*, 2021.

[137] Zachary Eldredge, Pablo Solano, Darrick Chang, and Alexey V Gorshkov. Self-organization of atoms coupled to a chiral reservoir. *Physical Review A*, 94(5): 053855, 2016.

[138] Alexander V Poshakinskiy, Janet Zhong, Yongguan Ke, Nikita A Olekhno, Chaohong Lee, Yuri S Kivshar, and Alexander N Poddubny. Quantum Hall phases

emerging from atom–photon interactions. *npj Quantum Information*, 7(1):1–8, 2021.

[139] Simon Gröblacher, Jeff T Hill, Amir H Safavi-Naeini, Jasper Chan, and Oskar Painter. Highly efficient coupling from an optical fiber to a nanoscale silicon optomechanical cavity. *Applied Physics Letters*, 103(18):181104, 2013.

[140] Etienne Brion, F Carlier, VM Akulin, and K Mølmer. Quantum repeater with Rydberg-blocked atomic ensembles in fiber-coupled cavities. *Physical Review A*, 85(4):042324, 2012.

[141] Vitalie Eremeev, Victor Montenegro, and Miguel Orszag. Thermally generated long-lived quantum correlations for two atoms trapped in fiber-coupled cavities. *Physical Review A*, 85(3):032315, 2012.

[142] Shinya Kato, Nikolett Német, Kohei Senga, Shota Mizukami, Xinhe Huang, Scott Parkins, and Takao Aoki. Observation of dressed states of distant atoms with delocalized photons in coupled-cavities quantum electrodynamics. *Nature Communications*, 10(1):1–6, 2019.

[143] Jonathan M Ward, Fuchuan Lei, Stephy Vincent, Pooja Gupta, Samir K Mondal, Jochen Fick, and Síle Nic Chormaic. Excitation of whispering gallery modes with a "point-and-play," fiber-based, optical nano-antenna. *Optics Letters*, 44 (13):3386–3389, 2019.

[144] J Cheung Knight, G Cheung, F Jacques, and TA Birks. Phase-matched excitation of whispering-gallery-mode resonances by a fiber taper. *Optics Letters*, 22(15): 1129–1131, 1997.

[145] Fam Le Kien and K Hakuta. Cavity-enhanced channeling of emission from an atom into a nanofiber. *Physical Review A*, 80(5):053826, 2009.

[146] KP Nayak, Fam Le Kien, Y Kawai, K Hakuta, K Nakajima, HT Miyazaki, and Y Sugimoto. Cavity formation on an optical nanofiber using focused ion beam milling technique. *Optics Express*, 19(15):14040–14050, 2011.

[147] C Wuttke, Martin Becker, S Brückner, M Rothhardt, and A Rauschenbeutel. Nanofiber Fabry–Perot microresonator for nonlinear optics and cavity quantum electrodynamics. *Optics Letters*, 37(11):1949–1951, 2012.

[148] Shinya Kato and Takao Aoki. Strong coupling between a trapped single atom and an all-fiber cavity. *Physical Review Letters*, 115(9):093603, 2015.

[149] Kaiwei Li, Nan Zhang, Nancy Meng Ying Zhang, Guigen Liu, Ting Zhang, and Lei Wei. Ultrasensitive measurement of gas refractive index using an optical nanofiber coupler. *Optics Letters*, 43(4):679–682, 2018.

[150] Xiao-Chong Yu, Bei-Bei Li, Pan Wang, Limin Tong, Xue-Feng Jiang, Yan Li, Qihuang Gong, and Yun-Feng Xiao. Single nanoparticle detection and sizing using a nanofiber pair in an aqueous environment. *Advanced Materials*, 26(44): 7462–7467, 2014.

[151] Ramgopal Madugani, Yong Yang, Jonathan M Ward, Vu H Le, and Síle Nic Chormaic. Optomechanical transduction and characterization of a silica microsphere pendulum via evanescent light. *Applied Physics Letters*, 106(24):241101, 2015.

[152] Hongbao Xin, Chang Cheng, and Baojun Li. Trapping and delivery of Escherichia coli in a microfluidic channel using an optical nanofiber. *Nanoscale*, 5(15):6720–6724, 2013.

[153] BD Patterson, P Solano, PS Julienne, LA Orozco, and SL Rolston. Spectral asymmetry of atoms in the van der Waals potential of an optical nanofiber. *Physical Review A*, 97(3):032509, 2018.

[154] Georgiy Tkachenko, Ivan Toftul, Alexey Vylegzhanin, Viet Giang Truong, Mihail Petrov, and Sile Nic Chormaic. Detection of the transverse spin of light by twisting anisotropic particles near an optical nanofiber waveguide. In *Optical Manipulation and Structured Materials Conference 2021*, volume 11926, pages 69–71. SPIE, 2021.

[155] VI Balykin, K Hakuta, Fam Le Kien, JQ Liang, and M Morinaga. Atom trapping and guiding with a subwavelength-diameter optical fiber. *Physical Review A*, 70 (1):011401, 2004.

[156] AH Barnett, SP Smith, M Olshanii, KS Johnson, AW Adams, and M Prentiss. Substrate-based atom waveguide using guided two-color evanescent light fields. *Physical Review A*, 61(2):023608, 2000.

[157] Neil V Corzo, Baptiste Gouraud, Aveek Chandra, Akihisa Goban, Alexandra S Sheremet, Dmitriy V Kupriyanov, and Julien Laurat. Large Bragg reflection from one-dimensional chains of trapped atoms near a nanoscale waveguide. *Physical Review Letters*, 117(13):133603, 2016.

[158] Y Meng, A Dareau, P Schneeweiss, and A Rauschenbeutel. Near-ground-state cooling of atoms optically trapped 300 nm away from a hot surface. *Physical Review X*, 8(3):031054, 2018.

[159] M Hammes, D Rychtarik, B Engeser, H-C Nägerl, and R Grimm. Evanescent-wave trapping and evaporative cooling of an atomic gas at the crossover to two dimensions. *Physical Review Letters*, 90(17):173001, 2003.

[160] Katharina Christandl, Gregory P Lafyatis, Seung-Cheol Lee, and Jin-Fa Lee. One-and two-dimensional optical lattices on a chip for quantum computing. *Physical Review A*, 70(3):032302, 2004.

[161] Fam Le Kien, S Dutta Gupta, KP Nayak, and K Hakuta. Nanofiber-mediated radiative transfer between two distant atoms. *Physical Review A*, 72(6):063815, 2005.

[162] Fam Le Kien and K Hakuta. Cooperative enhancement of channeling of emission from atoms into a nanofiber. *Physical Review A*, 77(1):013801, 2008.

[163] R Miller, TE Northup, KM Birnbaum, ADBA Boca, AD Boozer, and HJ Kimble. Trapped atoms in cavity QED: coupling quantized light and matter. *Journal of Physics B: Atomic, Molecular and Optical Physics*, 38(9):S551, 2005.

[164] Adarsh S Prasad, Jakob Hinney, Sahand Mahmoodian, Klemens Hammerer, Samuel Rind, Philipp Schneeweiss, Anders S Sørensen, Jürgen Volz, and Arno Rauschenbeutel. Correlating photons using the collective nonlinear response of atoms weakly coupled to an optical mode. *Nature Photonics*, 14(12):719–722, 2020.

[165] Fam Le Kien, Philipp Schneeweiss, and Arno Rauschenbeutel. Dynamical polarizability of atoms in arbitrary light fields: general theory and application to cesium. *The European Physical Journal D*, 67(5):1–16, 2013.

[166] Alexandre Dareau, Y Meng, P Schneeweiss, and A Rauschenbeutel. Observation of ultrastrong spin-motion coupling for cold atoms in optical microtraps. *Physical Review Letters*, 121(25):253603, 2018.

[167] Sebastian Pucher, Christian Liedl, Shuwei Jin, Arno Rauschenbeutel, and Philipp Schneeweiss. Atomic spin-controlled non-reciprocal Raman amplification of fibre-guided light. *Nature Photonics*, 16(5):380–383, 2022.

[168] Katsunari Okamoto. *Fundamentals of optical waveguides*. Elsevier, 2021.

[169] Jingyi Lou, Limin Tong, and Zhizhen Ye. Modeling of silica nanowires for optical sensing. *Optics Express*, 13(6):2135–2140, 2005.

[170] Darrick E Chang, Anders Søndberg Sørensen, PR Hemmer, and MD Lukin. Strong coupling of single emitters to surface plasmons. *Physical Review B*, 76(3): 035420, 2007.

[171] Qianfan Xu, Vilson R Almeida, Roberto R Panepucci, and Michal Lipson. Experimental demonstration of guiding and confining light in nanometer-size low-refractive-index material. *Optics Letters*, 29(14):1626–1628, 2004.

[172] Mark Daly, Viet Giang Truong, CF Phelan, Kieran Deasy, and S Nic Chormaic. Nanostructured optical nanofibres for atom trapping. *New Journal of Physics*, 16(5):053052, 2014.

[173] Mark Daly, Viet Giang Truong, and Síle Nic Chormaic. Evanescent field trapping of nanoparticles using nanostructured ultrathin optical fibers. *Optics Express*, 24 (13):14470–14482, 2016.

[174] Steven Chu. Nobel lecture: The manipulation of neutral particles. *Reviews of Modern Physics*, 70(3):685, 1998.

[175] Claude N Cohen-Tannoudji. Nobel lecture: Manipulating atoms with photons. *Reviews of Modern Physics*, 70(3):707, 1998.

[176] James S Douglas, Tommaso Caneva, and Darrick E Chang. Photon molecules in atomic gases trapped near photonic crystal waveguides. *Physical Review X*, 6 (3):031017, 2016.

[177] Alan L Jones. Coupling of optical fibers and scattering in fibers. *JOSA*, 55(3): 261–271, 1965.

[178] S Somekh, E Garmire, A Yariv, HL Garvin, and RG Hunsperger. Channel optical waveguide directional couplers. *Applied Physics Letters*, 22(1):46–47, 1973.

[179] Karl Leo, Peter Haring Bolivar, Frank Brüggemann, Ralf Schwedler, and Klaus Köhler. Observation of Bloch oscillations in a semiconductor superlattice. *Solid State Communications*, 84(10):943–946, 1992.

[180] Felix Bloch. Über die quantenmechanik der elektronen in kristallgittern. *Zeitschrift für physik*, 52(7):555–600, 1929.

[181] Stefano Longhi. Quantum-optical analogies using photonic structures. *Laser & Photonics Reviews*, 3(3):243–261, 2009.

[182] T Pertsch, P Dannberg, W Elflein, A Bräuer, and F Lederer. Optical Bloch oscillations in temperature tuned waveguide arrays. *Physical Review Letters*, 83 (23):4752, 1999.

[183] Carl M Bender, Stefan Boettcher, and Peter N Meisinger. PT-symmetric quantum mechanics. *Journal of Mathematical Physics*, 40(5):2201–2229, 1999.

[184] Stefano Longhi. Bloch oscillations in complex crystals with PT symmetry. *Physical Review Letters*, 103(12):123601, 2009.

[185] R El-Ganainy, KG Makris, DN Christodoulides, and Ziad H Musslimani. Theory of coupled optical PT-symmetric structures. *Optics Letters*, 32(17):2632–2634, 2007.

[186] Mark Kremer, Tobias Biesenthal, Lukas J Maczewsky, Matthias Heinrich, Ronny Thomale, and Alexander Szameit. Demonstration of a two-dimensional PT-symmetric crystal. *Nature Communications*, 10(1):1–7, 2019.

[187] Liang Feng, Zi Jing Wong, Ren-Min Ma, Yuan Wang, and Xiang Zhang. Single-mode laser by parity-time symmetry breaking. *Science*, 346(6212):972–975, 2014.

[188] Steffen Weimann, Manuel Kremer, Yonatan Plotnik, Yaakov Lumer, Stefan Nolte, Konstantinos G Makris, Mordechai Segev, Mikael C Rechtsman, and Alexander Szameit. Topologically protected bound states in photonic parity–time-symmetric crystals. *Nature Materials*, 16(4):433–438, 2017.

[189] Paolo Biagioni, Giuseppe Della Valle, Marco Ornigotti, Marco Finazzi, Lamberto Duo, Paolo Laporta, and Stefano Longhi. Experimental demonstration of the optical Zeno effect by scanning tunneling optical microscopy. *Optics Express*, 16 (6):3762–3767, 2008.

[190] Stefano Longhi. Nonexponential decay via tunneling in tight-binding lattices and the optical Zeno effect. *Physical Review Letters*, 97(11):110402, 2006.

[191] Stefano Longhi. Optical Bloch oscillations and Zener tunneling with nonclassical light. *Physical Review Letters*, 101(19):193902, 2008.

[192] F Klauck, Lucas Teuber, Marco Ornigotti, Matthias Heinrich, Stefan Scheel, and Alexander Szameit. Observation of PT-symmetric quantum interference. *Nature Photonics*, 13(12):883–887, 2019.

[193] SE Miller. Coupled wave theory and waveguide applications. *Bell System Technical Journal*, 33(3):661–719, 1954.

[194] John Robinson Pierce. Coupling of modes of propagation. *Journal of Applied Physics*, 25(2):179–183, 1954.

[195] Hermann A Haus. Electron beam waves in microwave tubes. 1958.

[196] Dietrich Marcuse. The coupling of degenerate modes in two parallel dielectric waveguides. *Bell System Technical Journal*, 50(6):1791–1816, 1971.

[197] D Marcuse. Coupled mode theory of round optical fibers. *Bell System Technical Journal*, 52(6):817–842, 1973.

[198] Hermann A Haus, Wei-Ping Huang, and Allan W Snyder. Coupled-mode formulations. *Optics Letters*, 14(21):1222–1224, 1989.

[199] Wei-Ping Huang. Coupled-mode theory for optical waveguides: an overview. *JOSA A*, 11(3):963–983, 1994.

[200] Chih-Sheng Chang and Hung-Chun Chang. Vector normal modes on two-core optical fibers. II. the modal cutoffs. *Journal of Lightwave Technology*, 15(7): 1225–1232, 1997.

[201] Horng Shou Huang and Hung-Chun Chang. Vector coupled-mode analysis of coupling between two identical optical fiber cores. *Optics Letters*, 14(1):90–92, 1989.

[202] W Wijngaard. Guided normal modes of two parallel circular dielectric rods. *JOSA*, 63(8):944–950, 1973.

[203] Chih-Sheng Chang and Hung-Chun Chang. Vector normal modes on two-core optical fibers. I. the normal mode solutions. *Journal of Lightwave Technology*, 15(7):1213–1224, 1997.

[204] GH Wang, P Shum, GB Ren, X Yu, JJ Hu, and C Lin. Theoretical investigation of nanowaveguide-based optical coupler using mode expansion transfer matrix. *Microwave and Optical Technology Letters*, 52(5):1123–1129, 2010.

[205] Gaetano Bellanca, Piero Orlandi, and Paolo Bassi. Assessment of the orthogonal and non-orthogonal coupled-mode theory for parallel optical waveguide couplers. *JOSA A*, 35(4):577–585, 2018.

[206] DN Christodoulides and RI Joseph. Discrete self-focusing in nonlinear arrays of coupled waveguides. *Optics Letters*, 13(9):794–796, 1988.

[207] Ashraf El Hassan, Flore K Kunst, Alexander Moritz, Guillermo Andler, Emil J Bergholtz, and Mohamed Bourennane. Corner states of light in photonic waveguides. *Nature Photonics*, 13(10):697–700, 2019.

[208] Alán Aspuru-Guzik and Philip Walther. Photonic quantum simulators. *Nature Physics*, 8(4):285–291, 2012.

[209] M Sumetsky. Optical fiber microcoil resonator. *Optics Express*, 12(10):2303–2316, 2004.

[210] Dietrich Marcuse. Light transmission optics. *New York*, 1982.

[211] WP Huang and Herman A Haus. Self-consistent vector coupled-mode theory for tapered optical waveguides. *Journal of Lightwave Technology*, 8(6):922–926, 1990.

[212] Fredrik K Fatemi, Jonathan E Hoffman, Pablo Solano, Eliot F Fenton, Guy Beadie, Steven L Rolston, and Luis A Orozco. Modal interference in optical nanofibers for sub-Angstrom radius sensitivity. *Optica*, 4(1):157–162, 2017.

[213] Jing Wang, Yipeng Liao, Shanshan Wang, and Xin Wang. Ultrasensitive optical sensing in aqueous solution based on microfiber modal interferometer. *Optics Express*, 26(19):24843–24853, 2018.

[214] AA Asatryan, Kurt Busch, RC McPhedran, LC Botten, C Martijn de Sterke, and NA Nicorovici. Two-dimensional Green tensor and local density of states in finite-sized two-dimensional photonic crystals. *Waves in Random Media*, 13(1): 9, 2002.

[215] Milton Abramowitz and Irene A Stegun. *Handbook of mathematical functions with formulas, graphs, and mathematical tables*, volume 55. US Government printing office, 1964.

[216] Fabrice Gerbier and Yvan Castin. Heating rates for an atom in a far-detuned optical lattice. *Physical Review A*, 82(1):013615, 2010.

[217] Karim Murr, Peter Maunz, Pepijn WH Pinkse, Thomas Puppe, Ingrid Schuster, D Vitali, and Gerhard Rempe. Momentum diffusion for coupled atom-cavity oscillators. *Physical Review A*, 74(4):043412, 2006.

[218] Peng Xu, Xiaodong He, Jin Wang, and Mingsheng Zhan. Trapping a single atom in a blue detuned optical bottle beam trap. *Optics Letters*, 35(13):2164–2166, 2010.

[219] Roee Ozeri, Lev Khaykovich, and Nir Davidson. Long spin relaxation times in a single-beam blue-detuned optical trap. *Physical Review A*, 59(3):R1750, 1999.

[220] Daniel Barredo, Vincent Lienhard, Pascal Scholl, Sylvain de Léséleuc, Thomas Boulier, Antoine Browaeys, and Thierry Lahaye. Three-dimensional trapping of individual Rydberg atoms in ponderomotive bottle beam traps. *Physical Review Letters*, 124(2):023201, 2020.

[221] Krishnapriya Subramonian Rajasree, Tridib Ray, Kristoffer Karlsson, Jesse L Everett, and Síle Nic Chormaic. Generation of cold Rydberg atoms at submicron distances from an optical nanofiber. *Physical Review Research*, 2(1):012038, 2020.

[222] Ran Finkelstein, Gal Winer, David Zeev Koplovich, Or Arenfrid, Thomas Hoinkes, Gabriel Guendelman, Moran Netser, Eilon Poem, Arno Rauschenbeutel, Barak Dayan, et al. Super-extended nanofiber-guided field for coherent interaction with hot atoms. *Optica*, 8(2):208–215, 2021.

[223] Fam Le Kien, Síle Nic Chormaic, and Thomas Busch. Optical force between two coupled identical parallel optical nanofibers. *Physical Review A*, 105(6):063517, 2022.

[224] Jacob N Israelachvili. van der Waals forces in biological systems. *Quarterly Reviews of Biophysics*, 6(4):341–387, 1973.

[225] Kellar Autumn, Metin Sitti, Yiching A Liang, Anne M Peattie, Wendy R Hansen, Simon Sponberg, Thomas W Kenny, Ronald Fearing, Jacob N Israelachvili, and Robert J Full. Evidence for van der Waals adhesion in gecko setae. *Proceedings of the National Academy of Sciences*, 99(19):12252–12256, 2002.

[226] T Poppe, J Blum, and Th Henning. New experiments on collisions of solid grains related to the preplanetary dust aggregation. *Advances in Space Research*, 23(7): 1197–1200, 1999.

[227] RS Decca, E Fischbach, GL Klimchitskaya, DE Krause, D López, and VM Mostepanenko. Improved tests of extra-dimensional physics and thermal quantum field theory from new Casimir force measurements. *Physical Review D*, 68(11):116003, 2003.

[228] Franz J Giessibl. Advances in atomic force microscopy. *Reviews of Modern Physics*, 75(3):949, 2003.

[229] HN De Freitas, M Oria, and M Chevrollier. Spectroscopy of cesium atoms adsorbing and desorbing at a dielectric surface. *Applied Physics B*, 75(6):703–709, 2002.

[230] Ralf Ritter, Nico Gruhler, Wolfram Pernice, Harald Kübler, Tilman Pfau, and Robert Löw. Atomic vapor spectroscopy in integrated photonic structures. *Applied Physics Letters*, 107(4):041101, 2015.

[231] JA Sedlacek, Eunja Kim, ST Rittenhouse, PF Weck, HR Sadeghpour, and JP Shaffer. Electric field cancellation on quartz by Rb adsorbate-induced negative electron affinity. *Physical Review Letters*, 116(13):133201, 2016.

[232] Atreju Tauschinsky, Rutger MT Thijssen, S Whitlock, HB van Linden van den Heuvell, and RJC Spreeuw. Spatially resolved excitation of Rydberg atoms and surface effects on an atom chip. *Physical Review A*, 81(6):063411, 2010.

[233] Fritz London. Zur theorie und systematik der molekularkräfte. *Zeitschrift für Physik*, 63(3):245–279, 1930.

[234] AD McLachlan. van der Waals forces between an atom and a surface. *Molecular Physics*, 7(4):381–388, 1964.

[235] Hassan Safari, Stefan Yoshi Buhmann, Dirk-Gunnar Welsch, and Ho Trung Dung. Body-assisted van der Waals interaction between two atoms. *Physical Review A*, 74(4):042101, 2006.

[236] Pablo Barcellona, Hassan Safari, A Salam, and Stefan Yoshi Buhmann. Enhanced chiral discriminatory van der Waals interactions mediated by chiral surfaces. *Physical Review Letters*, 118(19):193401, 2017.

[237] Stefan Buhmann. *Dispersion Forces II: Many-Body Effects, Excited Atoms, Finite Temperature and Quantum Friction*, volume 248. Springer, 2013.

[238] KV Shajesh and M Schaden. Repulsive long-range forces between anisotropic atoms and dielectrics. *Physical Review A*, 85(1):012523, 2012.

[239] Stefan Yoshi Buhmann, Valery N Marachevsky, and Stefan Scheel. Impact of anisotropy on the interaction of an atom with a one-dimensional nano-grating. *International Journal of Modern Physics A*, 31(02n03):1641029, 2016.

[240] Michael Levin, Alexander P McCauley, Alejandro W Rodriguez, MT Homer Reid, and Steven G Johnson. Casimir repulsion between metallic objects in vacuum. *Physical Review Letters*, 105(9):090403, 2010.

[241] Stefan Scheel, Stefan Yoshi Buhmann, Christoph Clausen, and Philipp Schneeweiss. Directional spontaneous emission and lateral Casimir-Polder force on an atom close to a nanofiber. *Physical Review A*, 92(4):043819, 2015.

[242] Gorachand Ghosh. *Handbook of optical constants of solids: Handbook of thermo-optic coefficients of optical materials with applications*. Academic Press, 1998.

[243] Sahand Jamal Rahi, Mehran Kardar, and Thorsten Emig. Constraints on stable equilibria with fluctuation-induced (Casimir) forces. *Physical Review Letters*, 105 (7):070404, 2010.

[244] Daniel A Steck. Cesium D line data. 2003.

[245] M Dalmonte, SI Mirzaei, PR Muppalla, D Marcos, P Zoller, and G Kirchmair. Realizing dipolar spin models with arrays of superconducting qubits. *Physical Review B*, 92(17):174507, 2015.

[246] Guanyu Zhu, Mohammad Hafezi, and Tarun Grover. Measurement of many-body chaos using a quantum clock. *Physical Review A*, 94(6):062329, 2016.

[247] Nguyen Dung Chinh. Strong enhancement and inhibition of the interatomic van der Waals interaction inside a cylindrical waveguide. *The European Physical Journal D*, 74(5):1–7, 2020.

[248] Ephraim Shahmoon and Gershon Kurizki. Dispersion forces inside metallic waveguides. *Physical Review A*, 87(6):062105, 2013.

[249] Fam Le Kien, DF Kornovan, Síle Nic Chormaic, and Thomas Busch. Repulsive Casimir-Polder potentials of low-lying excited states of a multilevel alkali-metal atom near an optical nanofiber. *Physical Review A*, 105(4):042817, 2022.

[250] Luca Pezze, Augusto Smerzi, Markus K Oberthaler, Roman Schmied, and Philipp Treutlein. Quantum metrology with nonclassical states of atomic ensembles. *Reviews of Modern Physics*, 90(3):035005, 2018.

[251] Carlton M Caves. Quantum-mechanical noise in an interferometer. *Physical Review D*, 23(8):1693, 1981.

[252] Jonathan P Dowling. Correlated input-port, matter-wave interferometer: Quantum-noise limits to the atom-laser gyroscope. *Physical Review A*, 57(6): 4736, 1998.

[253] Emanuele Polino, Mauro Valeri, Nicolò Spagnolo, and Fabio Sciarrino. Photonic quantum metrology. *AVS Quantum Science*, 2(2):024703, 2020.

[254] Vittorio Giovannetti, Seth Lloyd, and Lorenzo Maccone. Advances in quantum metrology. *Nature Photonics*, 5(4):222–229, 2011.

[255] Max F Riedel, Pascal Böhi, Yun Li, Theodor W Hänsch, Alice Sinatra, and Philipp Treutlein. Atom-chip-based generation of entanglement for quantum metrology. *Nature*, 464(7292):1170–1173, 2010.

[256] Weiting Wang, Yukai Wu, Yuwei Ma, Weizhou Cai, Ling Hu, Xianghao Mu, Yuan Xu, Zi-Jie Chen, Haiyan Wang, YP Song, et al. Heisenberg-limited single-mode quantum metrology in a superconducting circuit. *Nature Communications*, 10 (1):1–6, 2019.

[257] Irénée Frérot and Tommaso Roscilde. Quantum critical metrology. *Physical Review Letters*, 121(2):020402, 2018.

[258] Louis Garbe, Obinna Abah, Simone Felicetti, and Ricardo Puebla. Exponential precision by reaching a quantum critical point. *arXiv preprint arXiv:2112.11264*, 2021.

[259] Andrew M Childs, Edward Farhi, and John Preskill. Robustness of adiabatic quantum computation. *Physical Review A*, 65(1):012322, 2001.

[260] Marek M Rams, Piotr Sierant, Omyoti Dutta, Paweł Horodecki, and Jakub Zakrzewski. At the limits of criticality-based quantum metrology: Apparent super-Heisenberg scaling revisited. *Physical Review X*, 8(2):021022, 2018.

[261] Karol Gietka, Friederike Metz, Tim Keller, and Jing Li. Adiabatic critical quantum metrology cannot reach the Heisenberg limit even when shortcuts to adiabaticity are applied. *Quantum*, 5:489, 2021.

[262] Matteo GA Paris. Quantum estimation for quantum technology. *International Journal of Quantum Information*, 7(supp01):125–137, 2009.

[263] SM Roy and Samuel L Braunstein. Exponentially enhanced quantum metrology. *Physical Review Letters*, 100(22):220501, 2008.

[264] Sergio Boixo, Steven T Flammia, Carlton M Caves, and John M Geremia. Generalized limits for single-parameter quantum estimation. *Physical Review Letters*, 98(9):090401, 2007.

[265] Anthony J Hayes, Shane Dooley, William J Munro, Kae Nemoto, and Jacob Dunningham. Making the most of time in quantum metrology: concurrent state preparation and sensing. *Quantum Science and Technology*, 3(3):035007, 2018.

[266] Jan Czajkowski, Krzysztof Pawłowski, and Rafał Demkowicz-Dobrzański. Many-body effects in quantum metrology. *New Journal of Physics*, 21(5):053031, 2019.

[267] M Penasa, S Gerlich, T Rybarczyk, V Métillon, M Brune, JM Raimond, S Haroche, L Davidovich, and I Dotsenko. Measurement of a microwave field amplitude beyond the standard quantum limit. *Physical Review A*, 94(2):022313, 2016.

[268] Mingjie Xin, Wui Seng Leong, Zilong Chen, Yu Wang, and Shau-Yu Lan. Rapid quantum squeezing by jumping the harmonic oscillator frequency. *Physical Review Letters*, 127(18):183602, 2021.

[269] Peter Kirton, Mor M Roses, Jonathan Keeling, and Emanuele G Dalla Torre. Introduction to the Dicke model: From equilibrium to nonequilibrium, and vice versa. *Advanced Quantum Technologies*, 2(1-2):1800043, 2019.

[270] Kristian Baumann, Christine Guerlin, Ferdinand Brennecke, and Tilman Esslinger. Dicke quantum phase transition with a superfluid gas in an optical cavity. *Nature*, 464(7293):1301–1306, 2010.

[271] Arghavan Safavi-Naini, RJ Lewis-Swan, Justin G Bohnet, M Gärttner, KA Gilmore, JE Jordan, J Cohn, James K Freericks, Ana Maria Rey, and JJ Bollinger. Verification of a many-ion simulator of the Dicke model through slow quenches across a phase transition. *Physical Review Letters*, 121(4):040503, 2018.

[272] Markus P Baden, Kyle J Arnold, Arne L Grimsmo, Scott Parkins, and Murray D Barrett. Realization of the Dicke model using cavity-assisted Raman transitions. *Physical Review Letters*, 113(2):020408, 2014.

[273] Clive Emary and Tobias Brandes. Chaos and the quantum phase transition in the Dicke model. *Physical Review E*, 67(6):066203, 2003.

[274] RJ Lewis-Swan, Arghavan Safavi-Naini, John J Bollinger, and Ana M Rey. Unifying scrambling, thermalization and entanglement through measurement of fidelity out-of-time-order correlators in the Dicke model. *Nature Communications*, 10(1): 1–9, 2019.

[275] Peter Kirton and Jonathan Keeling. Superradiant and lasing states in driven-dissipative Dicke models. *New Journal of Physics*, 20(1):015009, 2018.

[276] Ye-Hong Chen, Wei Qin, Xin Wang, Adam Miranowicz, and Franco Nori. Shortcuts to adiabaticity for the quantum Rabi model: Efficient generation of giant entangled cat states via parametric amplification. *Physical Review Letters*, 126 (2):023602, 2021.

[277] MA Bastarrachea-Magnani, S Lerma-Hernández, and JG Hirsch. Comparative quantum and semiclassical analysis of atom-field systems. I. density of states and excited-state quantum phase transitions. *Physical Review A*, 89(3):032101, 2014.

[278] Sergey Bravyi, David P DiVincenzo, and Daniel Loss. Schrieffer–wolff transformation for quantum many-body systems. *Annals of Physics*, 326(10):2793–2826, 2011.

[279] Karol Gietka and Thomas Busch. Inverted harmonic oscillator dynamics of the nonequilibrium phase transition in the Dicke model. *Physical Review E*, 104(3): 034132, 2021.

[280] Daniel F Walls. Squeezed states of light. *Nature*, 306(5939):141–146, 1983.

[281] Changhun Oh, Changhyoup Lee, Carsten Rockstuhl, Hyunseok Jeong, Jaewan Kim, Hyunchul Nha, and Su-Yong Lee. Optimal Gaussian measurements for phase estimation in single-mode Gaussian metrology. *npj Quantum Information*, 5(1):1–9, 2019.

[282] Zu-Jian Ying, Simone Felicetti, Gang Liu, and Daniel Braak. Critical quantum metrology in the non-linear quantum Rabi model. *arXiv preprint arXiv:2206.08410*, 2022.

[283] Enrico Rinaldi, Roberto Di Candia, Simone Felicetti, and Fabrizio Minganti. Dispersive qubit readout with machine learning. *arXiv preprint arXiv:2112.05332*, 2021.

[284] F Dimer, B Estienne, AS Parkins, and HJ Carmichael. Proposed realization of the Dicke-model quantum phase transition in an optical cavity QED system. *Physical Review A*, 75(1):013804, 2007.

[285] Jens Klinder, Hans Keßler, Matthias Wolke, Ludwig Mathey, and Andreas Hemmerich. Dynamical phase transition in the open Dicke model. *Proceedings of the National Academy of Sciences*, 112(11):3290–3295, 2015.

[286] Dmitry N Chigrin. Radiation pattern of a classical dipole in a photonic crystal: Photon focusing. *Physical Review E*, 70(5):056611, 2004.

[287] R. E. Camley and A. A. Maradudin. Phonon focusing at surfaces. *Physical Review B*, 27(4):1959, 1983.

[288] Alejandro González-Tudela and J Ignacio Cirac. Quantum emitters in two-dimensional structured reservoirs in the nonperturbative regime. *Physical Review Letters*, 119(14):143602, 2017.

[289] A Goban, C-L Hung, S-P Yu, JD Hood, JA Muniz, JH Lee, MJ Martin, AC McClung, KS Choi, Darrick E Chang, et al. Atom–light interactions in photonic crystals. *Nature Communications*, 5(1):1–9, 2014.

[290] Ming Gong, Shiyu Wang, Chen Zha, Ming-Cheng Chen, He-Liang Huang, Yulin Wu, Qingling Zhu, Youwei Zhao, Shaowei Li, Shaojun Guo, et al. Quantum walks on a programmable two-dimensional 62-qubit superconducting processor. *Science*, 372(6545):948–952, 2021.

[291] Anthony Grbic and George V Eleftheriades. An isotropic three-dimensional negative-refractive-index transmission-line metamaterial. *Journal of Applied Physics*, 98(4):043106, 2005.

[292] Eunjong Kim, Xueyue Zhang, Vinicius S Ferreira, Jash Banker, Joseph K Iverson, Alp Sipahigil, Miguel Bello, Alejandro González-Tudela, Mohammad Mirhosseini, and Oskar Painter. Quantum electrodynamics in a topological waveguide. *Physical Review X*, 11(1):011015, 2021.

[293] Viktor G Veselago. Electrodynamics of substances with simultaneously negative electrical and magnetic permeabilities. *Usp. fiz. nauk*, 92(7):517, 1967.

[294] RK Fisher and RW Gould. Resonance cones in the field pattern of a short antenna in an anisotropic plasma. *Physical Review Letters*, 22(21):1093, 1969.

[295] Yu Guo, Ward Newman, Cristian L Cortes, and Zubin Jacob. Applications of hyperbolic metamaterial substrates. *Advances in OptoElectronics*, 2012, 2012.

[296] John Brian Pendry. Negative refraction makes a perfect lens. *Physical Review Letters*, 85(18):3966, 2000.

[297] MV Charukhchyan, ES Sedov, SM Arakelian, and AP Alodjants. Spatially localized structures and oscillons in atomic Bose-Einstein condensates confined in optical lattices. *Physical Review A*, 89(6):063624, 2014.

[298] Clai Owens, Aman LaChapelle, Brendan Saxberg, Brandon M Anderson, Ruichao Ma, Jonathan Simon, and David I Schuster. Quarter-flux Hofstadter lattice in a qubit-compatible microwave cavity array. *Physical Review A*, 97(1): 013818, 2018.

[299] CL Cortes, W Newman, S Molesky, and Z Jacob. Quantum nanophotonics using hyperbolic metamaterials. *Journal of Optics*, 14(6):063001, 2012.

[300] Zubin Jacob, Igor I Smolyaninov, and Evgenii E Narimanov. Broadband Purcell effect: Radiative decay engineering with metamaterials. *Applied Physics Letters*, 100(18):181105, 2012.

[301] S-A Biehs, Maria Tschikin, and Philippe Ben-Abdallah. Hyperbolic metamaterials as an analog of a blackbody in the near field. *Physical Review Letters*, 109 (10):104301, 2012.

[302] Ward D Newman, Cristian L Cortes, Amir Afshar, Ken Cadien, Al Meldrum, Robert Fedosejevs, and Zubin Jacob. Observation of long-range dipole-dipole interactions in hyperbolic metamaterials. *Science Advances*, 4(10):eaar5278, 2018.

[303] Lian Shen, Xiao Lin, Mikhail Y Shalaginov, Tony Low, Xianmin Zhang, Baile Zhang, and Hongsheng Chen. Broadband enhancement of on-chip single-photon extraction via tilted hyperbolic metamaterials. *Applied Physics Reviews*, 7(2): 021403, 2020.

[304] María Blanco de Paz, Alejandro González-Tudela, and Paloma Arroyo Huidobro. Manipulating generalized Dirac cones in quantum metasurfaces. *arXiv preprint arXiv:2203.11195*, 2022.

[305] Jaime Redondo-Yuste, María Blanco de Paz, Paloma A Huidobro, and Alejandro González-Tudela. Quantum electrodynamics in anisotropic and tilted Dirac photonic lattices. *New Journal of Physics*, 23(10):103018, 2021.

[306] Kejie Fang, Zongfu Yu, and Shanhui Fan. Realizing effective magnetic field for photons by controlling the phase of dynamic modulation. *Nature Photonics*, 6 (11):782–787, 2012.

[307] Hadiseh Alaeian, Chung Wai Sandbo Chang, Mehran Vahdani Moghaddam, Christopher M Wilson, Enrique Solano, and Enrique Rico. Creating lattice gauge potentials in circuit QED: The bosonic Creutz ladder. *Physical Review A*, 99(5): 053834, 2019.

[308] Dieter Jaksch and Peter Zoller. Creation of effective magnetic fields in optical lattices: the Hofstadter butterfly for cold neutral atoms. *New Journal of Physics*, 5(1):56, 2003.

[309] Yaacov E Kraus, Yoav Lahini, Zohar Ringel, Mor Verbin, and Oded Zilberberg. Topological states and adiabatic pumping in quasicrystals. *Physical Review Letters*, 109(10):106402, 2012.

[310] Monika Aidelsburger, Marcos Atala, Sylvain Nascimbene, Stefan Trotzky, Y-A Chen, and Immanuel Bloch. Experimental realization of strong effective magnetic fields in an optical lattice. *Physical Review Letters*, 107(25):255301, 2011.

[311] Pedram Roushan, Charles Neill, Anthony Megrant, Yu Chen, Ryan Babbush, Rami Barends, Brooks Campbell, Zijun Chen, Ben Chiaro, Andrew Dunsworth, et al. Chiral ground-state currents of interacting photons in a synthetic magnetic field. *Nature Physics*, 13(2):146–151, 2017.

[312] Yaakov Lumer, Miguel A Bandres, Matthias Heinrich, Lukas J Maczewsky, Hanan Herzig-Sheinfux, Alexander Szameit, and Mordechai Segev. Light guiding by artificial gauge fields. *Nature Photonics*, 13(5):339–345, 2019.

[313] Brandon M Anderson, Ruichao Ma, Clai Owens, David I Schuster, and Jonathan Simon. Engineering topological many-body materials in microwave cavity arrays. *Physical Review X*, 6(4):041043, 2016.

[314] Stefano Longhi. Quantum decay in a topological continuum. *Physical Review A*, 100(2):022123, 2019.

[315] Sabyasachi Barik, Aziz Karasahin, Christopher Flower, Tao Cai, Hirokazu Miyake, Wade DeGottardi, Mohammad Hafezi, and Edo Waks. A topological quantum optics interface. *Science*, 359(6376):666–668, 2018.

[316] M Ya Azbel, Per Bak, and PM Chaikin. Open orbits and generalized quantum Hall effect. *Physical Review Letters*, 59(8):926, 1987.

[317] N Dupuis and G Montambaux. Superconductivity of quasi-one-dimensional conductors in a high magnetic field. *Physical Review B*, 49(13):8993, 1994.

[318] Victor M Yakovenko. Quantum Hall effect in quasi-one-dimensional conductors. *Physical Review B*, 43(13):11353, 1991.

[319] Pan He, Chuang-Han Hsu, Shuyuan Shi, Kaiming Cai, Junyong Wang, Qisheng Wang, Goki Eda, Hsin Lin, Vitor M Pereira, and Hyunsoo Yang. Nonlinear magnetotransport shaped by Fermi surface topology and convexity. *Nature Communications*, 10(1):1–7, 2019.

[320] Vladimir P Bykov. Spontaneous emission from a medium with a band spectrum. *Soviet Journal of Quantum Electronics*, 4(7):861, 1975.

[321] Eleftherios N Economou. *Green's functions in quantum physics*, volume 7. Springer Science & Business Media, 2006.

[322] Tohru Morita. Useful procedure for computing the lattice Green's function-square, tetragonal, and bcc lattices. *Journal of Mathematical Physics*, 12(8):1744–1747, 1971.

[323] Valentin Zakharevich. Localization and stationary phase approximation on supermanifolds. *Journal of Mathematical Physics*, 58(8):083506, 2017.

[324] Jakob J Stamnes. Waves, rays, and the method of stationary phase. *Optics Express*, 10(16):740–751, 2002.

[325] Lei Ying, Ming Zhou, Michael Mattei, Boyuan Liu, Paul Campagnola, Randall H Goldsmith, and Zongfu Yu. Extended range of dipole-dipole interactions in periodically structured photonic media. *Physical Review Letters*, 123(17):173901, 2019.

[326] P Halevi, AA Krokhin, and J Arriaga. Photonic crystal optics and homogenization of 2D periodic composites. *Physical Review Letters*, 82(4):719, 1999.

[327] Patrick Ciarlet and Maryna Kachanovska. A mathematical study of a hyperbolic metamaterial in free space. *SIAM Journal on Mathematical Analysis*, 54(2): 2216–2250, 2022.

[328] Fabian HL Essler and Lorenzo Piroli. Integrability of one-dimensional Lindbladians from operator-space fragmentation. *Physical Review E*, 102(6):062210, 2020.

[329] Nicolai Lang and Hans Peter Büchler. Exploring quantum phases by driven dissipation. *Physical Review A*, 92(1):012128, 2015.

[330] Athreya Shankar, Jarrod T Reilly, Simon B Jäger, and Murray J Holland. Subradiant-to-subradiant phase transition in the bad cavity laser. *Physical Review Letters*, 127(7):073603, 2021.

[331] Marvin E Cage, Kv Klitzing, AM Chang, F Duncan, M Haldane, Robert B Laughlin, AMM Pruisken, and DJ Thouless. *The quantum Hall effect*. Springer Science & Business Media, 2012.

[332] M Berciu and AM Cook. Efficient computation of lattice Green's functions for models with nearest-neighbour hopping. *Europhysics Letters*, 92(4):40003, 2010.

[333] Leigh Page. Deflection of electrons by a magnetic field on the wave mechanics. *Physical Review*, 36(3):444, 1930.

[334] Miguel Bello, Gloria Platero, Juan Ignacio Cirac, and Alejandro González-Tudela. Unconventional quantum optics in topological waveguide QED. *Science Advances*, 5(7):eaaw0297, 2019.

[335] Janos Perczel and Mikhail D Lukin. Theory of dipole radiation near a Dirac photonic crystal. *Physical Review A*, 101(3):033822, 2020.

[336] Weiliang Ma, Guangwei Hu, Debo Hu, Runkun Chen, Tian Sun, Xinliang Zhang, Qing Dai, Ying Zeng, Andrea Alù, Cheng-Wei Qiu, et al. Ghost hyperbolic surface polaritons in bulk anisotropic crystals. *Nature*, 596(7872):362–366, 2021.

[337] Kanu Sinha, Alejandro González-Tudela, Yong Lu, and Pablo Solano. Collective radiation from distant emitters. *arXiv preprint arXiv:2006.12569*, 2020.

[338] Anthony Grbic and George V Eleftheriades. Periodic analysis of a 2-d negative refractive index transmission line structure. *IEEE Transactions on Antennas and Propagation*, 51(10):2604–2611, 2003.

[339] Sunil Mittal, Elizabeth A Goldschmidt, and Mohammad Hafezi. A topological source of quantum light. *Nature*, 561(7724):502–506, 2018.

[340] Janos Perczel, Johannes Borregaard, Darrick E Chang, Hannes Pichler, Susanne F Yelin, Peter Zoller, and Mikhail D Lukin. Topological quantum optics in two-dimensional atomic arrays. *Physical Review Letters*, 119(2):023603, 2017.

[341] D Rosenberg, D Kim, R Das, D Yost, S Gustavsson, D Hover, P Krantz, A Melville, L Racz, GO Samach, et al. 3D integrated superconducting qubits. *npj Quantum Information*, 3(1):1–5, 2017.

[342] Changsuk Noh and Dimitris G Angelakis. Quantum simulations and many-body physics with light. *Reports on Progress in Physics*, 80(1):016401, 2016.

[343] Sunil Mittal, Venkata Vikram Orre, Daniel Leykam, Yi Dong Chong, and Mohammad Hafezi. Photonic anomalous quantum Hall effect. *Physical Review Letters*, 123(4):043201, 2019.

[344] Wenlong Gao, Mark Lawrence, Biao Yang, Fu Liu, Fengzhou Fang, Benjamin Béri, Jensen Li, and Shuang Zhang. Topological photonic phase in chiral hyperbolic metamaterials. *Physical Review Letters*, 114(3):037402, 2015.